Microwave Dressed Potentials : a coherence control method for an atomic Sagnac Interferometer

Rhys Morrison

20279958

Supervisor : Dr Thomas Fernholz

A thesis presented for the degree of

Doctor of Philosophy

School of Physics and Astronomy

University of Nottingham

United Kingdom

01/09/2025

Abstract

The process of atomic interferometry relies heavily on the underlying atomic manipulation methods that have been developed over the past few decades. The ability to manipulate the internal state dynamics of atoms, and precisely control their time-space co-ordinates both lend themselves to the improvement of the sensitivities of these devices, allowing for more precise measurements, and more in-depth exploration of the physical world.

In this thesis the design of a state-dependent fully trapped interferometric transport is presented, wherein atoms are fully magnetically trapped for the entire duration of an interferometric sequence. Through use of Radio-Frequency dressed potentials, we are able to create a trapping system that is both robust, and able to create state-dependent trap that can be dynamically moved to create the mechanical basis for an interferometer.

We also investigate the coherence time of a superposition of hyperfine states loaded into the interferometer, necessary for a Ramsey-Borde sequence, and find it is significantly lower than what would be required to perform interferometry. We then present how this lack in coherence time is due to a mismatch in trapping potentials that arises due to a slight discrepancy between gyromagnetic ratios in the two superpositional states. This mismatch broadens the transition linewidth, leading to a reduction in superposition coherence time.

Finally, we lay out the theoretical groundwork, and experimental progress, in realising Microwave-Dressed potentials, which utilise the AC-Stark shift to adiabatically shift the trapping potentials of the atoms, reducing the mismatch and thus increasing the coherence time of the superposition.

Acknowledgements

I'd like to begin by thanking the fantastic support I have received from the Cold Atoms group here at the University of Nottingham, especially : My Supervisor Dr Thomas Fernholz, whose extensive knowledge, and ability to fix an experimental setup with a click of his fingers have been invaluable, and Vilus Atkocius, with whom I spent more time with than any other human being over the past four years, and whose conversations kept me sane during long experimental runs. I'd also like to thank Josh New, Nathan Cooper, Jamie Johnson, and the rest of the Cold atoms corridor crew, with whom lunchtime conversations remain some of my fondest memories. Finally, id like to thank my Family, for their ever continuing support, and most importantly, my brilliant, and loving partner, Parvathi Sajiv Kumar, who helped me through one of the most difficult times of my life.

Publication

This work is linked with, and supported by the following publication, of which I am an author:

Vilius Atkočius et al. "State-dependent transport in RF-dressed atom chip potentials". In: AVS Quantum Sci. 7 (April 30 2025) issn: 2639-0213.
DOI : https://doi.org/10.1116/5.0241484
url: https://pubs.aip.org/avs/aqs/article/7/2/023201/3345474/State-dependent-transport-in-RF-dressed-atom-chip

Contents

List of Figures

Chapter 1

Introduction

The purpose of this thesis is to provide an in-depth description of both experimental and theoretical efforts towards the creation of a fully trapped ^{87}Rb Sagnac interferometer. The Sagnac interferometer operates as a rotational sensor, not too dissimilar in principle to the famous atomic clock measurements performed by Hafele and Keating[44] in 1971, wherein precise measurements of atomic clock phase were used to confirm results predicted by the theory of special relativity. The ability to precisely measure one's own rotation is highly sought after, mainly due to its applications in navigation [31, 90, 94]. Not only can such measurements be used to figure out the bearing of a vessel with no other reference points (provided calibration was performed with respect to some known reference, a port for example), but the ability to measure ones rotational rate due to the Earth's axial spin means that precise measurements of latitude can be made, without the need for external satellite GPS systems, which could form the basis of entirely local GPS systems. Such applications require very precise measurements of rotational rates, which atomic interferometers theoretically excel at [43, 42], making them an ideal candidate for the future of the field. The only issue is that experimentally, atomic interferometers are far outperformed by conventional optical interferometers, with microwave interferometers being able to make nanometer-scale measurements on a commercial scale [87], an effect that is mostly derived from the flux difference between atomic interferometers, and light based interferometers. Combine this with the historically bulky and expensive setups used to op-

erate atomic interferometers, it is unsurprising that optical interferometers are commercially preferred.

Recent developments in the field [8], however, may look to change that, with advancements in the field of atomtronics [9, 75, 51, 4] allowing for smaller and less power consuming components, and advances in methods of measurement [80, 49], make the atomic interferometer a more attractive candidate than ever. The subject of this thesis, the fully trapped ^{87}Rb Sagnac interferometer seeks to take advantage of these advances. An innovative atom-chip design allows for precise control of atoms while minimising component size and power usage. A novel state-dependent transport method, which allows atoms to undertake an interferometric path, whilst remaining fully magnetically trapped is also used, which avoids wave-packet expansion due to free space propagation, and allows the interferometer to operate freely under tilt. Finally, novel coherence control methods allow for an increase in coherence time, allowing for longer interferometric sequences, opening the way for multiple loop sequences.

This introductory chapter will provide a groundwork in both concepts, and justifications, necessary to understand the drive to create such an interferometer. This will focus on the history of light, matter and measurements, concluding with the creation of the interferometer. Also included will be an overview of the objectives set out when I began work on this project, back in September 2020, as well as a brief description of the following chapters.

1.1 Light and Measurements

Scientific theory has long been reliant on the ability to make empirical measurements of the world around us, a precedent set by the French philosopher René Descartes [79]. In this pursuit of empiricism, we are limited by our ability to only measure three things : Position, Time, and Number of occasions. Its is then the ability to convert other physical properties of the world, from voltages to frequencies, into one of those three measurable quantities, that governs our ability to measure the world around us. In almost all experiments, we use the interactions between light and matter to make such conversions, from Newton's splitting of light via prisms to modern experiments, such as the measurement of quantum teleportation.

This section will take a dive into the history of measurements, as well as our understanding of light and matter, before arriving at the creation of the interferometer, all in an effort to understand the motivation for continuing the trend of making better and better measurements.

1.1.1 The Theory of Light

"*Where Lights is declared to be not Similar or Homogeneal, but consisting of difform rays, some of which are more refrangible than others: And Colors are affirm'd to be not qualifications of Light, deriv'd from Refractions of natural Bodies, (as 'tis generally believed;) but Original and Connate properties,which in divers rays are divers: Where several Observations and Experiments are alledged to prove the said Theory*". - Isaac Newton (February 19, 1672) [66]

This quote, and the letter that followed, would grant Isaac Newton the fame that he is still afforded today, and lay out his ray theory of light. Newtons main revelation, demonstrated by his well known experiment in which he split white light it its constituent colours through use of a triangular prism, was that colour was a inherent property of the light itself. Such a claim is in direct opposition to the prevailing theory of René Descartes(1637 [79]), in which the colour of light is a direct result of the '*plenum*' in which light propagates. Newtons theory that light was made up of rays of particles, that contained the information about said light, led theories around optics for the rest of the 17th and 18th centuries, despite work done by Robert Hooke[22], who likened light to mechanical water waves, and Christiaan Huygens who theorised that light was composed of vibrations perpendicular to the direction of travel [47]. This changed in 1802, when Thomas Young demonstrated that when light was shone through two close and narrow slits [48]; the light transmitted through each slit would interfere with the other and form a diffraction pattern on any far surface that it was imaged on. Such a result was not possible if light were composed of 'rays of particles' and instead meant that light must behave as a wave. The wave theory of Light was further strengthened by James Clark Maxwell who, in 1865, showed could be described as a direct consequence of the laws of electromagnetism, and through these laws described light as

a self-propagating electromagnetic wave, wherein the colour of light was tied to the frequency of electromagnetic oscillations, a theory that is still widely accepted to this day [57].

Whilst disproving Newton's theory of light was a step forwards, the new understanding of wave-light light brought forwards a new problem, if light was a wave, what would it travel through? Both other known waves, air and water, had clear media in which to propagate. Once again, René Decartes theory of light was relevant, and his '*plenum*' which when absorbed by the concepts proposed by both Huygens and Bernoulli, became known as the luminiferous aether. In an effort to measure the speed at which the aether travelled relative to earth, also known as the aether wind, two American physicists : Albert A. Michelson, and Edward W. Morley developed the first interferometer [62], in which the interference between two beams of light, propagating along two separate, orthogonal paths could be measured. The interferometer was placed on a liquid mercury table such that it could be rotated to measure the aether winds speed in multiple directions. It was found that there was no aether wind, a result that fundamentally changed our understanding of physics. Later renditions of the michelson-morley interferometer would result in LIGO, which led to the first detection of gravitational waves [1].

One other method that attempted to measure this luminiferous aether of particular importance was the Sagnac interferometer [76]. Created by French physicist Georges Sagnac the interferometer measures the phase difference between two waves propagating in opposite directions around a circular path. Measuring a phase difference between the two arms indicates that the device has been rotating in the rings plane, changing the dynamics of each arm with respect to one another (the exact nature of this change, whether it be a difference in path length or wave propagation speed, is dependent on which reference frame you work in). Much akin to the Michelson-Morley interferometer, the Sagnac Interferometer failed to measure the effects of any luminiferous aether, strongly suggesting its lack of existence.

1.1.2 Atomic Interferometers

In 1905, Albert Einstein wrote his Nobel prize winning paper on the photoelectric effect [29], the implications of which would define twentieth century physics. The quantisation of light gave birth to the field of quantum mechanics, and with it Louis de Broigle's description of matter waves [16]. The description of matter waves opened up the possibility of using these waves for interferometry, becoming an experimental possibility with the diffraction of electrons in 1927 by Davisson and Germer [24], and later an experimental certainty in 1930 when Estermann and Stern were able to produce diffraction patterns with sodium atoms [30]. By the 70s matter wave interference experiments [91] had reached the point in which they were able to be used in the measurements of physical quantities [55], including, but not limited to : Gravimetry(a feat not directly possible in optical interferometers, thanks to the massive nature of atoms) [85, 18, 21], Measurements of the earths rotation [67], and Magnetic field sensing [92]. These results were all produced via diffraction grating interferometers [73], but the field expanded, and new types of interferometer were able to be realised. The experimental realisation of Bragg pulse interferometry allowed for the realisation of two interferometric schemes in the atomic regime[13]. Mach-Zender interferometers [11, 58], a type of common path interferometry, and Ramsey-Borde interferometers, making use of Simultaneous Conjugate Atom Interferometry (SCI) to produce interferometric signals [59, 2], the results of which have been used to measure the fine structure constant down to a precision of 2 parts-per billion [20]. The massive nature of the atom, as mentioned before, opened up access to testing of the equivalence principle, as well, with recent results able to confirm the weak equivalence principle down to a level of 10^{-8} [96], a factor of 100 below previous measurements, precision measurements of the Newtonian gravitational constant [74], and the sensing of gravitational waves [26, 46, 40]. Other notable advances include the ability to generate Bose-Einstein condensates [5, 65], and the ability to produce larger interferometers via multi-photon kick operation [64, 19]. Atomic interferometers have recently expanded in regime to encompass interferometry on the ISS [93, 93, 53], testing microgravity, and into the regime of antimatter, where interferom-

etry has been preformed on positrons [77].

1.2 Justification

From seeing the potential power held within the atomic interferometer, and from seeing its flaws can we understand the desire for this projects Chip-based fully-trapped atomic Sagnac interferometer. The chip-based element solves many of the scale and weight issues that have plagued the atomic interferometers reputation, by placing all conductive components on a chip, and combined with recent advancements in on chip optics[70, 2, 75, 36], such as the ability to produce MOTs on a very small, and fast scale, chip-based atomic interferometers become a very attractive prospect. Combine this with the fully-trapped aspect, which removes many of the pitfalls of typically used Bragg based atomic interferometers, such as the expansion of atomic wave packets due to free space expansion, the ability to operate at a tilt without any change required to the setup, and the ability to perform many loops of the interferometer, increasing sensitivity. Future expansion to the project even include the ability to perform multiple interferometric sequences in succession[38],making progress towards bridging the flux gap between the atomic interferometer and optical interferometers.

The technology being developed here has the potential to be used in both commercial and research settings, over wide range of applications, from inertial sensing, to geolocation, and equivalence principle . It is hoped that the work performed during this project, and laid out in this thesis, can serve as the foundation for the creation of an interferometer that is the first of its kind, and as a reference for those wishing to foray into this field in the future.

1.3 Objectives

When I began my PhD, the project that this work is centered around had already been in production for nearly a decade, and was the labour of love of multiple other PhD students, the efforts of Fabio Gentile [37], Tom Bishop [12], and Jamie Johnson [50] are detailed in their respective theses. Despite

the groundwork made, the realization of the atomic Sagnac interferometer remained elusive, and the ability to load atoms into the ringtrap remained an un-achieved goal. With the overall stretch goal of the entire project being the completion and operation of the fully-trapped atomic Sagnac interferometer. This section will detail the objectives and tasks that made up the bulk of the work I performed on the project.

State Dependent transport

The first, and most crucial task to achieve was demonstrating the principle of Radio-Frequency (RF) Dressed potentials, and their ability to create state dependent traps that could be moved independently. The realisation of such a scheme requires a furthering of the ability to manipulate cold atom systems, such as long lifetime traps, efficient cooling techniques, and minimising atomic losses during loading and transport sequences. These requirements require tight control of magnetic fields, both static and dynamic, along with frequency control of AC fields, and noise reduction for all sources. Combined with the need for precise phase control in RF-frequency magnetic fields required for creating the interference effects that drive the state dependent transport. A more in depth look at the mechanics can be found in Vilius Atkocius' thesis [6].

Microwave Dressed Potentials

The second objective, and a crucial obstacle in the path of realising the interferometer was dealing with the limited coherence time of an atomic superposition in the state dependent traps. The problem arises due to a broadening of the natural linewidth of the clock transition due to slight changes in gyromagnetic ratio magnitudes between two trappable states. Such a problem is addressable through the use of microwave-frequency magnetic fields, that utilise the AC stark effect to adiabatically shift energy levels in a non-symmetric way, allowing us fine control over the linewidth of the clock transition.

1.3.1 Progress Milestones

The following table provides a brief summary of the objectives of this project, from initial setup of the experiment, to the realisation of the interferometer. It will be referenced later in the conclusion to measure the overall progress made on the project.

Progress Milestone	Completion
Loading atoms into a MOT	Complete
Transport to the Ringtrap	Complete
Demonstrate RF-Dressed Potentials	Partial
Load the RF-Dressed Ringtrap	Incomplete
RF-Dressed Transport Scheme	Incomplete
Multiple second trap Lifetimes	Incomplete
Demonstrate MW-Dressed potentials	Incomplete
200ms Coherence time/1Hz Linewidth	Incomplete
Full Ramsey Sequence	Incomplete
Rotational Interferometry	Incomplete
Signal maximisation and noise reduction	Incomplete

Table 1.1: Table of experimental milestone completion, as of September 2020

1.4 Description of this Work

This section will provide a brief overview of the following chapters of the thesis, for ease of use and reading. The descriptions are by no means in-depth or comprehensive, and only serve as a reference and guide to the chapters.

Chapter 2 : Theoretical Background

Chapter 2 outlines the necessary theory to understand the work performed throughout this project. It discusses the mechanics behind sagnac, and matter wave interferometry, The hyperfine structure of the atom, and how the associated magnetic dipoles of those levels interact with magnetic fields, both static and time-dependent. We also introduce the groundwork for the Floquet approach to dressed atomic states. Finally, we discuss Ramsey-Borde interferometry sequences, and their relations to the atomic states of

the atom, completing an overview of how an atomic interferometer would function.

Chapter 3 : Cold Atom Manipulation

Chapter 3 describes the techniques and processes that are instrumental in the manipulation of cold atom systems. The chapter is split into two halves, the first of which describes, in detail the different techniques that range in commonality form industry standard, like the Magneto-Optical Trap, to more niche methods, such as optically plugged quadrupole traps. The second section then details the experimental procedure used in the project itself, in getting atoms from a Rubidium dispenser at room temperature, to sub milli-kelvin, and loaded into a Radio-Frequency dressed ringtrap.

Chapter 4 : Experimental Setup

Chapter 4 provides an exploration into the physical setup present in the lab, from vacuum chambers and large MOT coils, to the precise generation of high-frequency currents, which require tight phase control, and very low noise. The chapter then goes on to describe the optical setup, in which laser light is used to provide a range of optical fields, and the methods by which the frequency, power and polarisation of such fields are controlled. Finally, a look at the state-of-the-art atom chip that is central to the setup is provided.

Chapter 5 : RF-Dressed Microwave transitions

Chapter 5 begins to explore the principles that are central to the creation of the Matter-Wave interferometer, namely the creation of quantum superpositions of atomic states, and the realisation of state-dependent transport sequences. The chapter will explore how the existence of an RF-Dressing field allows for a greater selection of allowed transitions, and how such a scheme can be utilised, and characterised. It then builds upon the foundation laid in earlier chapters to detail how the RF-Dressed ringtrap can be used to provide state-dependent transport, and outlines the steps required to achieve such a process.

Chapter 6 : Microwave-Dressed Potentials

Chapter 6 investigates further the issue of decoherence with the prepared quantum superposition, linking its existence to fundamental properties of the atomic states. It then provides a potential solution to the issue, Microwave Dressing of the potentials, providing a theoretical model, and experimental results. Some discrepancies between the results will then attempt to be explained via a different theoretical model that utilises floquet theory to explain the microwave-dressed potentials.

Chapter 7 : Conclusion

Chapter 7, the conclusion, ties all of the previous chapters together, showing what aims and objectives had been achieved, and what still needs to be realised. It also takes a look into some potential future possibilities for the project.

Chapter 2

Theoretical Background

This chapter exists to provide a detailed overview of the theoretical background required to both justify and understand this thesis. With the ultimate aim of the project being to create a fully trapped atomic interferometer, a background understanding of the operations of both interferometers and atomic manipulation is required. The first section of this chapter will give an understanding as to how atomic interferometers function, whilst justifying the decision to create a fully trapped interferometer. The second section of this chapter will provide a detailed overview of the internal mechanics of the Rubidium-87 (^{87}Rb) atom. This will lay the foundations is explaining the vast multitude of techniques referenced in this thesis.

2.1 The Atomic Sagnac

This section will provide an overview into the mechanisms required to understand and create an atomic interferometer. From understanding how phase accumulation works for matter waves, to describing the operation of an atomic interferometer, a comprehensive overview will be given. More information on this topic can be found in [3].

2.1.1 Matter Wave Interferometry

The principle of matter-wave interferometry relies on the quantum mechanical wave-like nature of matter. Quantum mechanics tells us that all particles have a Compton wavelength,

$$\lambda_c = \frac{h}{mc}, \tag{2.1}$$

which is a measure of equivalent photon wavelength for a particle with rest mass m. Such waves have the ability to interfere in the same way that classical electromagnetic waves can. This can be used to make measurements through interferometric sequences, wherein the difference between two arms of an interferometer can be measured via a difference in phase induced between two waves. We can calculate the Compton wavelength of a ^{87}Rb atom to be 1.51×10^{-17}m, significantly shorter than even Gamma ray light. Such a wave picks up additional phase according to its own motion and changes in potential energy, the shift in phase, $\Delta\phi$ can be calculated by considering the classical path action of the particle, obtained by integrating over the particles Lagrangian with respect to a specific time frame [83]:

$$\Delta\phi = \int_{t=0}^{t=\tau} \mathcal{L} \ \ dt \tag{2.2}$$

Where,

$$\mathcal{L} = T - V = \frac{1}{2}mv^2 - V(x) \tag{2.3}$$

for a 1-dimensional path. From this we can see immediately why atomic interferometry is such a powerful tool, not only can it be used to measure very small changes in distance, but also as a measure of local potential changes. This allows atomic interferometers specifically to use the mass of the atom to probe into area that standard light interferometers struggle to do, or simply cannot, such as : Gravitational wave detection, Equivalence principle testing, and Charge-Parity violation testing. A example interferometric sequence can be seen in Figure 2.1, where a superposition of two states, $|red\rangle$ and $|blue\rangle$, is created, separated, and then recombined, to obtain an interference signal, gaining information about the two separate paths.

It might seem, from Equation 2.3, that such an interferometric sequence could be utilised to gain absolute information about the velocity of a given reference frame, as in the absence of any potential landscape, the phase gain is only dependent on velocity (and mass, which we assume to be in-

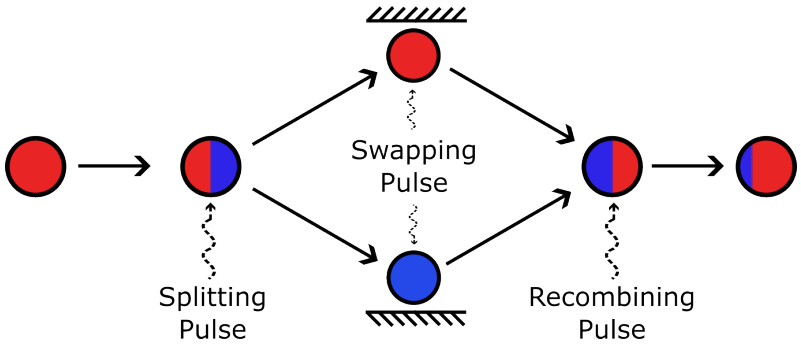

Figure 2.1: An interferometry sequence with two states $|red\rangle$ and $|blue\rangle$, light acts as a beam splitter, and as mirrors, for the purpose of matter-based interferometry.

variable), which is a violation of the Galilean principle. To measure this absolute velocity, however, one would have to measure the absolute phase of a given particle, which is neither possible experimentally, or a meaningful idea theoretically. Instead, interferometry makes differential measurements, meaning that only the difference in phase between two interfering particles is able to be measures, and as a result, only the difference in contributions to phase from velocity are able to be measured. The measurement of interference must also be local, meaning that the particles must be in the same location to make the measurement, resulting in a situation where the differential measurement requires one, or both of the particles, to enter into accelerating (non-inertial) reference frames, losing information on their absolute velocities, and maintaining the Galilean principle.

2.1.2 Sagnac Interferometry

Whilst the Lagrangian method gives rise to a broad explanation of matter-wave interferometry in general, the specific case of Sagnac interferometry can be better explained through observing the relativistic effects that occur within a rotating interferometer. We begin by considering the Sagnac interferometer to be a circular ring-like device, with radius R. In the lab frame, the ring rotates at an angular rate of Ω, we define rotational directions in this lab frame in a $+, -$ basis, referring to counter clockwise, and clockwise rotations respectively. To transform from the static lab frame into the rotating ring frame we must consider the relativistic Lorentzian

transformations for time:

$$t' = \gamma \left(t - \frac{\Omega R x}{c^2} \right) \tag{2.4}$$

and position:

$$x' = \gamma \left(x - \Omega R t \right) \tag{2.5}$$

Here we introduce the lorentz factor:

$$\gamma = \frac{1}{\sqrt{1 - \frac{v^2}{c^2}}} \tag{2.6}$$

Where v is the phase velocity of a wave travelling around the interferometer. The phase velocities of waves, $v_{\pm}$, travelling in two counter propagating directions around the rotating ring are given as:

$$v'_{\pm} = \frac{x'_{\pm}}{t'} = \frac{v \pm R\Omega}{1 \pm \frac{vR\Omega}{c^2}} \tag{2.7}$$

The path lengths of the two waves travelling in the rotating ring frame is:

$$l'_{\pm} = 2\pi R \pm T\Omega t'_{\pm} \tag{2.8}$$

Where T is the average time taken for a wave to propagate around the interferometer. This difference in path length, and phase velocity between the two arms of the Sagnac interferometer, manifests in a different effective evolution time $t'_{\pm} = \frac{l'_{\pm}}{v'_{\pm}}$. To calculate the phase difference between the two rings we consider the difference in this evolution time:

$$\Delta t = |t'_{+} - t'_{-}| = \frac{4\pi R^2 \Omega}{c^2 \left(1 - \frac{R^2\Omega^2}{c^2}\right)} \tag{2.9}$$

This is the Sagnac effect for a circular interferometer. To generalise it, we can substitute in the area $A = \pi R^2$, and see that the time evolution difference induced is directly proportional to the space-time area enclosed by the interferometer path, and to the rotation rate of the interferometer. The geometric setup of the Sagnac interferometer can be seen in Figure 2.2.

Atomic-Sagnac Effect

The effect can be further specified for the matter-wave case for atoms by considering the time difference as a function of Compton wave evolution. The Compton frequency ν_C of an atom of mass m is given by:

$$\nu_C = \frac{mc^2}{h} \tag{2.10}$$

The resulting induced Sagnac phase then becomes:

$$\Phi = 2\pi\nu_C\Delta t = \frac{mc^2}{\hbar}\frac{4A\Omega}{c^2\left(1-\frac{R^2\Omega^2}{c^2}\right)} \tag{2.11}$$

Whilst the ring is rotating at non-relativistic velocities (i.e. $R\Omega \ll c$). The atomic Sagnac phase approximates to:

$$\Phi = \frac{4mA\Omega}{\hbar} \tag{2.12}$$

2.1.3 Ramsey-Borde Interferometry

In order to measure the difference in phase accumulated by two atomic species travelling around a ring, we require a method that converts a phase difference into a measurable quantity. For this purpose, we employ the Ramsey sequence [72], a method that turns phase differences between two atomic states into a state population difference, which is a measurable quantity. To understand this process, suppose that we have a cloud of atoms, all in a ground state $|-\rangle$, that can be driven via single-photon transitions to an excited state $|+\rangle$. A Ramsey sequence involves first creating an equal super position of the two states by driving the cloud for a quarter of a rabi cycle. This pulse can be represented as a rotation on the Bloch sphere about the x-axis by an angle of $\frac{\pi}{2}$ radians, the Bloch sphere representations and the sequence are shown in Figure 2.3.The two states are then physically separated, so that they can independently evolve their respective phases. Halfway through this process, a second pulse, which corresponds to a π rotation about the x axis on the Bloch sphere, inverts the states. This serves the purpose of eliminating any state-dependent phase gains(i.e.

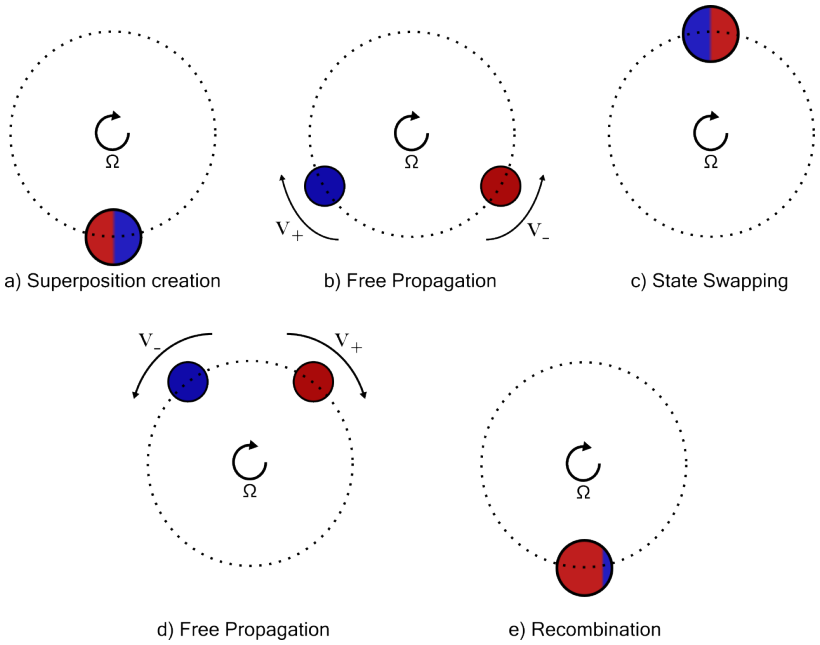

Figure 2.2: Simple Diagram showing the principle of atomic Sagnac interferometry. A superposition between the states $|red\rangle$ and $|blue\rangle$ is created in a, allowed to freely propagate around a circular path, with a lab frame rotation of Ω(where the atoms co-rotating with Ω have a velocity of v_+, and counter rotation has a velocity of v_-). The superposition is inverted in c, allowed to freely propagate back to the origin, before recombination maps the phase difference onto a population imbalance between the two states.

the $|+\rangle$ interacts more strongly with stray magnetic fields, causing it to evolve phase faster). Once the interferometric sequence is done, the two states are recombined with another $\frac{\pi}{2}$ pulse (finishing the sequence, as the sum of all pulses adds to 2π). If there was no phase difference between the two clouds of atoms, then the final recombination pulse transfers all atoms back into the initial $|-\rangle$ state. However, if there were a difference in phase accumulation, not all atoms are transferred back into the $|-\rangle$ state, a population imbalance that can be directly measured through spectroscopic techniques. The representation of this sequence as expressed on the Bloch sphere can be seen in Figure 2.3.

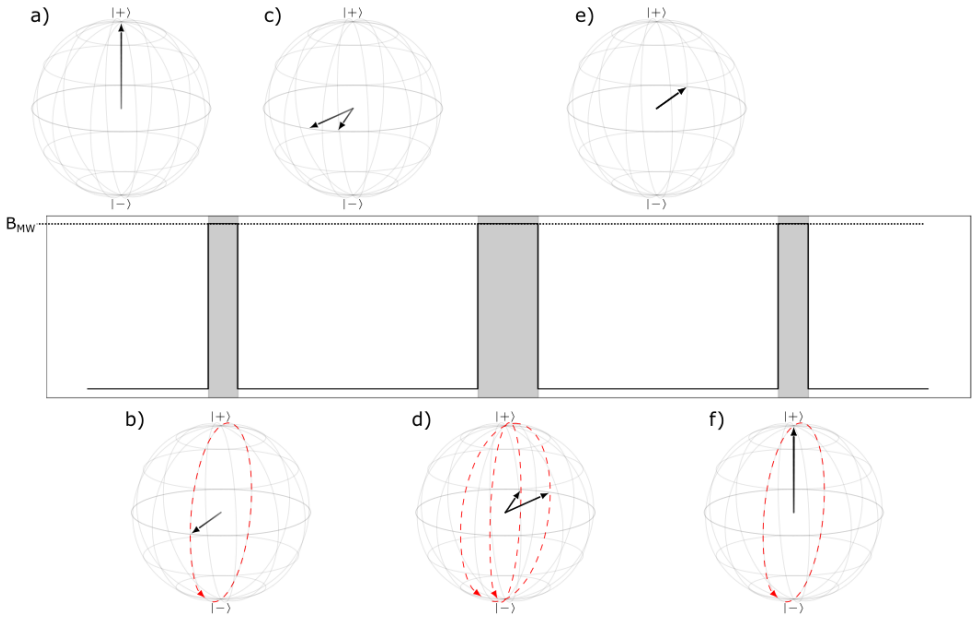

Figure 2.3: A Ramsey sequence. The centre graph shows the required field pulses (Highlighted in grey). The Bloch spheres show the expected state of the atoms over the sequence. a) Atoms are in a pure quantum state of $|+\rangle$. b) A $\frac{\pi}{2}$ pulse drives the atoms into a superposition of $|+\rangle$ and $|-\rangle$. c) Free evolution occurs between the two superpositional states. d) The superposition is inverted with a π pulse. e) Another free evolution stage where the two states evolve if there is no path difference they remap onto each other. f) A final $\frac{\pi}{2}$ pulse drives the superposition back towards the $|+\rangle$ pure state.

Driving the atomic clouds between the $|-\rangle$ and $|+\rangle$ states requires an energy coupling between the two levels. For the purposes of this project

we will consider single-photon transitions between energy levels, meaning that they can be directly coupled with optical or magnetic fields. The next section will describe the details of these energy levels, and how ^{87}Rb can be coupled to magnetic fields to be driven between its different internal states.

2.2 The Rubidium Atom : A detailed view

When choosing an atomic species for cold atoms experiments, it is common to settle on alkali metals, as their hydrogen-like electronic structure (only having one outer shell electron) makes them easy to theoretically and manipulate. Whilst there are several alkali metals to choose from, the experiment uses Rubidium-87 (^{87}Rb), a heavier isotope of atomic Rubidium, it is found in an abundance of about 20% along with the other isotope - Rubidium-85. This is a common choice amongst cold atoms experiments, mostly due to ^{87}Rb 780nm transition line, which falls within the infrared range, at a frequency commonly used for laser-disk applications. As a result, laser technology for interacting with that ^{87}Rb transition is comparatively cheap and stable, owing to years of commercial progress. The section will describe the inner workings of the ^{87}Rb atom, starting with its electronic and nuclear structure, and how the interactions between them give rise to the internal energy levels. After this, methods of coupling to and between these energy levels are discussed; this includes both static DC magnetic field coupling, and AC coupling between internal energy states. The information in this section commonplace amongst textbooks such as [32, 34]. Further reading about associated effects can be found in [60].

2.2.1 Atomic Structure of ^{87}Rb

The section aims to provide an overview for the internal mechanics of the ^{87}Rb atoms. The internal energy states of which arise from the inter-coupling of angular momenta within the atom itself.

Electron Shells

The defining feature of ^{87}Rb is its position amongst the alkali metals on the periodic table, meaning that it only has 1 electron in its outermost shell.

As all other electron shells are full, and thus have zero impact on the net angular momentum of the atom, they can be largely ignored. This leaves ^{87}Rb appearing as an atom with a single electron in its n = 5 shell. The angular momentum of the electron in the outermost shell is

$$L = \sqrt{l(l+1)}\hbar \qquad (l = 0, 1, ..., n-1) \tag{2.13}$$

The values for angular momentum L are integer multiples of $\hbar$, however it is helpful for readability to just refer to them as the $L = 0, L = 1...$ states, naturalising them to their quantum number l values. The energy of the atomic state can be computed using the Bohr formula for a charged particle in an inverse squared potential:

$$E_B = -hc\frac{R_c}{\mathbf{n}^*} \tag{2.14}$$

Where R_c is the Rydberg constant, and $\mathbf{n}^*$ is the principle quantum number (electron shell number) modified slightly to take into account the slight effect of the nucleus charge on the outer electron, due to imperfect charge screening. The value of $\mathbf{n}^* = n^2 - \delta_L$ depends on the angular momentum of the electron, which alters the quantum defect δ_L. The states $L = 0$, and $L = 1$ are nominally referred to as the $\mathcal{S}$ and $\mathcal{P}$ orbitals, respectively. These are the only two orbital states to which this thesis will refer. For ^{87}Rb the quantum defects for these two orbitals are $\delta_{\mathcal{S}} = 3.19$ and $\delta_{\mathcal{P}} = 2.64$. For data on ^{87}Rb see [82].

Spin-Orbit Coupling

As with all electrons, the electron in the outer shell of ^{87}Rb has an intrinsic spin of $\frac{1}{2}$, this spin vector $\hat{\mathbf{S}}$ couples to the orbital angular momentum vector $\hat{\mathbf{L}}$. The interaction Hamiltonian is:

$$\hat{H}_{fs} \propto \hat{\mathbf{L}} \cdot \hat{\mathbf{S}} = \frac{1}{2}(\hat{\mathbf{J}^2} - \hat{\mathbf{L}^2} - \hat{\mathbf{S}^2}) \tag{2.15}$$

We introduce $\hat{\mathbf{J}} = \hat{\mathbf{L}} + \hat{\mathbf{S}}$ as the total angular momentum vector for the electron. From 2.13 it can be inferred that the total energy of this interaction is:

$$E = j(j+1) - l(l+1) - s(s+1) \tag{2.16}$$

It can be seen for the $\mathcal{S}$ orbital, which has angular momentum $l = 0$, that the spin orbit interaction is non-existent, as there is no orbital angular momentum for the electrons spin to couple to. However, for the $\mathcal{P}$ orbital, the total angular momentum takes two possible values, as the orbital angular momentum $\hat{\mathbf{L}}$ and spin $\hat{\mathbf{S}}$ can either align or anti align, leading to a situation where $j_{\pm} = |l-s|, l+s$.This causes a splitting of the initial energy level into two sub energy levels, referred to as the fine states. The singular $\mathcal{S}$ orbital fine state is called the $5^2\mathcal{S}_{\frac{1}{2}}$ state, whereas the two $\mathcal{P}$ orbital fine states are the $5^2\mathcal{P}_{\frac{1}{2}}$ and the $5^2\mathcal{P}_{\frac{3}{2}}$ for the anti-aligned and aligned coupling, respectively.

Nuclear Angular Momentum

The third and final angular momentum to consider in intra-atomic coupling is that of the atomic nucleus. The nuclear angular momentum $\hat{\mathbf{I}}$ couples to the net electron angular momentum $\hat{\mathbf{J}}$ with the interaction Hamiltonian

$$\hat{H}_{hfs} \approx \mathbf{A}_{HFS}(\hat{\mathbf{I}} \cdot \hat{\mathbf{J}}) = \frac{1}{2}(\hat{\mathbf{F}^2} - \hat{\mathbf{I}^2} - \hat{\mathbf{J}^2}) \tag{2.17}$$

Where we have once again introduced a new angular momentum vector $\hat{\mathbf{F}} = \hat{\mathbf{I}} + \hat{\mathbf{J}}$, which is the net sum of all angular momenta withing the atom, we also introduce the magnetic dipole constant $\mathbf{A}_{hfs}$. It should be noted that this approximation ignores the effect of higher order terms that arise due to the electric quadrupole interaction, and the magnetic octupole interaction, which depend on $(\hat{\mathbf{I}} \cdot \hat{\mathbf{J}})^2$ and $(\hat{\mathbf{I}} \cdot \hat{\mathbf{J}})^3$ respectively. The higher order terms mean that this approximation is only valid for fine states in which $l = \frac{1}{2}$ (i.e. only the $5^2\mathcal{S}_{\frac{1}{2}}$ and the $5^2\mathcal{P}_{\frac{1}{2}}$ states will be considered). The energy associated with this Hamiltonian is:

$$E \approx \mathbf{A}_{HFS}(f(f+1) - i(i+1) - j(j+1)) \tag{2.18}$$

This energy shift causes each fine state with $l = \frac{1}{2}$ to split into two new hyperfine sub-levels, with a frequency splitting of $2 * \frac{A_{hfs}}{h} = 6.8347$ GHz for the $5^2\mathcal{S}_{\frac{1}{2}}$ level. An illustration of the full Hyperfine splitting for the ^{87}Rb

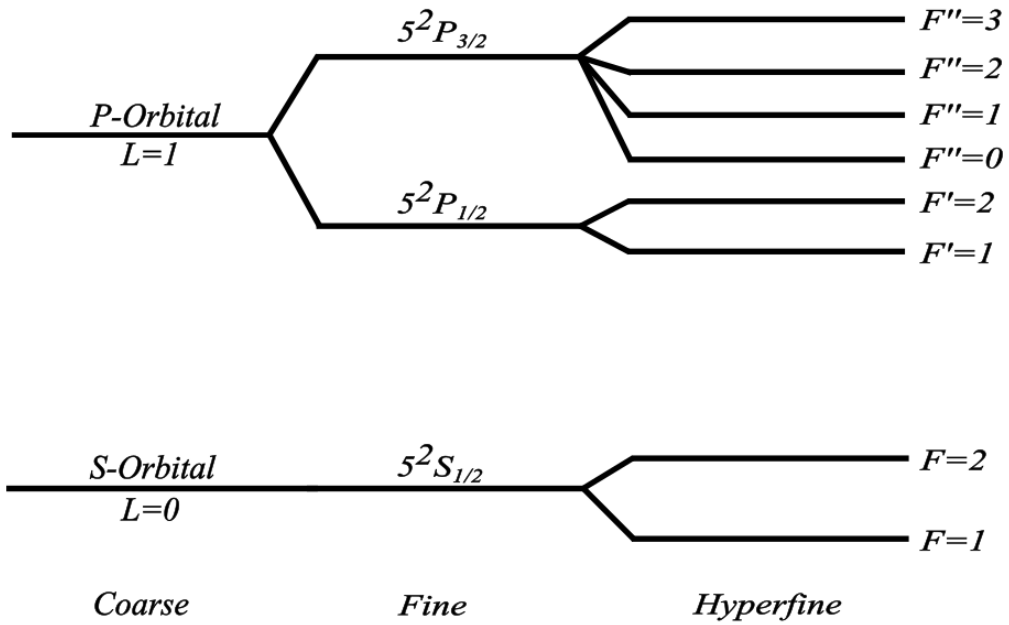

Figure 2.4: Diagram showing the coarse, fine, and hyperfine energy levels for the $L = 0$ and $L = 1$ orbitals of ^{87}Rb. This Diagram is adapted from [82] where a more detailed diagram is availible.

atom can be seen in Figure 2.4.

2.2.2 Coupling to Static Magnetic Fields

The energy levels of ^{87}Rb shown above are of little use if the atom cannot be manipulated via external means. This subsection will detail how ^{87}Rb couples to external magnetic fields, both in the DC (static field) and AC (time-dependent field) regimes. The angular momenta from last chapter form a magnetic dipole of the atom, which couples to external magnetic fields with the interaction Hamiltonian :

$$\hat{H}_B = -\hat{\boldsymbol{\mu}}_T \cdot \hat{\mathbf{B}} = -(\hat{\boldsymbol{\mu}}_{\hat{\mathbf{I}}} + \hat{\boldsymbol{\mu}}_{\hat{\mathbf{S}}} + \hat{\boldsymbol{\mu}}_{\hat{\mathbf{L}}}) \cdot \hat{\mathbf{B}} \tag{2.19}$$

We can define an arbitrary magnetic dipole moment $\hat{\boldsymbol{\mu}}_{\hat{\mathbf{N}}}$, that is created by an angular momentum operator $\hat{\mathbf{N}}$ as:

$$\hat{\boldsymbol{\mu}}_{\hat{\mathbf{N}}} = \mu_B g_N \hat{\mathbf{N}} \tag{2.20}$$

Where μ_B is the Bohr magneton, and g_N is the gyromagnetic ratio, or landé g-factor, of the associated magnetic dipole. For a weak magnetic field, we can consider the total magnetic dipole $\hat{\boldsymbol{\mu}}_T$ as the total sum of all angular momenta, in other words, all angular momenta components within the atom couple collectively to the magnetic field, such that $\hat{\boldsymbol{\mu}}_T = \hat{\boldsymbol{\mu}}_F$. As such, the interaction Hamiltonian becomes:

$$\hat{H}_B = -\hat{\boldsymbol{\mu}}_F \cdot \hat{\mathbf{B}} = -\mu_B g_F \hat{\mathbf{F}} \cdot \hat{\mathbf{B}} \tag{2.21}$$

The field couples to the projection of the angular momentum along the quantisation axis defined by the field direction, for ease of use we define this as the z-axis. As the total angular momentum $\hat{\mathbf{F}}$ takes quantised values according to 2.13, the projection of this spin must also take quantised values:

$$m_f = -f, -f+1, ..., 0, ..., f-1, f \tag{2.22}$$

Where f is the quantum number associated with angular momentum $\hat{\mathbf{F}}$. These quantised projections, m_f, simplify the Hamiltonian down such that we can simply extract the energy shift due to an atomic dipole coupling to a magnetic field as:

$$\Delta E_B = \mu_B \langle F, m_F | \, g_F \hat{\mathbf{F}} \cdot \hat{\mathbf{B}} \, | F, m_F \rangle = -\mu_B g_F m_f |\mathbf{B}| \tag{2.23}$$

The existence of these magnetic sub-levels gives rise to an energy dependence that depends on which state the atomic dipole is in. Different magnetic substates can leave the energy shift positive or negative, depending on the alignment (sign) of the magnetic sub-level m_f, and the sign of the gyromagnetic ratio of the corresponding hyperfine manifold. This is the origin of Zeeman splitting [95], where any given hyperfine level with angular momentum $F = n$ splits into $2n + 1$ sub-levels, according to 2.22. A graphical representation of the Zeeman splitting of the $F = 1$ and $F = 2$

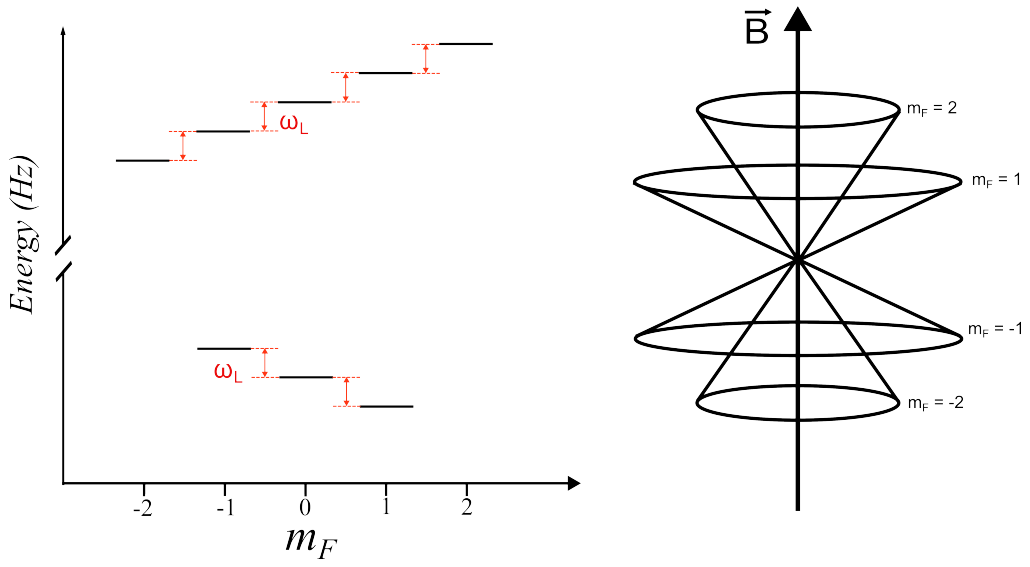

Figure 2.5: Left : Zeeman splitting of the $F = 1$ (lower) and $F = 2$ (upper) hyperfine manifolds, in the presence of a weak magnetic field. Right : Spin cone projection of the m_F levels of the $F = 2$ manifold.

states is given in Figure 2.5.

This thesis is mostly interested in the $5^2\mathcal{S}_{\frac{1}{2}}$ state, which has 2 hyperfine levels, $F = 1$ and $F = 2$. These hyperfine levels have 3 and 5 magnetic sub-levels, respectively. These sub-levels will be denoted in a $|F, m_f\rangle$ basis, for ease of reading. The gyromagnetic ratios of the two hyperfine manifolds in the $5^2\mathcal{S}_{\frac{1}{2}}$ state are $g_{F1} = -0.50182671$ and $g_{F2} = 0.49983642$ (often simplified to -0.5 and 0.5 respectively) as calculated by:

$$g_F = g_J \frac{f(f+1) + j(j+1) - i(i+1)}{2f(f+1)} + g_I \frac{f(f+1) - j(j+1) + i(i+1)}{2f(f+1)} \tag{2.24}$$

We may also define the larmor precession frequency:

$$\omega_l = \frac{\Delta E_B}{\hbar} \tag{2.25}$$

Which, in a semi-classical approach to the coupling, defines the rate at which the magnetic dipole precesses about the magnetic fields quantisation axis.

The linear scaling of the Zeeman splitting with magnetic field magnitude does propose one small problem on its own, which is that there is some

magnetic field value at which the $|1,1\rangle$ state becomes degenerate with the $|2,-2\rangle$ state. At these larger field values, it is no longer appropriate to consider the magnetic field as coupling with the $\hat{F}$ manifold, and instead we see that the large magnetic field disrupts the coupling between the nucleus and outer-shell electron. Because of this we must consider the static field coupling to the $\hat{J}$ manifold instead, and its associated m_J states:

$$\hat{H} = -\mu_B g_J \hat{\mathbf{J}} \cdot \hat{\mathbf{B}} \tag{2.26}$$

This is the Paschen-Beck effect, which denotes the interruption of nuclear-electron coupling, in favour of individual couplings to the static magnetic field. In a similar fashion to solving the weak field problem, we obtain similar results obtaining an energy shift of:

$$\Delta E_B = \mu_B \langle J, m_J | \, g_F \hat{\mathbf{J}} \cdot \hat{\mathbf{B}} \, | J, m_J \rangle = -\mu_B g_J m_J |\mathbf{B}| \tag{2.27}$$

Where the associated gyromagnetic ratio for the fine state $5^2\mathcal{S}_{\frac{1}{2}}$ is 2.00233113. As one would expect, there is an intermediate region in which the m_F states transform into the m_J states. We calculate the energy levels of this state transformation with the Breit-Rabi formula [14]:

$$\Delta E = -\frac{hA_{HFS}}{2(2i+1)} + \mu_B g_I m_F \mathbf{B} \pm \frac{hA_{hfs}}{2}\sqrt{1 + \frac{2m_F x}{i+\frac{1}{2}} + x^2} \tag{2.28}$$

Where x is the field strength parameter, that describes the transitory fields between the weak and strong field regime:

$$x = \frac{B(\mu_B g_J - \mu_B g_I)}{hA_{hfs}} \tag{2.29}$$

Interestingly, despite $\hat{F}$ no longer being a well defined manifold, its spin projection m_F remains a good quantum number and can be used to calculate the resulting magnetic field couplings. This more complete view of the Zeeman sub-levels is shown in Figure 2.6

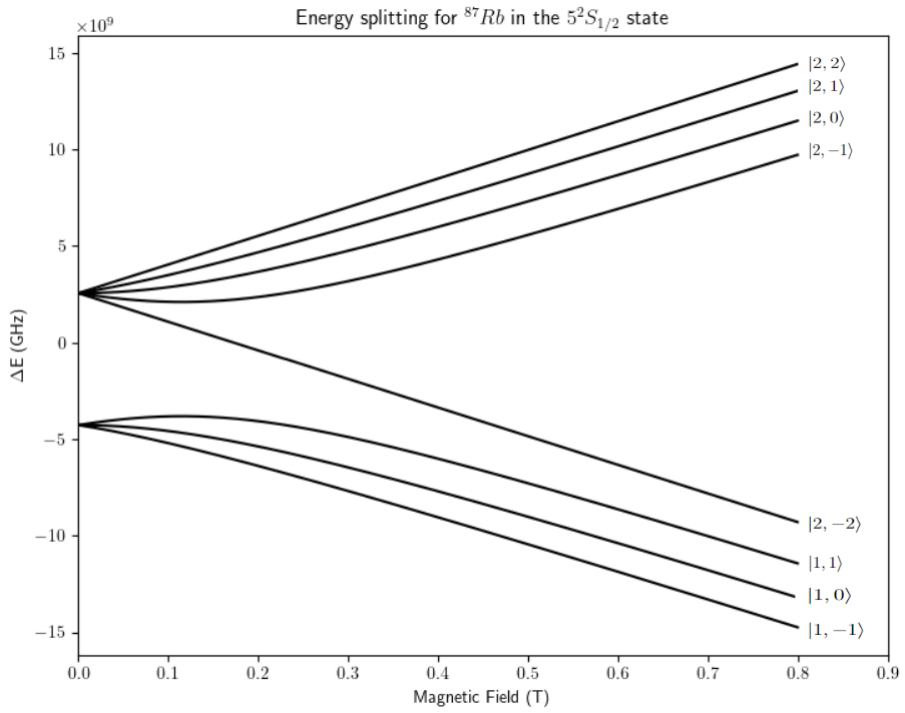

Figure 2.6: Energy splitting of the $5^2\mathcal{S}_{\frac{1}{2}}$ state of the ^{87}Rb atom that occurs in the weak field and strong field regimes due to a static magnetic field.

Going even further, one would expect there to be further degeneracy in the m_J, as the static field increases further still, such that the Zeeman splitting becomes greater than the fine splitting. In this scenario all components of internal angular momentum of the atom couple to the magnetic field separately, making the energy splitting very difficult to calculate. Thankfully, the Paschen beck effect is considerably beyond consideration for this experiment.

2.2.3 Coupling to Time-Dependent Fields

The coupling of atoms to static magnetic fields gives rise to the semi-classical concept of the larmor precession, a time-dependent property of a magnetic dipole. In this section we will examine how the resonant driving of this larmor precession via time-dependent magnetic fields operates. Such theory is set up mostly in academic papers, such as [45].

To begin, we consider a magnetic field B_{Tot} that has a static component

B_{DC}, and a time-dependent component B_{AC}

$$B_{Tot} = B_{DC} + B_{AC}(\omega t) \tag{2.30}$$

Substituting this in to equation 2.21 gives us:

$$\hat{H}_{TOT} = \hat{H}_{DC} + \hat{H}_{AC} \tag{2.31}$$

To solve the effects of an AC magnetic field on the atomic dipole, it is helpful to move to a different co-ordinate system. We move to the circular co-ordinate system, defined as:

$$\begin{aligned} \hat{\sigma}_+ &= \frac{1}{\sqrt{2}}(\hat{x} + i\hat{y}) \\ \hat{\sigma}_- &= \frac{1}{\sqrt{2}}(\hat{x} - i\hat{y}) \\ \hat{\pi} &= \hat{z} \end{aligned} \tag{2.32}$$

We can write the AC magnetic field in the co-ordinate system as:

$$B_{AC} = (B_{\sigma+}\hat{\sigma}_+ + B_{\sigma-}\hat{\sigma}_- + B_\pi\hat{\pi})\exp(-i\omega_{AC}t) + \mathbf{c.c.} \tag{2.33}$$

Here we choose the z-direction to be the direction of the static magnetic field. We can substitute equation 2.33 into equation 2.31, to see that the energy shift induced by the AC field will be the eigenvalues of the Hamiltonian:

$$\hat{H}_{TOT} = \frac{\mu_B g_F}{2}\left(\hat{F}_z B_{DC} + \left(\frac{1}{\sqrt{2}}(\hat{F}_+ B_{\sigma+} + \hat{F}_- B_{\sigma-}) + \hat{F}_\pi B_\pi\right)\exp(-i\omega_{AC}t)\right) + \mathbf{h.c.} \tag{2.34}$$

Where we have introduced the ladder operators F_+ and F_-, that are defined

as:

$$\begin{aligned}\hat{F}_+ &= \frac{1}{\sqrt{2}}(\hat{F}_x + i\hat{F}_y)\\ \hat{F}_- &= \frac{1}{\sqrt{2}}(\hat{F}_+ - i\hat{F}_-)\\ \hat{F}_\pi &= \hat{F}_z\end{aligned} \tag{2.35}$$

The eigenenergies of the total Hamiltonian can be numerically obtained directly for a field of arbitrary polarisation. It is easier, however to consider the coupling of a circularly polarised field in the xy plane (σ_+ or σ_-), which will be that norm for the rest of this thesis. The direction can be defined by the sign of ω_{AC}, as $\sigma_+(\omega t) = \sigma_-(-\omega t)$. We introduce a rotation operator to transform us into a frame of reference co-rotating with this circularly polarised field.

$$\hat{U}_\pm = \exp\Big(i(\varphi \pm \omega_{AC}t)\hat{F}_z\Big) \tag{2.36}$$

where the direction of rotation is defined by the sign of ωt. The operator $\hat{U}_\pm$ transforms the wavefunction ψ into its rotated form ϕ, such that $\phi = \hat{U}_\pm\psi$. Starting from the time-dependent schrödinger equation ($\hat{H}\psi = i\hbar\frac{\partial\psi}{\partial t}$) we can obtain the time-evolved form of the wavefunction:

$$i\hbar\frac{\partial\psi}{\partial t} = i\hbar\frac{\partial\hat{U}_\pm}{\partial t}\psi + \hat{U}_\pm\hat{H}\psi = i\hbar\frac{\partial\hat{U}_\pm}{\partial t}\hat{U}_\pm^\dagger\phi + \hat{U}_\pm\hat{H}\hat{U}_\pm^\dagger\phi \tag{2.37}$$

We can use the commutation relation $\left[\hat{F}_z, \hat{U}_\pm\right] = 0$ to simplify $i\hbar\frac{\partial\hat{U}_\pm}{\partial t}\hat{U}_\pm^\dagger\phi = -\hbar\omega_{AC}\hat{F}_z$ and a substitution into equation 2.34 to obtain the full hamiltonian in the rotating frame:

$$\begin{aligned}\hat{H}_{rot} = \frac{\mu_B g_F}{2}\Bigg(&\left(B_{DC} - \frac{\hbar\omega_{AC}}{\mu_B|g_F|}\right)\hat{F}_z\\ &+ \left(B_\pi\exp(i \pm \omega_{AC}t) + B_\pi^*\exp(i \mp \omega_{AC}t)\right)\hat{F}_\pi\\ &+ \hat{U}_\pm\left(\frac{1}{\sqrt{2}}(\hat{F}_+B_+ + \hat{F}_-B_-)\exp(-i\omega_{AC}t)\right)\hat{U}_\pm^\dagger + \mathbf{h.c.}\end{aligned} \tag{2.38}$$

The first term, that couples to $\hat{F}_z$, includes the resonant field term:

$$B_{res} = \frac{\hbar\omega_{AC}}{\mu_B|g_F|} \tag{2.39}$$

The resonant field term becomes equal to B_{DC} when $\omega_{AC} = \omega_{larmor}$. Choosing the AC field to be in the xy plane simplifies equation 2.38, as $B_\pi = 0$. To simplify the $\hat{U}_\pm$ terms, we invoke the Baker-Hausdorf-Campbell Lemma:

$$\exp\left(\alpha \hat{F}_z\right) \hat{F}_\pm \exp\left(\alpha \hat{F}_z\right) = \exp(\pm\alpha)\hat{F}_\pm \tag{2.40}$$

Applying these simplifications to equation 2.38 gives the new Hamiltonian:

$$\begin{aligned}\hat{H}_{rot} = \frac{\mu_B g_F}{2} \Big(& (B_{DC} - B_{res})\, \hat{F}_z \\ & + \frac{1}{\sqrt{2}} \Big(\exp(\mp i\varphi)\hat{F}_+ B_+ \left(1 + \exp(2i\omega_{AC}t)\right) \\ & + \exp(\pm i\varphi)\hat{F}_- B_- \left(1 + \exp(-2i\omega_{AC}t)\right) \\ & + \exp(\pm i\varphi)\hat{F}_+ B_-^* \left(1 + \exp(-2i\omega_{AC}t)\right) \\ & + \exp(\mp i\varphi)\hat{F}_- B_+^* \left(1 + \exp(2i\omega_{AC}t)\right) \Big) \Big)\end{aligned} \tag{2.41}$$

We can invoke the rotating wave approximation to see that terms with a frequency much higher than the rotational frequency ω_{AC} should average out over 1 cycle, having a net zero effect. As a result we can discard all the terms oscillating at $2\omega_{AC}$. Due to the two hyperfine manifolds having opposite larmor precession axes, given by the sign of their gyromagnetic ratio g_F, the rotating terms couple in opposite senses, we can split the Hamiltonian into two, depending on the manifold it couples, and discard counter rotating terms. Doing this leaves us with the Hamiltonian:

$$\begin{aligned}\hat{H}^\pm_{rot} = \frac{\mu_B g_F}{2} \Big(& (B_{DC} - B_{res})\, \hat{F}_z \\ & + \frac{1}{\sqrt{2}} \Big(\exp\Big(\pm i\varphi \hat{F}_\pm B_\pm + \exp(\mp i\varphi)\hat{F}_\mp B_\pm^* \Big) \Big)\end{aligned} \tag{2.42}$$

In which $\hat{H}^+_{rot}$ describes the coupling of atoms in the $F = I + J$ manifold, and $\hat{H}^-_{rot}$ describes the coupling of atoms in the $F = I - J$ manifold. We can define the effective Hamiltonian as:

$$\hat{H}^\pm_{\text{eff}} = \frac{\mu_B g_F}{2} \hat{F} \cdot \hat{B}^\pm_{\text{eff}} \tag{2.43}$$

Where the effective field in the rotating frame, $\hat{B}^{\pm}_{\text{eff}}$ is defined as:

$$\hat{B}^{\pm}_{\text{eff}} = (B_{DC} - B_{res})\,\hat{z} + \frac{1}{2}\left(\exp(\pm i\varphi)B_{\pm} + \exp(\mp i\varphi)B^{*}_{\pm}\right)\hat{\sigma}_{\pm} \tag{2.44}$$

The rabi frequency, or coupling strength, induced by this field is:

$$\hbar\Omega^{\pm} = \mu_B g_F |B_{\text{eff}}|. \tag{2.45}$$

In the rotated frame, the eigenstates of $\hat{H}_{\text{eff}}$ take the same form as the eigenstates of the DC case, but we must consider the rotated transformation of the $|F, m_F\rangle$ states : $|F, \bar{m}\rangle$. The eigenenergies of the rotated hamiltonian are:

$$E_{F,\bar{m}} = \mu_B g_F \bar{m}\sqrt{\frac{|B_{\pm}|^2}{2} + (B_{DC} - B_{res})^2} \tag{2.46}$$

Which are shown in Figure 2.7.

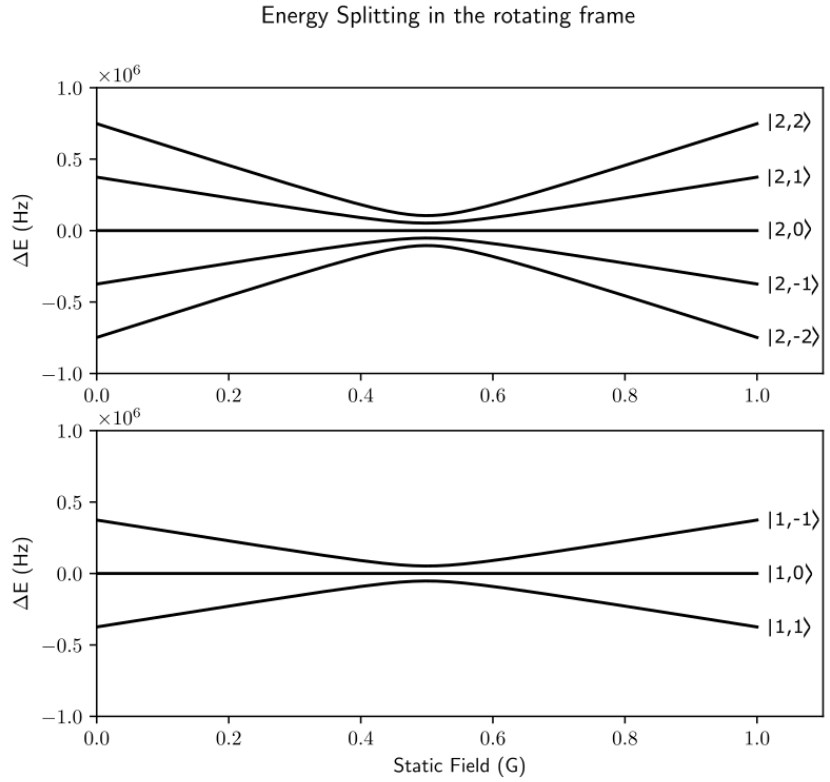

Figure 2.7: Energy Splitting of Hyperfine $|F, \bar{m}\rangle$ states in the rotating frame. The resonance is at 0.5 Gauss, where the rotating frame energy levels are separated by an energy of $h\Omega_{rf}$.

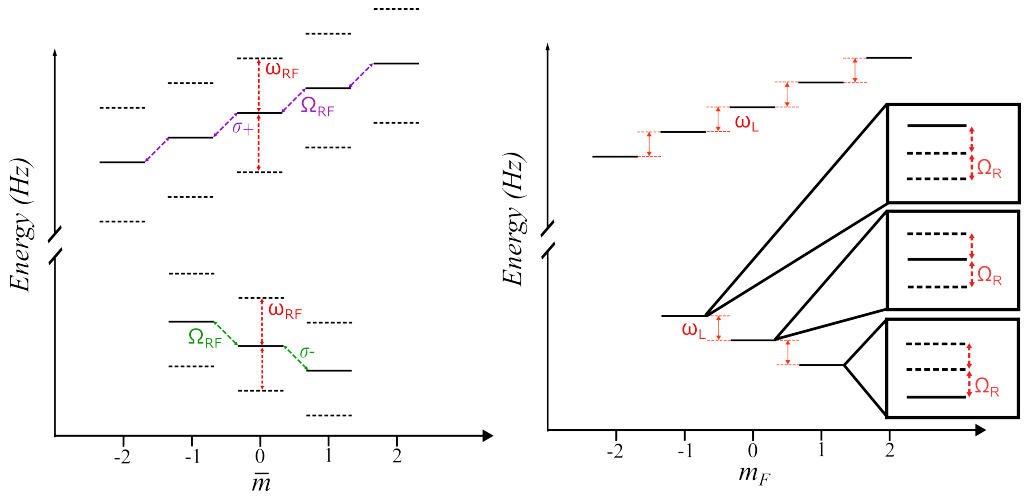

Figure 2.8: Left : Zeeman splitting of the $F = 1$ and $F = 2$ manifolds, in the RF-Dressed rotating frame. Right : Zeeman splitting of the $F = 1$ and $F = 2$ states in the RF-Dressed static lab frame.

The eigenenergies in the rotating frame are closest to zero when $B_{res} = B_{DC}$. With a splitting between the levels (at resonance) of:

$$\Delta E_{F,\bar{m}\to F,\bar{m}+1} = \frac{1}{\sqrt{2}}\mu_B g_F |B_\pm| = \hbar\Omega_\pm \tag{2.47}$$

When at resonance, B_{eff} appears to be a static field, in the rotating frame, that is perpendicular to the original quantisation axis in the $\hat{z}$ direction. This field drives the atomic dipole precession around itself at the rabi frequency. In the non-rotating lab frame, this precession about B_{eff} manifests as the magnetic dipole being driven through different $\bar{m}$ states. The apparent difference between the two reference frames, rotating, and not, is shown in figure 2.8.

2.2.4 The Floquet Approach

If we return to the rotating frame transformation, where we introduced the operator $\hat{U}_\pm$ we can note the periodic nature of the operator, we rewrite the operator as:

$$\hat{U}_\pm = A\exp\left(\pm i\omega_{AC} t\hat{F}_z\right) \tag{2.48}$$

Observing that $\hat{U}_{\pm}$ is a strictly periodic operator with period $T = \frac{2\pi}{\omega_{AC}}$. In a non-rotating frame, $\hat{U}_{\pm}$ has the effect of time-evolving that Hamiltonian $\hat{H}_{TOT}$ forwards by a time t [88]. Taking this operator as evolving our Hamiltonian from a given state at $t = \tau_0$ to $t = \tau$, we can observe that

$$\hat{U}_{\pm}(\tau, \tau_0) = \hat{U}_{\pm}(\tau + T, \tau_0) \tag{2.49}$$

due to the oscillatory nature of $\hat{U}_{pm}$. From this we can define a fast action operator that allows us to explore the time-dependent potential landscape.

$$\exp\Big(-i\hat{K}_F(t)\Big) = \hat{U}_{\pm}(\tau, \tau_0) \exp\left(i\mathcal{H}_F \frac{(\tau - \tau_0)}{\hbar}\right) \tag{2.50}$$

Here we introduce two operators: $\mathcal{H}_F$ is a time-dependent Hermitian operator that transforms the Hamiltonian over a single period, and $\hat{K}_F(t)$ is a fast-action operator, named the 'stroboscopic kick' operator. This operator is arithmetically identical to the rotating frame transformation in the previous section, but provides a more robust description of the time dependent mechanics. As $\mathcal{H}_F$ is unitary, its eigenvalues ϵ_n take complex values with a magnitude of 1. From this we can define the Floquet multipliers as $\exp\big(-i\epsilon_n \frac{T}{\hbar}\big)$. As the values of $\mathcal{H}_F$ remain invariant on periodic transformations, the eigenvalues are not uniquely defined, and take values of ϵ_n mod $\hbar\omega_{AC}$. These higher eigenvalues are the quasienergies of the system. Defining the periodic eigenstates $|n[\tau_0]\rangle$ we may write:

$$\mathcal{H}_F |n[\tau_0]\rangle = \epsilon_n |n[\tau_0]\rangle \tag{2.51}$$

Considering the atoms initial state $|\psi(\tau_0)\rangle$ we can find the time evolution:

$$|\psi(\tau)\rangle = \hat{U}_{\pm}(\tau, \tau_0) |\psi(\tau_0)\rangle \tag{2.52}$$

The initial state can be expanded as:

$$\begin{aligned} |\psi(\tau_0)\rangle &= \sum_n |n\rangle \langle n|\psi(\tau_0)\rangle \\ &= \sum_n a_n |n\rangle \end{aligned} \tag{2.53}$$

We can then write the evolved state $|\psi(\tau\rangle$ as:

$$\begin{aligned} |\psi(\tau\rangle &= \sum_n a_n \exp\Big(-i\hat{K}_F(\tau)\Big) \exp\left(\frac{-i\mathcal{H}_F\tau}{\hbar}\right)|n\rangle \\ &= \sum_n a_n \exp\Big(-i\hat{K}_F(\tau)\Big) \exp\left(\frac{-i\epsilon_n\tau}{\hbar}\right)|n\rangle \end{aligned} \tag{2.54}$$

Here we introduce the Floquet modes $|u_n(\tau\rangle$, which are defined as:

$$|u_n(\tau\rangle = \exp\Big(-i\hat{K}_F(\tau)\Big)|n\rangle \tag{2.55}$$

Where they inherit the periodic nature of the Hamiltonian:

$$|u_n(\tau\rangle = |u_n(\tau + T\rangle \tag{2.56}$$

Equation 2.54 defines the Floquet states $|\psi(\tau\rangle$, and reveals their periodic nature. Due to the periodicity of the eigenvalues(ϵ_n mod $\hbar\omega_{AC}$), we reveal the existence of phantom energy levels that exist at energy values that are integer multiples of $\hbar\omega_{AC}$. This effect can be understood as arising due to the absorption or stimulated emission of photons from the driving field. This is shown by the Band structure of the energy levels shown in Figure 2.9.

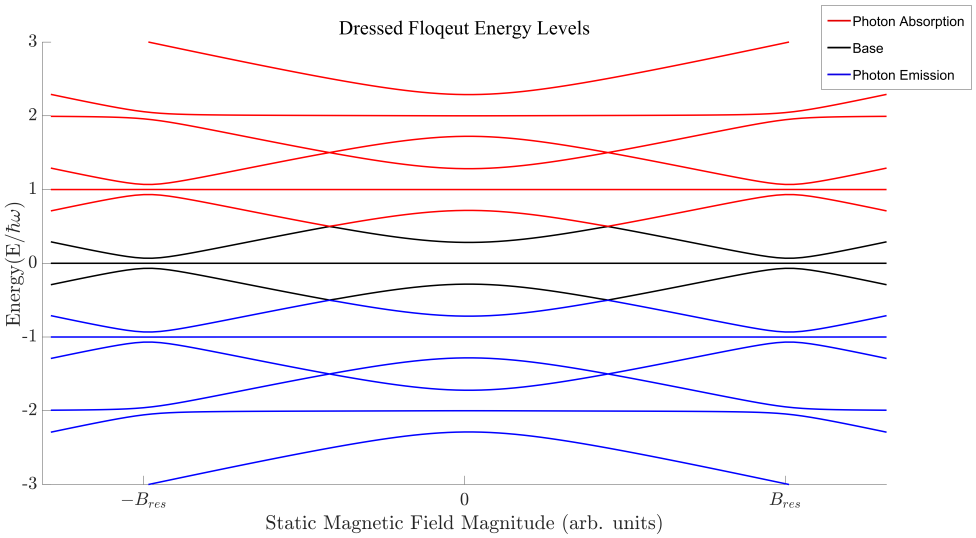

Figure 2.9: Floquet dressed energy levels containing the $+2, +1, 0, -1$, and -2 groups. Red energy levels correspond to those in which the atom has absorbed RF photons to reach, whereas blue corresponds to energy levels that the atom must emit a photon to reach.

Chapter 3

Ultracold atom manipulation

The process of creating a fully-trapped, atomic interferometer requires a high degree of control over both an atom clouds internal energy levels, such that a coherent superposition is able to be generated, and the trapping scheme itself. Maximising the number of atoms present through these processes is of importance, as the signal to noise ratio scales based on the square root of the atom number. This chapter will provide a comprehensive guide through the various methods and equipment required to realise the interferometer, as outlined in Figure 3.1. The chapter will be split into 3 parts: The first will describe the theory behind many of the experimental techniques used in this project, the second will provide a detailed view into the equipment and setup required to bring this project to life, and the third will tie it all together, taking us through the procedure, from room temperature atoms deposited into a vacuum chamber, to loading sub milikelvin atoms in a ringtrap, and driving them adiabatically around the ring.

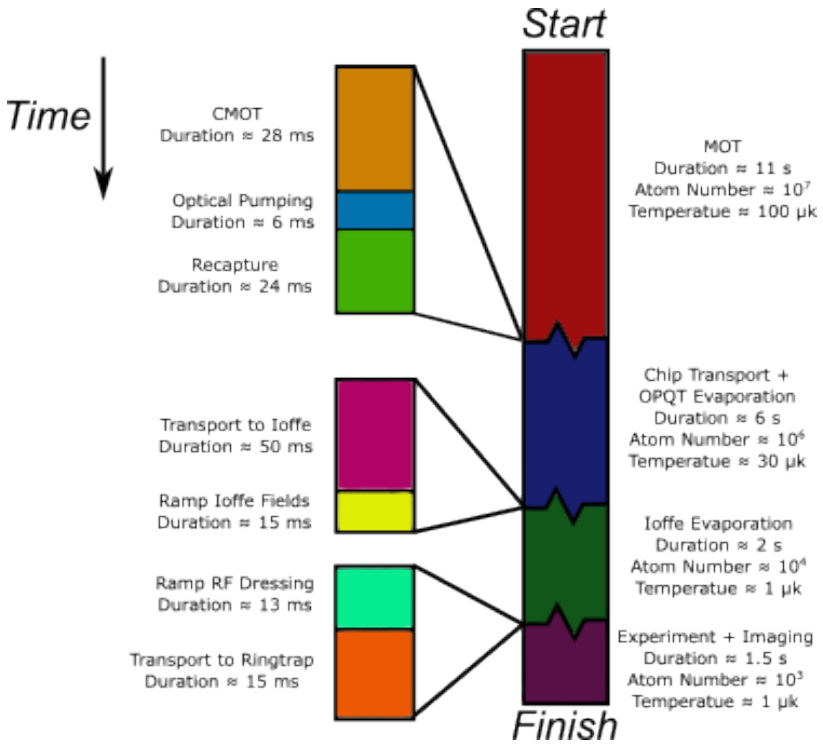

Figure 3.1: Diagram showing the steps, and their respective durations, for the experimental procedure. The major stages, on the right, are accompanied by rough estimates of atom numbers, and atomic cloud temperatures.

3.1 Techniques in Atomic Manipulation

This section aims to provide an overview of the techniques used throughout this experiment. It will provide both justification for the methods used, as well as a theoretical overview as to why the methods work, and how an experiment must be tuned to make the most out of the techniques. Many of the techniques listed here are commonplace amongst cold atoms experiments, and as such can be found in textbooks such as [61]

3.1.1 Magnetic Trapping of Atoms

Proper manipulation of atoms has the main requirement that atoms are able to be trapped, as untrapped atomic clouds quickly disperse and are lost. To do this we only have to refer back to the energy shift due to Zeeman splitting that occurs for an atom in the presence of a static magnetic field.

Taking the F=2 state, the magnetic sublevels can be split into three groups based on their behaviours. The $|2,2\rangle$ and $|2,1\rangle$ states increase in potential as magnetic field strength increases, and as such are weak-field seeking. The $|2,0\rangle$ state is magnetically insensitive and as such can be ignored. The $|2,-2\rangle$ and $|2,-1\rangle$ have a negative energy shift in the presence of a magnetic field and as such are high-field seeking. High field seeking states are fundamentally untrappable as, due to a selective case of Earnshaws theorem, there is no static configuration of currents that can produce a local field maxima outside of the current source [10]. Weak-field seeking states however are trappable, and all that has to be done to do so is to produce a local field minimum. For use in the experiment, magnetic trapping fields have a number of criteria that must be met:

Confinement The field must be able to confine atoms, meaning atoms must stay trapped. This includes creating a deep enough potential such that the thermal energy of atoms does not allow them to escape, and having a high enough gradient to levitate atoms against gravity.

Robustness The trap must be robust enough to outside noise as to not interfere with the internal states of the trapped atoms.

Lifetime Loss channels in the trap should be minimal in a way to maximise atom number over time.

The Magnetic Quadrupole

The magnetic quadrupole trap is one of the foundations of cold atom experiments due to its simplicity and functionality. All that is required to form a basic quadrupole trap is a pair of current-loops propagating in opposite directions. Generally this takes the form of two coils of wire in an anti-helmholtz configuration, in which the two coils share a central axis but are wound in opposite handed ways. The field geometry produced by such an arrangement, at the centre of the trap, can be generalised as:

$$\overrightarrow{B} = \alpha\hat{\boldsymbol{x}} + \alpha\hat{\boldsymbol{y}} + 2\alpha\hat{\boldsymbol{z}} \tag{3.1}$$

Where α is the gradient of the magnetic field, which for a quadrupole field created via anti-Helmholtz coils is given by:

$$\alpha = \frac{1}{\mu_0}\frac{3}{2}NI\frac{r^2 d}{(r^2 + \frac{d^2}{4})^{\frac{5}{2}}} \tag{3.2}$$

Where NI is the number of turns in the coil N, multiplied by the current through the coil, I, which will be referred to as the current-turns of the coil henceforth, r is the radius of the coils, and d is the displacement of the coils from their centre point (or half the distance between the coils). It can be seen from equation 3.2 that the maximum gradient for the quadrupole is given when $r = d$, or in words, when the radius of coils is equal to half the distance between them.

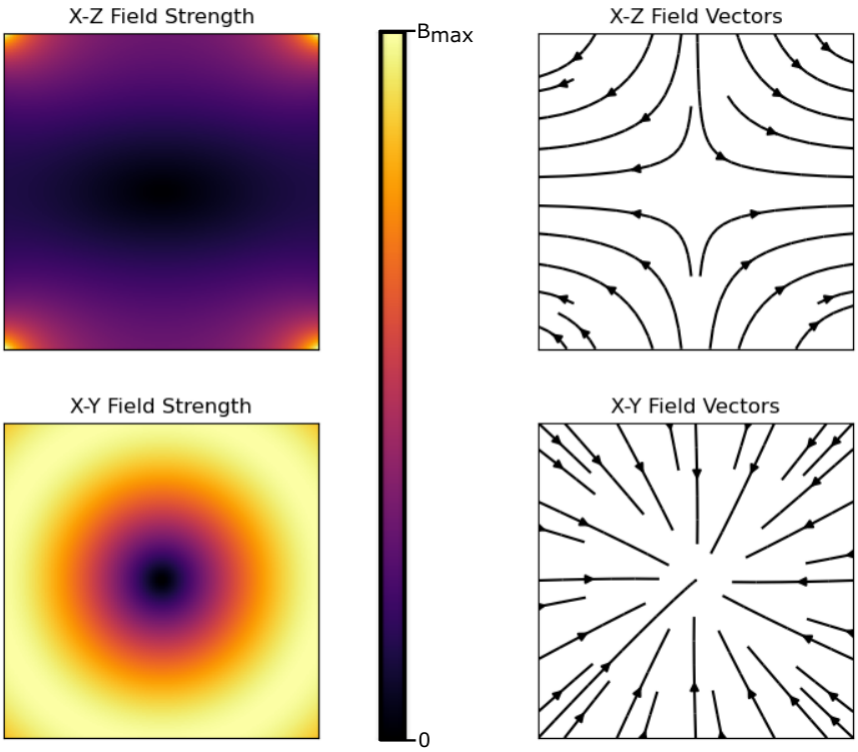

Figure 3.2: Simulated fields of a quadrupole field generated by an anti-Helmholtz coil pair, where $r = d$. The left side depicts the magnetic field strength (in arbitrary units), the right side depicts the direction of the magnetic fields. The top and bottom rows correspond to bisections of the central X-Z and X-Y planes respectively.

The gradient in the z-direction provides the levitating force to resist

gravity, in this quadrupole trap, the z gradient is double the trap gradient in other directions, making levitation easier, as a result we obtain a lower bound for the gradient [33]:

$$\alpha \geq \frac{1}{2}\frac{m_a g}{\mu_B g_F m_F} \tag{3.3}$$

Where m_a is the mass of the atom, and g is the acceleration due to gravity. For ^{87}Rb the gradient needed to levitate is 32 Gcm^{-1} for states with $|m_F| = 1$, and 16 Gcm^{-1} for states with $|m_F| = 2$

3.1.2 The Ringtrap Quadrupole

A variant of the standard 3D Helmholtz quadrupole trap, the ringtrap quadrupole utilises a set of 4 concentric, in plane currents, each propagating in a circular path in alternating directions. This setup allows for the creation of a quadrupole trap that takes the form of a 2d slice through the X-Y plane, extended in a ring shape above the centre of the current loops. The field at a point (x, y, z), close to the quadrupole zero is assumed to be given by the equation:

$$\overrightarrow{B} = \alpha\sqrt{\left(\sqrt{x^2+y^2} - R\right)^2 + (z - z_0)^2}, \tag{3.4}$$

where R is the distance between the centre of the current loops and the centre of the ring. The field geometry is shown in Figure 3.3 The height of the ringtrap z_0 is given by [12]:

$$z_0 = \frac{1}{2}\sqrt{4dR + 4R^2 - w^2}, \tag{3.5}$$

where w is the width of the wire loops, and d is the distance between an outer wire, and its nearest inner neighbour. The field gradient, α is given by:

$$\alpha = \frac{2\mu_0 I}{\pi}\frac{z_0 d}{R(d+R)(d+2R-w)(d+2R+w)} \tag{3.6}$$

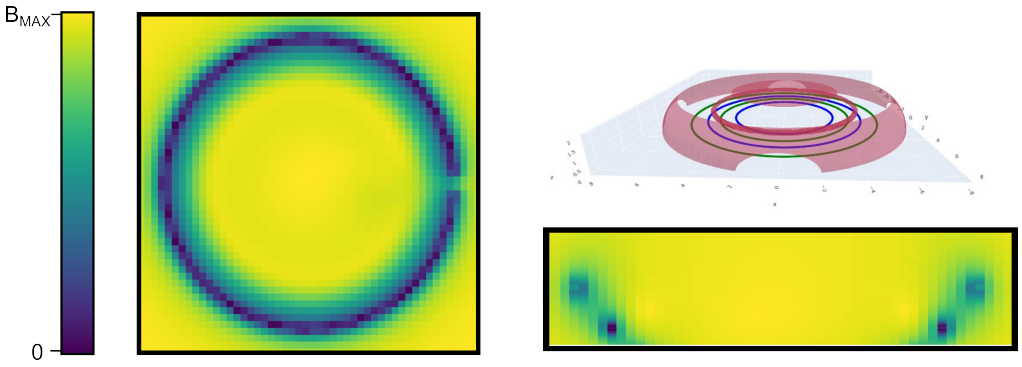

Figure 3.3: Simulated field magnitudes of the a Ringtrap Quadrupole. Left :X-Y plane view. Top-Right : Iso-surface of low field value, with current loops showing, green rings are clockwise, and blue are counter-clockwise. Bottom Left : X-Z plane view.

3.1.3 Magneto-Optical Trapping

Beginning the experiment, atoms are dispensed into a vacuum chamber through a Rubidium getter dispenser, which dispenses Rubidium atoms, in their natural abundance (20/80 between ^{85}Rb and ^{87}Rb). To begin the experiment, we need a way of selecting the ^{87}Rb isotope, driving its internal states into magnetically trappable ones, and to cool the atomic cloud down such that the average atom does not have enough kinetic energy to simply escape a magnetic trap. Thankfully all three of these criteria can be achieved through a Magneto-Optical Trap (MOT for short), and its following stages. The MOT, as the name suggests, makes use of both magnetic, and optical fields to both confine, and cool atomic clouds. Atoms are exposed to both a quadrupole field, and 6 orthogonal light fields, each with a σ_+ polarisation with respect to the quadrupole field, which are red-detuned from the $5^2\mathcal{S}_{\frac{1}{2}} \rightarrow 5^2\mathcal{P}_{\frac{1}{2}}$ transition. This detuning allows the optical field to provide both an additional confining force, in conjunction with a quadrupole magnetic field, and also selectively reduce the kinetic energies of atoms within the cloud. These optically induced forces come from the fact that when an atom absorbs a photon from a laser beam, it gains a momentum of $\hbar k$ in the direction of the laser, and is excited to a higher energy level. The spontaneous emission of the photon when the atoms decays back to its ground state, however, is omni-directional, and as such has no average direction of momentum change for the atoms. This

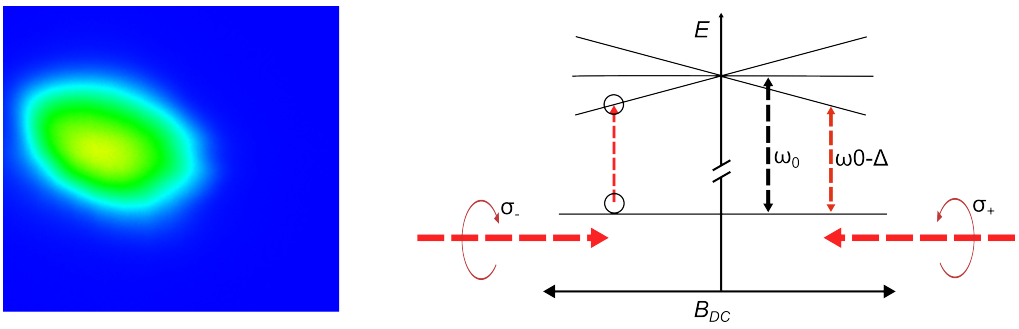

Figure 3.4: Left : False colour image of the MOT fluorescence. Right : Illustration demonstrating the principle of positionally dependent MOT forces along a single principle axis.

is exploited in two ways, firstly through the use of the Zeeman shift induced by the quadrupole field, as the untrappable states in the $5^2\mathcal{P}_{\frac{1}{2}}$ have a lowered potential in higher field values, meaning atoms further from the quadrupole centre see a smaller transition frequency, and are thus their resonance is closer to the optical fields frequency. Secondly, atoms with high velocities away from the quadrupole centre see the optical field that they are travelling into blue detuned, due to the Doppler effect, which brings the optical field closer to transition resonance in the atoms moving frame of reference. In both cases the optical field being closer to the transition resonance causes an increased probability of the atoms absorbing a photon from the optical field, and feeling a net force towards the centre of the trap. For these effects to occur, we aim to drive a transition between specific m_F states, this is selected for by controlling the polarisation of the incoming light to be σ_+ with respect to the magnetic field (as shown in Figure 3.4). We expect the force on an atom in the MOT, then, to be dependent on both velocity ,v, and position , x [81].

$$F_{MOT} = -av - abx \tag{3.7}$$

where a is a constant related to the likelihood of photon absorption by an atom, and b is related to the Zeeman splitting of the excited state.

$$a = \frac{16\hbar k^2\Omega^2\Delta}{(\Gamma^2 + 4\Omega^2)^2} \qquad b = \frac{1}{k}\frac{g_J\mu_B\alpha}{\hbar}, \tag{3.8}$$

where Ω is the rabi frequency of the optical transition, Δ is the detuning of the optical field from the $|J,0\rangle \rightarrow |J',-1\rangle$ transition, and Γ is the damping coefficient.

This force gives rise to the optical molasses, wherein atoms are pushed towards the centre of the quadrupole, and cooled. The recoil effect that occurs due to spontaneous emission, whilst having not net force on the atom, does give it a small velocity in a random direction. This limits the minimum momentum of an atoms cooled via Doppler cooling to $\hbar k$, setting a lower limit for the temperature of the cloud. The minimum temperature of the cloud is also limited bythe natural linewidth of the driven transition, shown in the Doppler limit [54] :

$$T_{min} = \frac{\hbar\gamma}{2k_B} \tag{3.9}$$

Where k_B is the Boltzmann constant. The natural linewidth of the $5^2\mathcal{S}_{\frac{1}{2}} \rightarrow 5^2\mathcal{P}_{\frac{1}{2}}$ transition is $\gamma = 2\pi \times 6.065$ MHz, leading to a minimum temperature via Doppler cooling of $T_{min} = 145\mu k$

The spontaneous emission of photons from atoms allows for the direct viewing of the MOT, as it fluoresces at the $5^2\mathcal{S}_{\frac{1}{2}} \rightarrow 5^2\mathcal{P}_{\frac{1}{2}}$ frequency, which is ≈ 780nm. Sadly this is just outside of the human eyes visble range, but means that the MOT is directly observable through use of a camera with no Infra-red filter!

Compressed-MOT stage

Before loading atoms into a purely magnetic trap, it would be ideal to cool below the Doppler limit. Achieving this is possible through the use of the Compressed-MOT (or CMOT for short) stage [69]. This method works by first ramping down the quadrupole trapping fields, allowing the atomic cloud to ballistically expand, whilst also beginning to fall under the effects of gravity. The cooler beam is then rapidly ramped away from resonance, such that the scattering rate amongst slower atoms decreases, this causes a collapse in the clouds spatial distribution, compressing it and lowering the overall temperature of the cloud. It is also likely, though not taken into account, that we see further atomic cooling as a result of polarisation gradient cooling in the Z-direction, in which a standing wave produced by

the superposition of σ_+ and σ_- components of the Z beam cause atoms with some velocity component in the z direction to absorb more photons in the direction countering their velocities. The CMOT stage lasts for only a few milliseconds, as any longer would cause the free-falling motion of the atoms to become a concern for future trapping.

Optical Pumping

Crucial to the magnetic trapping of atoms is that all of the atoms in a given ensemble reside in trappable Zeeman sub-states. This is not true of atoms just after a MOT stage, as the photon decay from Doppler cooling leaves atoms populating a wide range of states. To fix this we make use of the polarisation of an optical field, along with selection rules for photon decay, to drive atoms into magnetically sensitive states. Atoms driven between the $F = 2$ and $F' = 2$ manifolds via a σ_+ polarised optical field will see the respective m_F sublevels increase by $+1$. This, combined with the spontaneous emission being able to return the atom to a substate with $m_F = \pm 1, 0$ then the atoms trend towards higher m_F states. This process is illustrated in Figure 3.5.The opposite is also true, where a σ_- polarised optical field would trend atoms towards their lowest m_F states. Performing this experimentally requires a local magnetic field, with which the optical field can be polarised with respect to. We achieve this by applying a bias field in the X direction whilst atoms are in free-fall immediately after the CMOT stage, they typical optical pumping stage takes only a few milliseconds before reaching saturation.

Transfer to fully magnetic trapping

With atoms cooled below the Doppler limit, and optically pumped into trappable Zeeman states, we can begin trapping them without the need for optical fields. The first step in this process is catching the atoms, which are in gravitational free-fall after the optical pumping stage. This is done by ramping up a quadrupole field in such a way that it slows, and then traps the atoms as smoothly as possible. This process is incredibly sensitive to even small changes in quadrupole positioning, as positioning it too far away from the atoms will mean they simply fall straight past

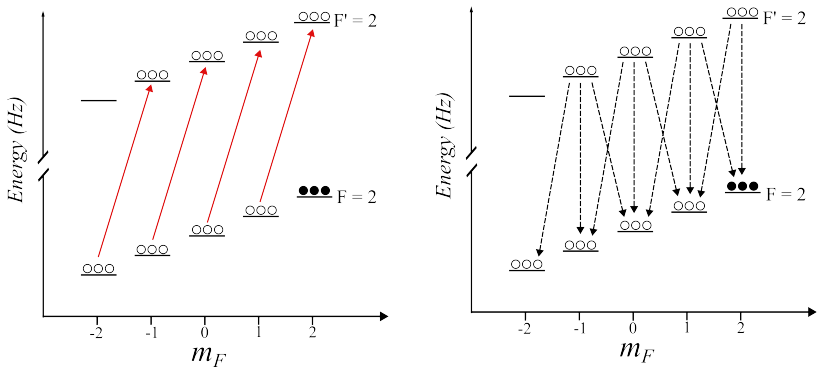

Figure 3.5: Illustration showing the process of optical pumping . Left : A σ_+ laser beam always transfers atoms to a state with $m'_F = m_F + 1$, leaving the maximal m_F state transparent to the beam. Right : Atoms decay from the excited state to $m'_F = m_F \pm (1, 0)$, meaning that over time, all atoms will occupy the maximal m_F state.

it and are not trapped, but position it too close and the jerking motion from quickly stopping the atoms causes them to heat up. With atoms now confined into a purely magnetic quadrupole trap, we can use bias fields to move the quadrupole field to above the atom chip, where the majority of experimental procedure takes place.

3.1.4 Atom Measurement Techniques

Being able to accurately measure multiple properties of the atom cloud is of vital importance, little can be done to optimise the atom number and temperature if they cannot be measured. The method through which this experiment can see the atom cloud is via Absorption Imaging. Atoms absorb light resonant to their transitions and scatter it, making them opaque to light of the correct frequency. By backlighting atoms with light resonant to an atomic transition, and measuring the resultant on a CCD camera sensitive the frequency, we can see the 'shadow' of the atomic cloud. This image of the atoms can be combined with two other images, one of the same frame with the light on, to measure the background features of the image (experimental features like atom chips or antennae, camera marks, etc.) and one image with no light to measure dark currents in the CCD pixels, These images, and the resulting analysed image can be seen in Figure 3.6. By taking the intensity of these three images across every pixel in

the camera, the optical density (O.D.) can be calculated.

$$O.D. = \ln \frac{I_l - Id}{I_a - I_d} \tag{3.10}$$

Where I_a, I_l, and I_d are the intensities of the pixels for the atom, light, and dark images respectively. Knowing the optical density of an image, the magnification M, and pixel width x of our camera allows for the calculation of an atom number by summing the optical densities across the 2D plane of the image.

$$N_a = \frac{x^2}{\sigma_0 M^2} \sum_{x,y} O.D._{x,y} \tag{3.11}$$

Where σ_0 is the resonant cross section of the atom. Absorption imaging is a powerful tool that allows for the measurement of the location and number of atoms at any point in the sequence, with the limitation that it is a destructive measurement, meaning it ends any given experimental sequence. Absorption imaging becomes even more powerful when combined with other techniques that can convert properties of the atomic cloud into a change in atom number, or atom cloud size/location.

RF Spectroscopy

Section 2.2.3 described how RF magnetic fields could resonantly drive the spin of atoms that had a larmor precession frequency equal to the RF frequency. This effect can be utilised to perform spectroscopy, as a pulse of RF power, at a given frequency can be used to resonantly drive atoms from their trapped $|F, m_F\rangle$ state, to an untrapped one. For atoms in a magnetic trap, the Zeeman shift of atoms at higher field value increases the resonance frequency of the RF probe, meaning that RF spectroscopy directly probes the thermal distribution of atoms about a magnetic trap.

The probability of finding an atoms at a field value of B, provided the cloud has a definite temperature T is:

$$P(B,T) = \frac{1}{Z} \exp\left(-\frac{\mu_B g_F m_F B}{k_B T}\right) \tag{3.12}$$

where Z is the partition function that serves as a normalisation constant. By using the relationship between a probes frequency, ω_P, and it energy

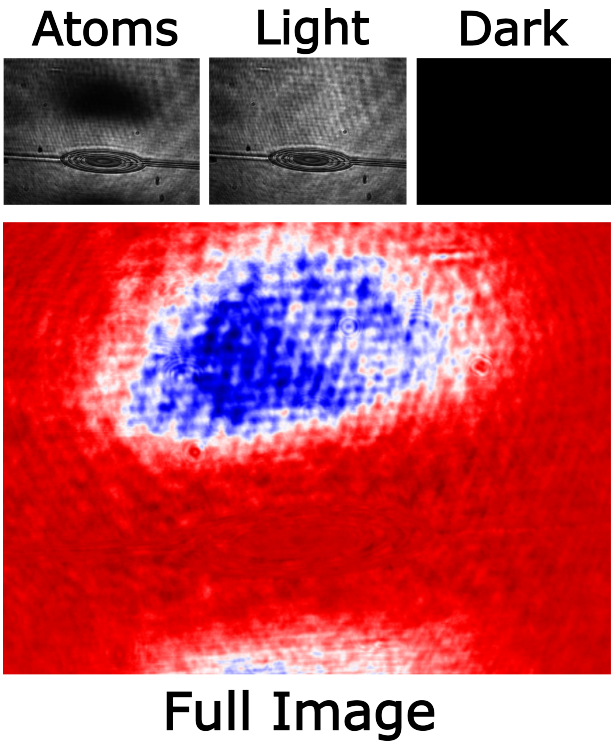

Figure 3.6: Principle of Absorptive imaging : The atoms, light, and dark image are combined to produce the optical density image, shown with false colours. this image can be analysed to calculate the amount of atoms present for a given shot.

we can relate the magnetic field magnitude to a transition frequency:

$$\omega_P = \frac{\mu_B m_F g_F B}{h} \tag{3.13}$$

Which allows us to convert Equation 3.12 into frequency space:

$$P(\omega_P, T) = \frac{1}{Z(\omega_P)} \exp\left(\frac{h\omega_P}{k_B T}\right) \tag{3.14}$$

This result (by no means being unexpected or groundbreaking) allows us to infer that the maxwell-Boltzmann distribution of atoms energies is directly observable via RF spectroscopy. This allows us to use RF spectroscopy as thermometry, as provided we are able to express the Partition function, we can fit a maxwell Boltzmann distribution to the spectroscopy measurements.

Figure 3.7 is an example of how such a spectrum is laid out, we probe the atom cloud with differing frequencies of RF, when that RF is resonant with an atoms local larmor precession frequency, it is ejected from the trap, and we see a reduction in atom number. By graphing the atom number as a function of probe frequency we can observe the thermal distribution of atoms in a trap.

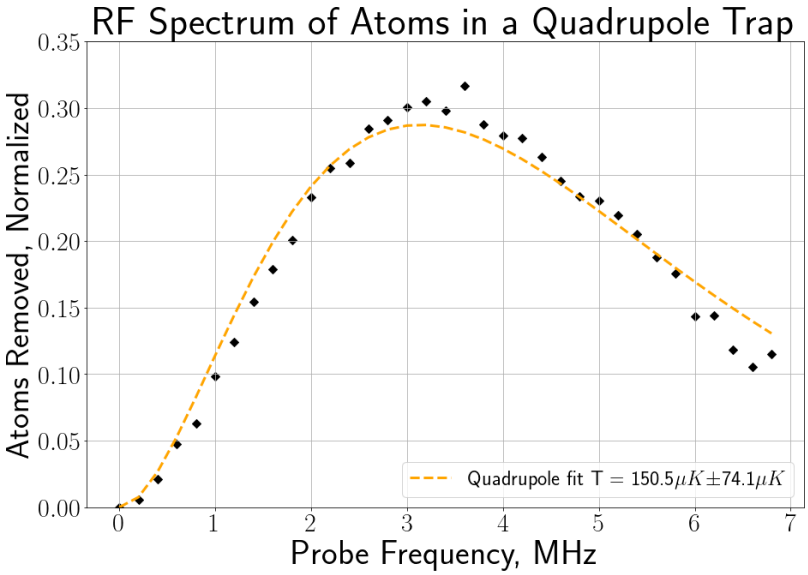

Figure 3.7: RF spectroscopic measurement of quadrupole trapped atoms shortly after optical pumping. We can use the removal distribution to estimate the cloud temperature at $\approx 150\mu k$ - Just above the Doppler limit.

All data points for such spectra are processed using absorption spectroscopy that is analysed via Python script. To avoid background noise in such images that arises due to mechanical oscillations, and laser fluctuation noise, the analysis is aided by Principal component analysis (Appendix A provides more details on this methodology). A thermal distribution is fit onto the data points, and plotted alongside it, though sometimes it is instead more useful to plot straight lines between points as a sort of linear interpolation of the data, to better see spectroscopic features. Due to the inclusion of Principal component analysis, error bars are not shown, though the precision of any given measurement is dependent on some function of total atom number.

3.1.5 Evaporative Cooling

The Doppler limit discussed earlier places a lower bound on the temperature of atomic clouds created in a MOT, if we wish to go any further, we must make use of another method to cool atom clouds further: Evaporative cooling. This method makes use of the fact that RF frequencies can be used to selectively remove atoms of a specific energy from the trap. We

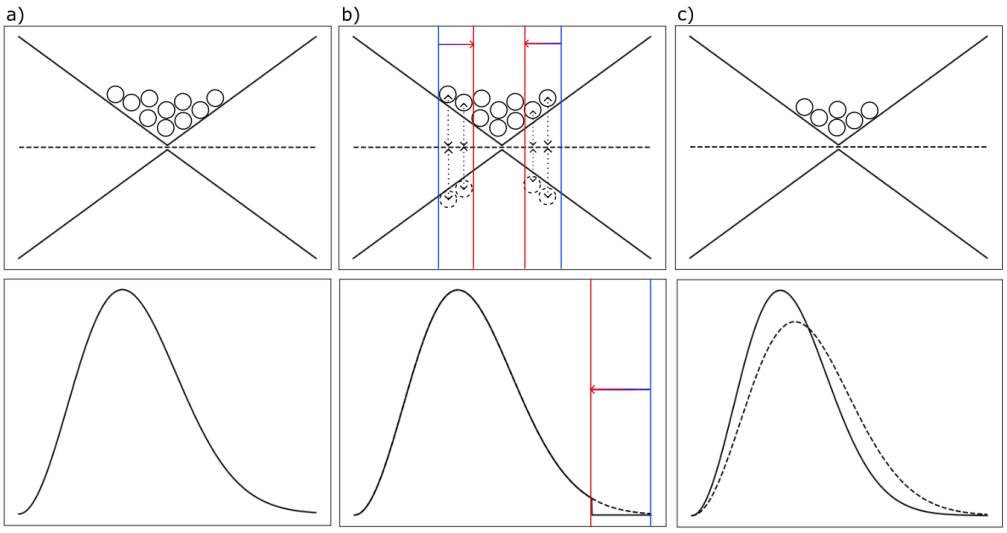

Figure 3.8: Illustration of the principle of RF evaporative cooling. a) The atomic cloud in the trap is distributed thermally about the magnetic field. b) An AC field is frequency ramped through the atomic distribution, transferring atoms it crosses into untrappable states, and expelling them from the trap. c) With the highest energy atoms expelled, the cloud rethermalises, and is now colder.

can use this to selectively remove atoms with a higher energy from the distribution, lowering the average energy of the entire atoms cloud. We can make use of this process experimentally by ramping an RF field's frequency down, from being blue detuned to just passing through the tail end of the thermal distribution. This RF field is referred to as an RF knife, as it 'cuts' into the atomic distribution, as can be seen from Figure 3.8. Any atoms that the RF knife cuts through are adiabatically transferred into an untrappable m_F states. The rate at which the RF knife can be ramped down into the distribution and thus the cooling rate is primarily limited by the rethermalization rate of the atomic cloud. We assume that the rethermalization of the cloud is dependent on elastic collisions between atoms. The rate at which elastic collisions occur in an atomic cloud is given as [23]:

$$\Gamma_{col} = \langle \bar{v} \rangle \langle n \rangle \sigma \tag{3.15}$$

Here we introduce $\langle \bar{v} \rangle$ as the mean squared velocity of atoms within the thermal ensemble, σ as the cross sectional area for elastic collisions, for a given atom in a given state, and $\langle n \rangle$ as the number density of atoms in

the trap. For ^{87}Rb in the $|2,2\rangle$ state, the cross sectional area can be found from [82]

$$\sigma = 4\pi(109a_0)^2 \tag{3.16}$$

where a_0 is the Bohr radius. We also note that the average velocity of an atom with mass M is :

$$\bar{v} = \sqrt{\frac{8k_BT}{\pi M}} \tag{3.17}$$

In most cases (depending on the geometry of the trapping potential) a reduction in cloud temperature results in an overall increase in collision rate, this process can compound upon itself, culminating in a runaway effect in which there is little to not limit on the rate at which the Rf knife frequency can be ramped down. From this we can expect to require a cooling profile in which the speed of Rf knife ramping begins slow, and speeds up as the cloud gets cooler. Despite this, in both the (see Figure 3.9, and other experiments found in literature [17], we find the opposite cooling profile to be better in achieving colder atom clouds.

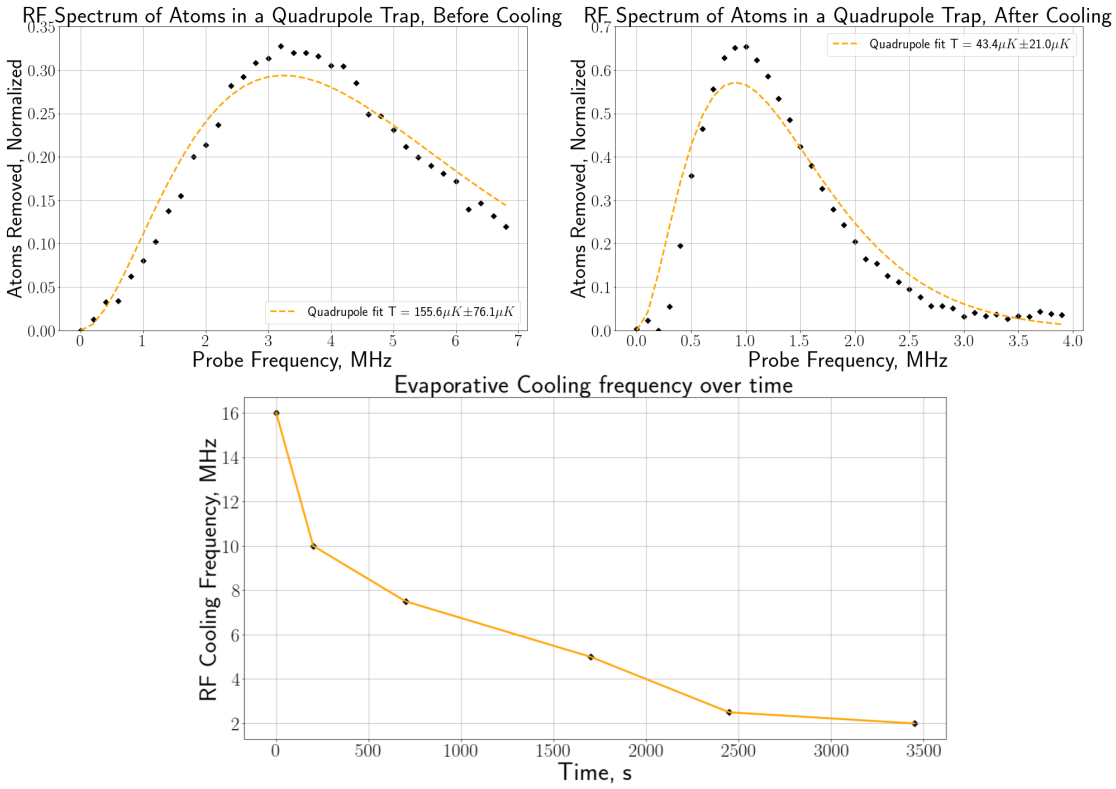

Figure 3.9: RF spectra in an (almost) Quadrupole trap before and after RF evaporative cooling, along with the RF knife frequency profile used to achieve such cooling.

It should also be noted that evaporative cooling is by definition, a lossy process, and the trade-off for cooling down clouds to very low temperatures is losing imaging contrast due to ending up with very low atom numbers. Cooling sequences typically last from 100's of milliseconds, to multiple seconds, meaning that they can only really be performed in long-lifetime traps.

3.1.6 Majorana spin flip losses

Obtaining longer lifetime atom traps means eliminating channels by which atoms are lost. One major channel for atomic losses in this experiment is due to Majorana spin-flip losses. When atoms transverse the region around the field zero, provided that they are slow enough, they adiabatically follow the field. When crossing over the field zero, however, the field direction instantly flips, in the atomic dipoles reference frame, leading to a situation

where the atomic dipole is now anti-parallel to the magnetic field, effectively driving it into an untrappable m_F state. This non-adiabatic mechanism serves as a loss channel for atoms confined in quadrupole traps that mainly affects ultra cold atoms in high gradient trapping potentials. For spin 1/2 particles, the loss rate due to majorana spin flips can be shown to be [15]:

$$\omega_f = \frac{\pi\omega_i}{2}\exp\left\{-\frac{\pi k_i^2 b_i^2}{4}\right\} \tag{3.18}$$

Where ω_i is the trap oscillation frequency, b_i is the length of such oscillations, and k_f is the momentum of the atom as it passes through the trap zero. For a relatively hot cloud of atoms, in a low-gradient trap, the exponential decay dominates, and losses are low. However,for lower temperature clouds, or cloud confined in trapping potentials with greater gradients, the close proximity of atomic trap oscillations to the field zero greatly increases the rate of majorana losses. Avoiding majorana losses in magnetic trapping potentials is only possible by introducing methods that deny atoms the ability to reach a field zero point, to this end we employ two different methods : Optically-plugged Quadrupole traps, and Ioffe-Pritchard traps.

Optically-Plugged Quadrupole trap

The quadrupole can also be modified in a more static manner to avoid spin flip losses via use of an optical plug. An optical plug makes use of the AC stark shift induced via blue detuned light, to produce a repulsive potential barrier to prevent atoms from reaching the field zero. For an arbitrary two level system, with ground and excited states $|g\rangle$ and $|e\rangle$ respectively, the shift in energy induced by an off-resonance beam of light is shown to be [41]:

$$\Delta E = \pm\frac{|\langle e|\,\mu\,|g\rangle|^2}{\Delta}|E|^2 = \pm\frac{3\pi c^2}{2\omega_0^3}\frac{\Gamma}{\Delta}I \tag{3.19}$$

Here we see that the energy shift induced is inversely proportional to the beam detuning. $\Delta = \omega_0 - \omega$, but directly proportional to the intensity of light, I. We also introduce the decay rate from the excited state to the ground state, Γ. Using this, we can obtain the potential shift induced by this interaction on a ^{87}Rb atom, with a laser beam intensity profile $I(r)$,

which couples the ground $5^2\mathcal{S}_{1/2}$ state to the $5^2\mathcal{P}_{1/2}$ and $5^2\mathcal{P}_{3/2}$ states.

$$U(r) = \frac{\pi c^2 \Gamma}{2\omega_0^3}\left(\frac{2 + P g_F m_F}{\Delta_2} + \frac{1 - P g_F m_F}{\Delta_1}\right) I(r) \tag{3.20}$$

Where Δ_1 and Δ_2 are the transition energies between the $5^2\mathcal{S}_{1/2}$ state, and the $5^2\mathcal{P}_{1/2}$ and $5^2\mathcal{P}_{3/2}$ states respectively, and P defines the laser polarisation ($P = 0$ for linearly polarised light, and $P = \pm 1$ for $\sigma_\pm$ polarised light, respectively. Taking the assumption that $|\Delta_1| \approx |\Delta_2| \gg |\Delta_2 - \Delta_1|$we can simplify Equation 3.20 to:

$$U(r) = \frac{3\pi c^2 \Gamma}{2\omega_0^3 \Delta} I(r) \tag{3.21}$$

This potential change forms a repulsive barrier for atoms attempting to enter the region illuminated by the light field. This works even if very few atoms are transferred to the excited state by that laser, i.e. $\Gamma \gg \Gamma_{SC}$. The scattering rate, Γ_{SC} can be shown to be:

$$\Gamma_{SC}(r) = \frac{3\pi c^2 \Gamma}{2\omega_0^3 \Delta^2} I(r) \tag{3.22}$$

As we wish to maximise the potential barrier, but reduce scattering rates to an absolute minimum, it is favourable to focus on maximising the detuning of the beam, rather than maximising the intensity (though maximising intensity is still desirable), to take advantage of the inverse square scaling on the scattering rate. Experimentally, we make use of a beam, blue detuned by 20nm from the D2 transition line (which is the greatest detuning we can achieve), with round 2W of laser power transmitted into the chamber. This beam is focused onto the quadrupole centre, repulsing atoms from the field zero. Experimentally, this technique allows us to create a trap with a lifetime of 11 seconds (see Figure 3.10), long enough to perform the evaporative cooling sequences.

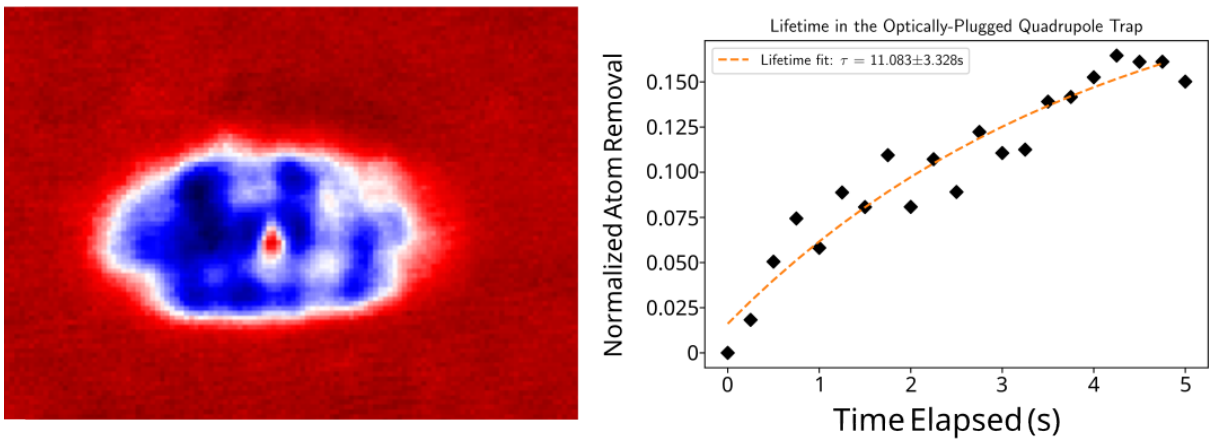

Figure 3.10: Left : Absorption imaging of $\approx 10^6$ atoms in the OPQT, the red hole in the centre is the focus of thee plug beam. Right : Lifetime plot of atoms in the OPQT, post evaporative cooling.

Ioffe-Pritchard Traps

A generalised term for any magnetic trapping scheme that does not form a field zero at its minima, but instead some arbitrary minimum field value, Ioffe-Pritchard traps come in many shapes and sizes [7, 39, 86]. Of particular interest to this experiment, however, is the Z-trap, as we are able to create an ad hoc Z-type trap using pre-existing conductor structures. Z trap is formed of a Z-shaped current-carrying conductor structure combined with a static bias field parallel to the plane of the Z shape. The result is a magnetic trap located above the central wire of the 'Z', with a trap field minimum that is adjustable in magnitude by simply changing the ratio between the field generated by the Z wire, and the planar field. We are able to create such a trap by utilising the lead wire of the conductor structure responsible for the ringtrap quadrupole. The slight hook shape where the curved conductor meets its lead wire forms a pseudo-z shape, and a bias field is applied. This Ioffe trap serves as the ideal location for the later stages of manipulation and cooling of atoms. The trap bottom is adjustable by simply changing the magnitude of the Bias field, allowing for dynamic control of the trap energetics in-sequence. The raised trap bottom also brings the atoms out of range of low frequency noise to the point at which we see a $\approx$ 10s lifetime in the trap. Because of this long life-

time, we are able to perform a very efficient RF-evaporation procedure on the atoms, allowing us to bring the atomic cloud down to sub-microkelvin temperatures.

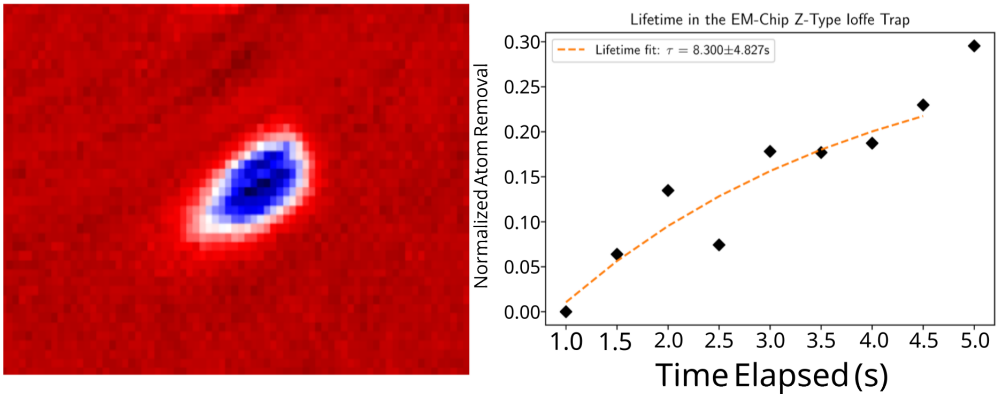

Figure 3.11: Left : Absorption imaging of $\approx 10^4$ atoms in the Z type Ioffe trap. In the top left of the image, the tracks to the ringtrap-generating coil-structure can be seen, as this Ioffe trap is created near to the ringtrap. Right : Lifetime plot of atoms in the Z type Ioffe trap, post evaporative cooling.

3.2 Radio-Frequency Dressed Potentials

Whilst static trapping methods allow for the creation and manipulation of Ultra-cold atomic cloud, and are able to produce stable trapping potentials close to a conductive surface, with multiple second lifetimes, it is the Radio-Frequency Dressed potential that lies at the heart of this interferometer. Through the use of AC magnetic fields applied to the trapping methods mentioned in the previous chapter, we are able to create traps for atoms that are resilient to noise, have interesting geometries, and are able to be dynamically manipulated. This section will provide a detailed description into the methods by which we make use of RF-Dressed potentials in the path towards the trapped atomic Sagnac interferometer.

3.2.1 RF Dressed Traps

In Chapter 2, we discussed how an AC magnetic field coupled to the atomic magnetic moment allowed for the creation of local potential minima at

resonant field values. We can expand upon this idea by considering the field geometry about a quadrupole, as seen in Section 3.1.1. The radial nature of the field strength means that the resonance condition will be fulfilled on the surface of an oblate spheroid, with a radius of $r_x = r_y = \frac{r_z}{2}$, we refer to this trap surface as the RF-dressed shell trap. The potential minima of the trap is directly proportional to the coupling strength of the RF-dressing field to the atoms, which in turn is governed by the magnitude of the RF-dressing field, and the relative orientation of the dressing field to the static magnetic field. We can see how this manifests by considering the application of a linear dressing field to a static Quadrupole trap; Regardless of the orientation of the dressing field, there will be some point on the surface of the dressed shell in which the dressing field is parallel to the static field, resulting in a region of zero coupling, and a point at which the dressing field and static field are perpendicular, leading to maximum coupling. We can see this directly by looking at atoms trapped in an RF-dressed quadrupole trap, such as in Figure 3.12, atoms seek out the region of minimum coupling and move to the point on the shell surface in which they see no coupling from the RF field. However, with no RF coupling, the atoms become undressed and thus untrapped, either falling to the centre of the quadrupole, or expelled from the trap entirely, depending on their state. This creates a major channel for atomic losses; to avoid this we can utilise RF fields polarised along more than 1 axis (such as circular polarisations) such that there is always some component of the dressing field perpendicular to the static field.

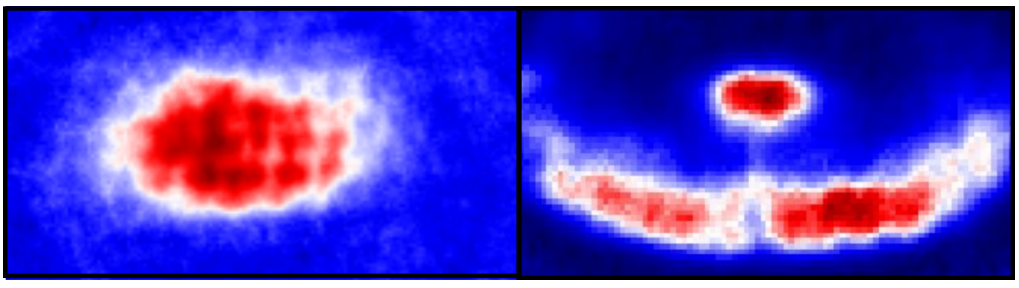

Figure 3.12: Left : Atoms confined in a bare quadrupole trap. Right : Atoms confined to an RF shell trap, we assume a linear polarisation in the z-direction, as such atoms are drawn to the bottom of the trap where the coupling tends to zero, and some have fallen through the hole in the shell into the bare quadrupole in the centre.

Frequency Heirarchy

One major benefit to using RF-Dressed potentials is that the process of trapping the atoms on a resonant shell raises the noise floor for the atoms to the dressing frequency. What this means in practice is that low frequency noise, especially the type that originates from nearby electronics (mains, lights, etc.) and mechanical oscillations, become far detuned from the atoms. This works in the same manner as confining the atoms in an Ioffe-Pritchard type trap, but without the need to create elaborate wire geometries. With this in mind, the first assumption is that one would want to dress the atoms at a very high frequency, but here we are limited by the curvature of the static trapping potentials, as higher dressing frequencies couple to atoms when they are located further from the trap centre (at a higher static field value). This creates the issue that further from the trap centre, trap gradients are typically lower, meaning that atoms are less well confined, and as such have a lower phase space density. As a result, we choose to dress at 1 MHz, as it is well clear of most noise effects, that could lower atom numbers, but only causes a shell radius in the μm range, meaning trapping gradients do not significantly change. We are also limited by the magnitude of the dressing field somewhat, as the rotating wave approximation requires the the Rabi frequency of the dressing remains smaller than the dressing frequency. As such we dress with a Rabi frequency of a few hundred kHz, which does not significantly distort the trapping potentials. There is also some consideration for the so-called trap frequency, that is unrelated to our RF-dressing scheme, but instead measures the oscillation frequency of atoms about the trap bottom (assuming the trap is harmonic, which is the case for a quadrupole trap, and very nearly the case for ioffe, and RF-dressed traps). These frequencies fall into the 100's of Hz to 10's of kHz range typically, so are not driven by the RF fields, making them of little concern.

3.2.2 Spectrum of an RF Dressed trap

Proper characterisation of atoms trapped within RF Dressed potentials remains similar to those used for static trapping methods, with absorption imaging remaining a valid method of probing the atomic cloud. The main

tool of investigation, RF spectra, also remains a viable method, albeit with a few changes to our expected results. As a result of the mixing products between an RF probe, and the RF dressing field, we no longer expect to see a single spectral peak, instead we observe three separate peaks, each belonging to a separate polarisation component of the RF probe. The first peak, which corresponds to the $\hat{z}$ polarisation, is seen at the dressing Rabi frequency, which effectively acts as a trap bottom measurement. The second and third peaks, which correspond to the $\hat{\sigma}_+$ and $\hat{\sigma}_-$ polarisations, are seen at the RF dressing frequency, plus or minus the dressing Rabi frequency, respectively [28]. An experimental spectrum taken of atoms in an RF-dressed Ioffe trap is shown in figure 3.13

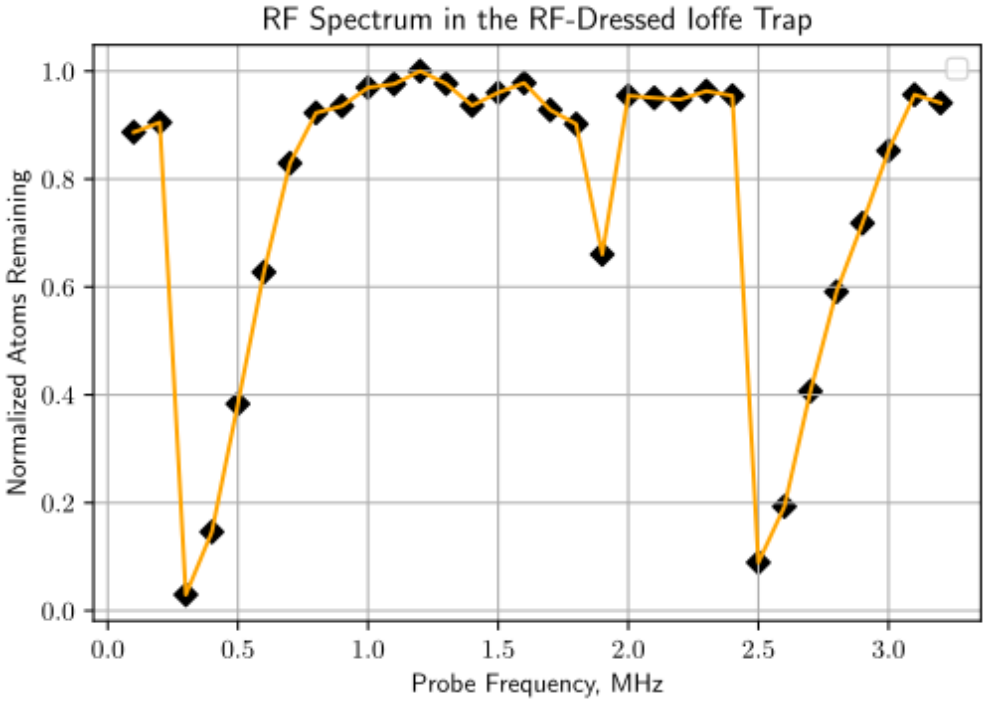

Figure 3.13: RF Spectrum of the RF-dressed Ioffe trap. We see three peaks, and can use them to measure the Rabi frequency at $\Omega_{RF} \approx 250\ kHz$ and the dressing frequency at $\omega_{RF} \approx 2.2$ MHz

3.3 State-Dependent Transport

This chapter, up until now, has only described preparatory techniques, which only serve to enable an interferometric sequence, but do not perform

it. In this final section, one of the main achievements, a novel method of driving atomic clouds around a ring, in a state-dependent, fully-trapped manner, will be presented.

The physics presented in this section relies on the interactions between many different polarisation and frequency components, of multiple different RF, and DC, magnetic fields. To aid in readability, whilst also reducing wordiness, a lookup table for the different components, their notation, and a brief description of function have been provided below.

Field component	Notation	Description
Ringtrap Quadrupole Field	B_{DC}	Static field that forms the base field geometry of the ringtrap
RF-Chip Field	B_{RFChip}	RF-Field used as the radial component of the smoke-ring dressing
RF-C4 Field	B_{RFC4}	RF-Field used as the vertical component of the smoke ring dressing
RFx Field	B_{RFx}	Planar RF-field used to interfere with the radial components of the smoke-ring dressing, to create state-dependent potentials

Table 3.1: Magnetic Fields used in the creation of state-dependent potentials in a ringtrap. All of the RF fields are linearly polarised along the direction indicated in the description.

Frequency	Notation	Description
RF Dressing Frequency	ω_{RF}	Base frequency of all dressing fields, set experimentally to 1 MHz
RF Rabi Frequency	Ω_{RF}	Rabi frequency induced by the RF dressing field at the point of lowest coupling strength
Trap Rotation Rate	Ω_T	Rate at which state-dependent traps are rotated around the ring. Equal to the difference between the Dressing frequency of the Smoke ring, and RFx dressing frequency

Table 3.2: Frequencies that are used in, and result from, the creation of state-dependent potentials in a ringtrap.

3.3.1 Creating an RF-Dressed Ringtrap

The state-dependent transport scheme relies on the difference in the the coupling of σ_+ and σ_- RF polarisations to the $F = 1$ and $F = 2$ hyperfine manifolds. To be able to exploit this we require an initial dressing geometry that satisfies two conditions: Firstly, all atoms in the ringtrap must remain dressed at all times, meaning that there must be some component of the RF-dressing field perpendicular to the static ringtrap quadrupole field at all points. Secondly, all atoms should experience the same static magnetic field direction, meaning that they should be confined to a single strip around the ringtrap corresponding to a single poloidal angle. This is achieved through the introduction of an RF-field that is polarised elliptically with respect to the ringtrap cross-section. This RF field has a vertical component B_{RFz} and a radial component B_{RFr}. For a dressing field where $B_{RFz} > B_{RFr}$ atoms located at the top of the ringtrap (which experience a vertical static magnetic field and thus only couple to B_{RFr}) experience a smaller potential shift from the RF than atoms located at the sides (which experience a horizontal static magnetic field and thus only couple to B_{RFz}). This creates a trapping geometry in which atoms are confined top and bottom of a hollow toroidal shell. Atoms in this trap all experience the same vertical static magnetic field, and experience a trap bottom potential of $h\Omega_{RFr}$ -

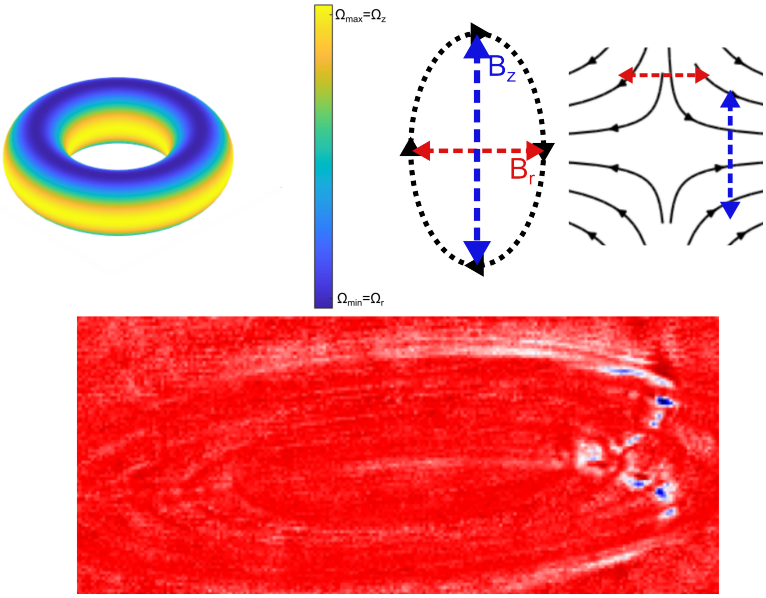

Figure 3.14: Illustration of Trapping potentials in the RF-dressed ringtrap, and absorption imaging of atoms loaded into the dressed ringtrap

the rabi frequency induced by the radial component of the RF field. Due to this geometry created, we nominally refer to this trap, and the dressing field that creates it, as the smoke ring, and smoke ring field, respectively. Figure 3.14 shows the field polarisations, and a map of the potentials across the torus surface, along with an absorption image of atoms loaded into this trap.

Creating this trap experimentally begins with atoms cooled to around $1\mu K$ in the Z-type Ioffe trap. The smoke ring dressing field is created through the use of two coils of different width underneath the ringtrap, namely the RF-Chip coil, and the C5 coil on the atom chip (descriptions of these coils are given in Chapter 4), where we use the RF chip coil to produce the vertical component of the field, and the C5 coil to produce the horizontal field component. This field is initially some 500 kHz red-detuned from the trap bottom in the ioffe trap, and then the frequency is ramped up to 1 MHz to dress the atoms. Whilst doing this causes a very slight amount of non-adiabaticity in the introduction of the dressing, it is preferable, as starting from a higher detuning causes the second harmonic of the RF field to ramp through the atoms, expelling them all from the trap. With the dressing field applied, the bias field that forms the Ioffe trap is lowered, and

the atoms move into the dressed ringtrap. Despite traps forming on the top and bottom of the torus, we only see atoms on the top, which is likely due to two reasons: Firstly, the Ioffe trap formed is slightly higher than the ringtrap, meaning that the natural path of atoms tends towards the top trap. Secondly, the bottom trap is located closer to the conductive chip surface, meaning that noise effects (induced currents, etc.) cause atoms in that trap to have a shorter lifetime. The trap minima in this scheme is set by the Rabi frequency at the top of the ring, which is determined by the magnitude of the radial component of the smoke-ring dressing field. It is desirable to have this trap minima as high as possible for later stages of the experiment, but we are limited by the fact that the RF-Chip, which we describe as producing a radial field, actually produces a field that points at 17° to the vertical, meaning that it contributes only around 30% of its total field magnitude to the radial dressing component. This limits the trap floor to 200 kHz at maximum power, as more amplification would make the dressing field too noisy. The depth of this trap is determined by the difference in Rabi frequencies of the top and sides of the ring, as the vertical component of the dressing field is responsible for the Rabi frequency on the side, and thus trap depth. A diagram showing the geometric origin of this limitation can be seen in Figure 3.15.

3.3.2 State-Dependent Potentials

With atoms confined to a single ring-shaped plane, the next step in reaching the interferometer geometry is to be able to localise atoms in a state-dependent manner. The symmetry breaking derives from the polarisation dependent coupling strength of the RF-dressing field. Recall from Equation 2.46 that the coupling strength of the RF is dependent on $B_{\pm}$, which is the component of the RF field in the direction of the local larmor precession. By breaking the geometric symmetry of the RF-field polarisation we can create a state-dependence for the potentials. In other words, control of local RF-polarisations around the ring allow for the creation of local-state-dependent polarisation around the ring, allowing us to trap atoms, that have different internal hyperfine states, in different locations around the ring.

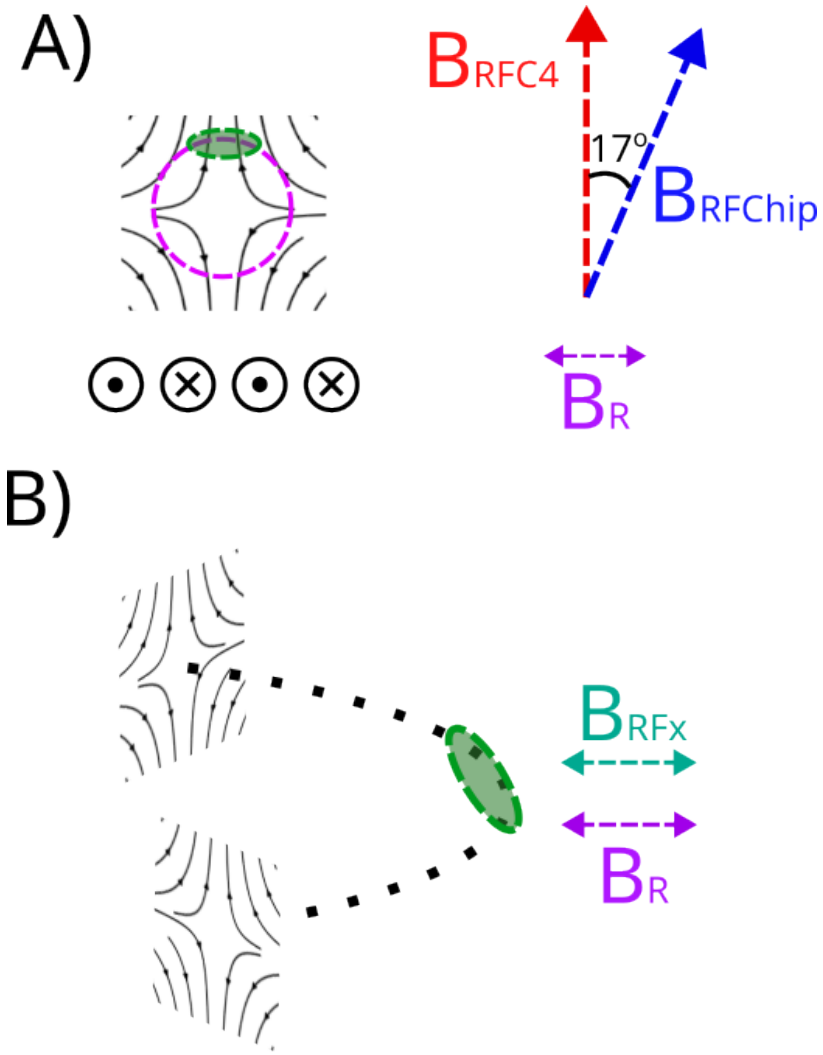

Figure 3.15: Diagram detailing the geometry of the dressed ringtrap, and its limitations. A: The left shows a slice through the ringtrap, the pink circle is the resonant shell, and the green oval shows where the atoms sit. The right shows the angle between the two dressing fields B_{RFC4}, and B_{RFChip}, and how the shallow angle of 17^o between them leads to a small resultant radial dressing field, which limits the coupling strength of the dressing. B: Geometry of the ringtrap after localisation, the interference of B_{RFx}, and B_R leads to a potential minima where the green oval is located, but the maxima at the same point is limited by the magnitude of B_R.

To understand how this polarisation symmetry break is formed, and how it gives rise to local potential maxima. We consider that there are two phase components present when discussing the smoke-ring dressing field, the first is the temporal phase, φ, which is the phase resultant from the evolution of the RF field over time. The second phase is the Geometric phase, that results from the symmetry of the dressing field radially, as the field direction in the lab frames turns with the toroidal angle, θ_T, of the ringtrap in that the field points in opposite directions at opposite times (or has a phase difference of π radians). Whilst not technically a phase in the traditional sense, it is useful to discuss as one when we introduce the planar field B_{RFx}. This field interferes with the smoke-ring field differently, depending on the local geometric phase of the smoke-ring field. When the planar field and some-ring field point along the same axis, the resulting interference field can only be linearly polarised, with a magnitude depending on the difference in temporal phase between the two fields. Importantly, when the side of the ring at $\theta_T = 0$ is maximally constructively interfering, the opposite side of the ring at $\theta_T = \pi$ will be maximally destructively interfering. At the sides of the ring, where $\theta_T = 0$ or $\frac{3\pi}{2}$, the field polarisation resulting from interference is not necessarily linear, but instead, depending on the temporal phase difference, can be circularly polarised, in either the σ_+, or σ_- directions. When one side of the ring is producing a σ_+ polarisation, the π radian shift in θ_T on the other side of the ring results in a σ_- polarisation. A diagram showing the differing interference results for different θ_T, and φ values is shown in Figure 3.3.2

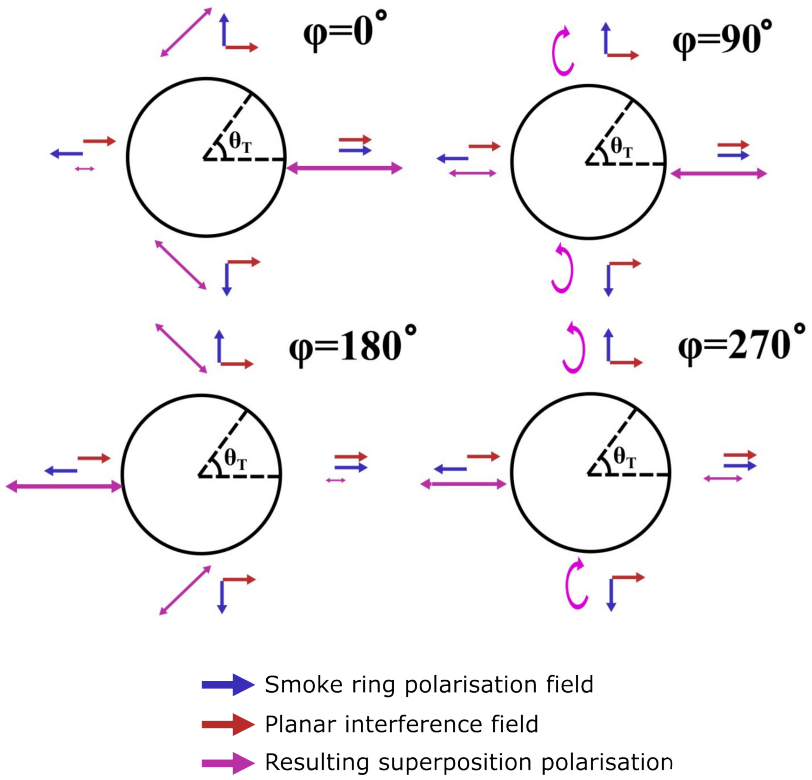

Figure 3.16: Diagram showing the dressing fields that result from the interference between the smoke ring field, and the planar field, for different temporal phase differences.

Thus, depending on the temporal phase difference between the planar field, it is possible to create a situation where the coupling strength is at a minimum for both the $F = 1$, and $F = 2$ states, and then by evolving the temporal phase difference move into a situation where the coupling strength minima are in two different locations around the ring for the two different hyperfine states. The potential landscape for these state-dependent traps can be seen in figure 3.17

3.3.3 State-Dependent Transport

Rather than viewing the state-dependent potentials as simply a consequence of the interference of the planar and smoke-ring fields, we can instead view it as two different polarisations of the dressing field propagating around the ring as φ_T evolves. This can be exploited to create a transport scheme, where by evolving φ_T, we can move the two trapping potentials

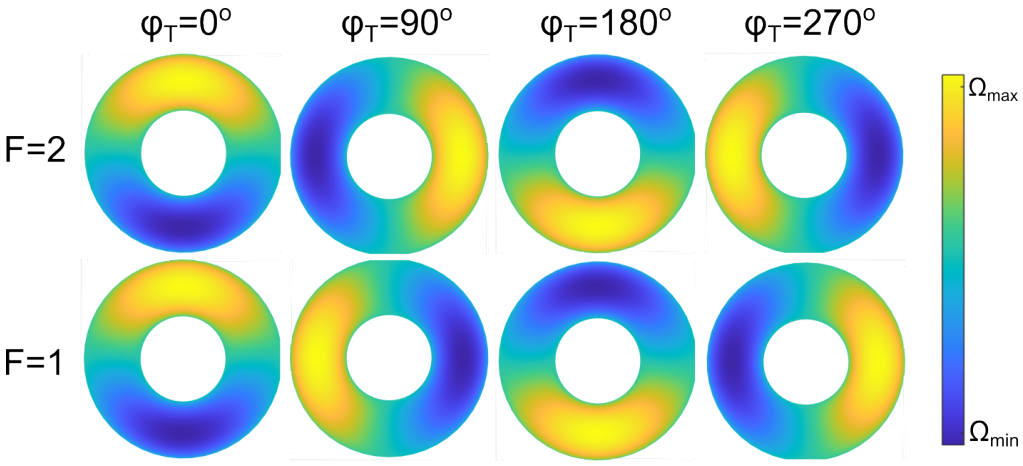

Figure 3.17: Illustration of state-dependent potentials evolving with phase. As the phase φ_T is evolved, the potential minima for the two different hyperfine manifolds move in opposite directions around the ring

opposite directions around the ring. Experimentally, this is achieved by slightly increasing the field dressing frequency of the planar field by an amount Ω_T. This has the effect of causing φ_T to evolve at at a rate determined by Ω_T (i.e. if Ω_T is 1 Hz then φ_T will evolve from 0 to 2π once every second). This causes the traps to rotate about the ring at this frequency, and sets the interrogation time for the interferometer (2Hz rotation speed means the traps complete a full loop in 500 ms). We observe, in Figure 3.18, that setting the rotation frequency to 5Hz causes atoms to move around the ringtrap, completing one full loop. More importantly, for the same change in rotation frequency, atoms in the two different hyperfine states, $|1,-1\rangle$ and $|2,1\rangle$, travel around the ring in opposite directions, meaning we have achieved state dependent transport. We are limited in the speed of this transport by the non-adiabaticity of the trap movement. Essentially, the traps formed by the interference are shallow enough that the energy imparted by their sudden movement is enough for atoms to overcome the potential barrier, and simply not move about the ring. There are two possible solutions to this issue, one is gradually ramping the planar dressing fields, such that the traps 'accelerate' around the ring, this would solve for some of the non-adiabatic components, but slows down the actual rotation (as accelerating from 0Hz to 5Hz in a full sequence is the same as travelling at a constant 2.5Hz for that entire sequence). As discussed in Chapter 5,

we are limited by coherence time, so slowing down the rotation rate is not preferable. The other option would be to increase trap depth, but this is hard-limited by the geometry of coils used to generate the smoke-ring dressing field.

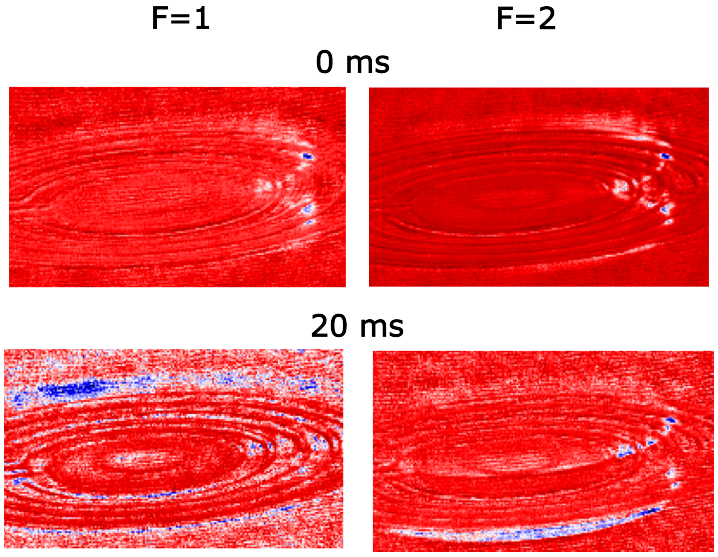

Figure 3.18: Absorption Imaging for atoms in both the $F = 1$ and $F = 2$ being driven around the ringtrap via RF dressed potentials at a rate of 2 Hz. Due to lack of atoms in the trap, and how thin the cloud spread absorption imaging is poor here, but the blue clouds of atoms can clearly be seen travelling clockwise for the $F = 2$ manifold, and anti-clockwise for the $F = 1$ manifold.

Chapter 4

Experimental apparatus

The previous chapter delved into the methods of controlling and manipulating atoms, all in the aim of creating the RF-dressed, fully-trapped, atomic sagnac interferometer. But all of those techniques are of little use without the proper equipment to realise them. Experimental cold atom setups suffer from noise issues, stray fields, and a host of other issues that impede the ability to manipulate atoms effectively. This chapter will provide a detailed overview of the experimental setup used to realise the RF-dressed transport, and microwave based manipulation in later chapters. The experimental apparatus, and thus this chapter, are split into four parts. The first is the vacuum chamber superstructure and the surrounding components. The second is the Atom Chip stack, a cutting edge conductive structure that incorporates micrometer scale electronics to create tight and stable magnetic potentials. The third is the optical setup, responsible for all laser light used in the experiment. The final is the generation of AC signals, which is used to generate clean AC magnetic fields in both the RF and microwave range.

All of the constituent parts that make up the experimental apparatus are connected, and controlled through the use of a network system that runs on National Instruments Labview software. The program runs on a PXI system connected to an internal network, and is accesible through PC desktop in the control room. The PXI converts the Labview script into commands for an FPGA board, which then executes the script, producing analogue and digital outputs. Analogue outputs range from -10 to 10 volts

and are used for controlling other components in the setup (current supply output, AOM frequencies, Voltage controlled attenuators, etc). The digital outputs act as Transistor-Transistor Logic (TTL) signals, used for turning on and off components in the setup.

4.1 Vacuum Chamber and Surrounding Superstructure

At the heart of the experiment is the vacuum chamber, an enclosed space with an internal background gas pressure of $p < 10^{-10}$ mbar. The vacuum chamber is fundamentally necessary for the experiment due to the negative effect that collisions with room temperature air molecules, namely heating of the atoms, and nonadiabatic spin flips, leading to losses. The vacuum is kept at this low pressure via an always-on ion pump. The vacuum chamber serves as the initial building block for which the rest of the experiment is built on, it and its surrounding superstructure contain coils for DC field generation, view ports to allow both laser input and optical output from the chamber, and precision connector inputs that connect external AC current sources to antennae inside the chamber. Diagrams illustrating a simplified layout of the vacuum chamber can be seen in Figures 4.1 and 4.2, which show views from the side and top, respectively.

4.1.1 DC field coils

Flanking the vacuum chamber on all sides are three pairs of conductive coils. Each pair of coils is positioned along a Cartesian axis perpendicular to the others, and as such are named the x, y, and z coils. Due to the high inductances and resitivities these coils have (due to their large sizes and high number of turns), the current sent to them first passes through a relay controlled via TTL signal. This allows for fast switching of the coil currents, as a lingering current within the coil could have adverse effects for stages of the experimental sequence not requiring the use of the external coils.

Z coils

The z coils are an anti-Helmholtz pair designed to produce a large quadrupole trap mainly for the purpose of initial MOT trapping, each coil containing 120 (12×10) turns. The two coils are connected to separate current sources, allowing for dynamic -positioning of the quadrupole centre by changing an offset current between the two coils. The large amount of turns these coils have, and large currents being driven through them creates the need for cooling mechanisms. To achieve this each of the two z-coils is sandwiched between two water cooled metal plates. Temperature stability of these coils is particularly important, as the high inductance of the coils mean that small changes in resistivity can cause large changes in the turn on or turn off time of the coils, reducing the consistency of the experiment over longer timescales.

X and Y Bias Coils

The X and Y coils are both set up in Helmholtz arrangements such that they produce static bias fields in the x and y directions, respectively. Each pair of coils is driven by a single power supply that can provide both positive and negative currents, allowing for full bias control in the X-Y plane.

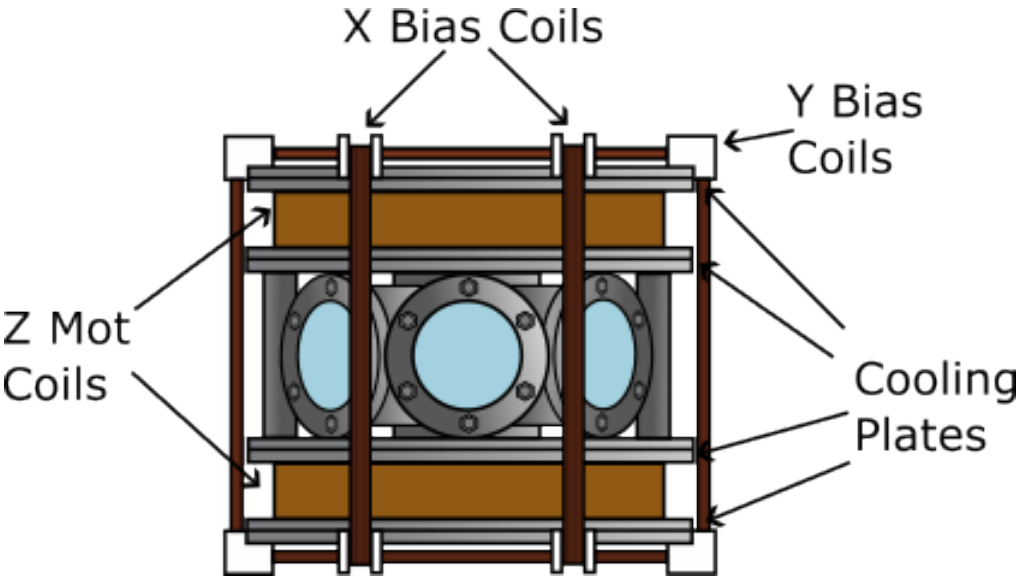

Figure 4.1: Schematic Diagram of the Vacuum chamber from the side. Optical components and the PCB hat stripped away for better viewing of the external coils.

4.1.2 On Chamber Optics

In addition to magnetic fields, the MOT stages also require optical fields in the chamber. These optical fields are generated on an optical bench, that will be discussed in a later section, but are sent via optical fibre to optical rigging attached to the chamber. The laser beams that form the basis of the 3D MOT are coupled into three optical axes, labelled X-MOT, Y-MOT, and Z-MOT (the X and Y MOT axes are 45 degrees offset from the X and Y magnetic field axes). The X and Y beams pass through the chamber and are retro-reflected by mirrors back along their path, and the Z beam enters from underneath the chamber, and is retro reflected off the gold conductive surfaces of the atom chips.

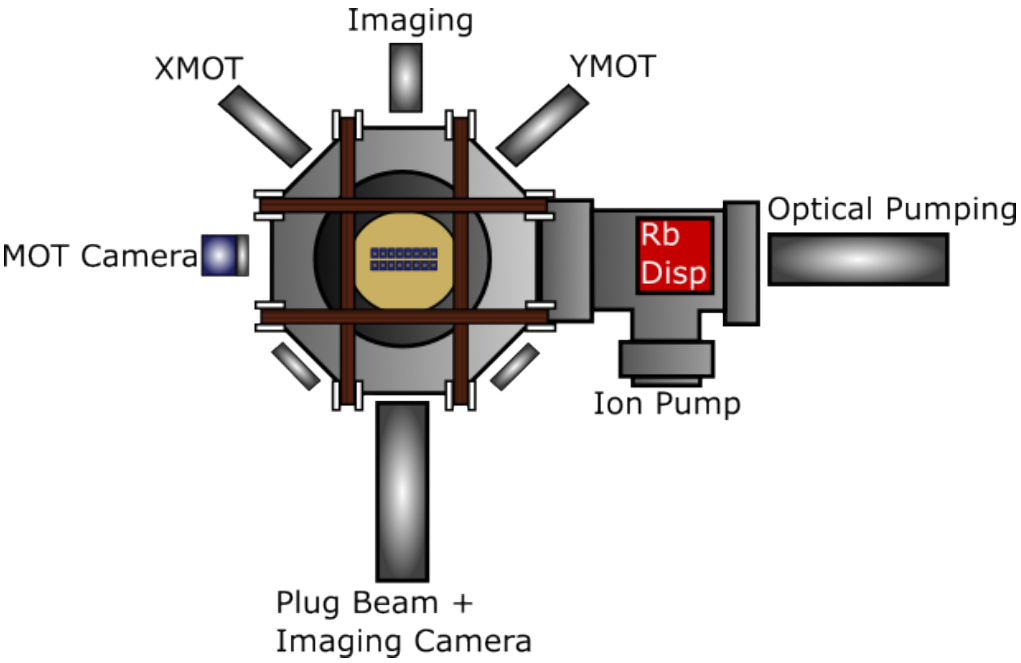

Figure 4.2: Schematic Diagram of a top-down view of the vacuum chamber. Optical components are enclosed in black tubes. Not shown is the Z-MOT axis, which is underneath the chamber.

4.1.3 Rotation Table

The vacuum chamber sits on a motorised spinning platform intended to simulate rotation effects on the vacuum chamber to allow for testing of the interferometer. The rotation table is driven by an electrical motor connected via USB to the laboratory computer, which can remotely set a rotation command during an experimental sequence. The table and thus the entire chamber sit on an air bearing to allow for smooth rotation of the table, having the added effect of filtering out high-frequency vibrational noise from the vacuum chamber.

4.2 The Atom Chip Stack

The magnetic fields required to produce the ringtrap, and the quadrupole traps tight enough to load it, are all produced on an atom chip stack that is suspended upside down from the top flange of the vacuum chamber. The stack consists of 3 specially produced micrometre-scale electronics: The

Atom Chip, the EM Ring Chip, and the RF Chip. The Atom chip was produced by an external PCB manufacturer and the EM and RF chips were produced at Ben Gurion University. The chips are stacked on-top of one another, connected via ultra-high vacuum compatible glue. The Chip stack was then connected to the top flange of the vacuum chamber, and connections were wire-bonded onto pads that connect to the conductive elements of the chips. These wires connect to a PCB hat that sits on the external side of the vacuum flange, shown in Figure 4.2 as the pale disc between the bias coils. This PCB hat allows external current sources to be connected directly to the chips via screw plug terminals, these terminals also allow for monitoring of the voltages and resistances of the coils via the Electronic watchdog unit.

4.2.1 The Atom Chip PCB

The bottom layer of the chip stack, and the largest of the chips is the atom chip, a multi-layer PCB. It consists of 7 multilayered concentric coils, labelled C7 through to C1 in order of descending size. The coils are gold, and layered in ultra-high vacuum compatible PCB substrate. The gold conductive layers forming the concentric coils can be seen in the photograph of the PCB in Figure 4.3.The primary purpose of this chip is to provide the magnetic fields required to transfer atoms from a quadrupole generated via external coils. This is done by creating a quadrupole with the outer coils, and gradually switching to the innermost coils. To do this coils must be configured in an anti-Helmholtz manner, and as the current sources that drives them are not bi-directional, must have their polarity manually set, by reversing the wire layout on the PCB hat. The C4 coil is connected to both a DC current source, and the RF current source through a home-made Bias-Tee network. This allows the coil to produce both a DC field for atom trapping, and an RF field for dressing and cooling, simultaneously.

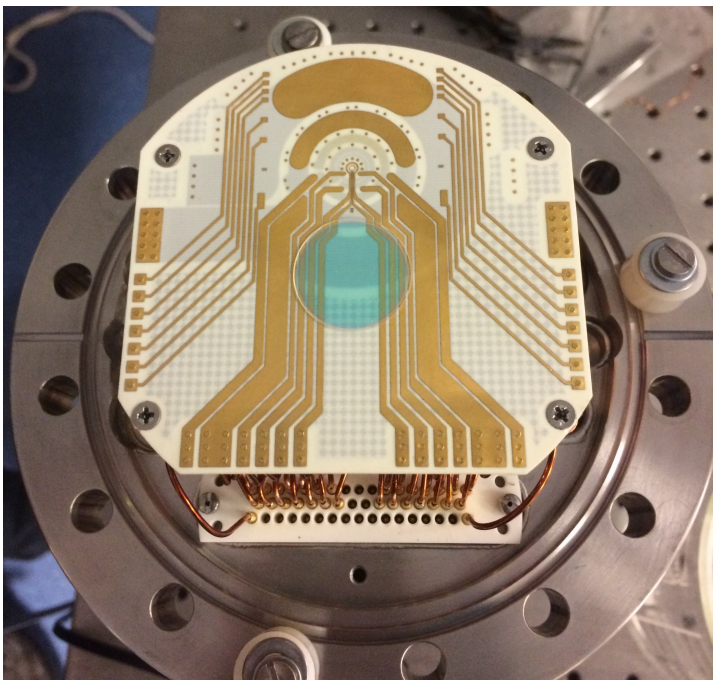

Figure 4.3: Photograph of the atom chip PCB, without other chips attached, mounted on the vacuum flange. The turquoise disc in the centre is a wave-plate for the purpose of retro-reflecting the Z-MOT beam

4.2.2 The EM Ring Chip

The top chip of the stack is responsible for generating the quadrupole ringtrap field. The chip consists of two gold layers evaporated onto a UHV-compatible silicon substrate. These gold conductive layers are in such a shape as to produce a quadrupole ringtrap when DC current is passed through them, the rings are rotated 180 degrees with respect to one another to allow for swapping between the two coils to avoid the discontinuity in the ringtrap caused by the lead wires. Due to the $2\mu m$ silicon layer that separates the two coils, the lower one is slightly larger in radius such that the two quadrupole ringtraps match better in terms of position and gradient where we want to be trapping atoms. The four wires forming the EM chips current carrying structure can be seen in Figure 4.4.

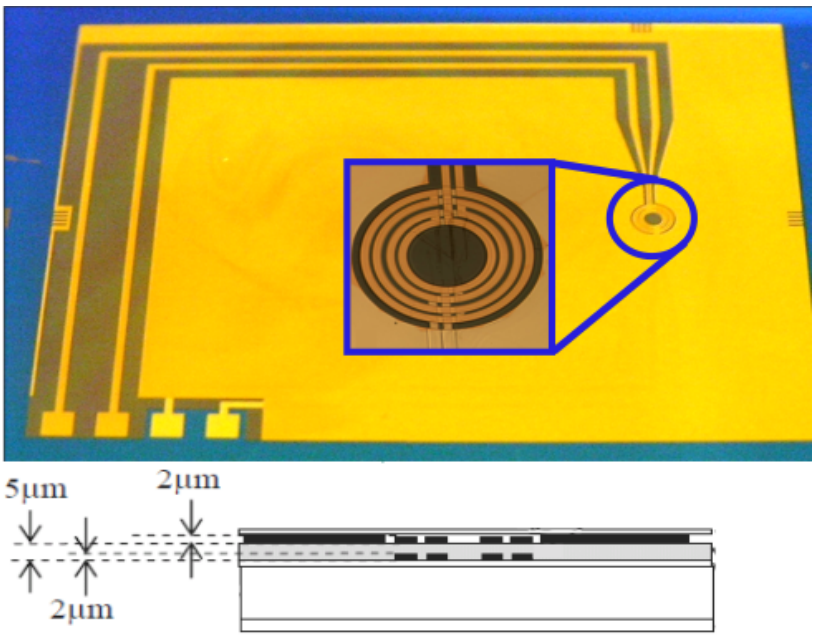

Figure 4.4: Above : Photograph of the EM-Chip, with enhanced close up of the coils. Below : Schematic cut-through of the EM-Chip

4.2.3 The RF Chip

Between the EM and Atom chips is the RF-Chip, a silicon chip designed to produce a the radial component of the ringtrap dressing field. The chip features a two-layer coil, with layers on either side of a 280 μm silicon substrate, and connected through a copper via wire. Each layer is formed of ten tightly would, $40\mu m \times 40\mu m$ copper coils, formed through etching of the silicon, then copper electroplating. Figure 4.5 shows the RF chip placed on top of the Atom chip PCB, and its tightly wound coil. The Chip is connected to an external matching network, that includes a step down transformer to maximise current through the coil, and impedance matching elements to such that the coil has an impedance of 50Ω at 1 MHz

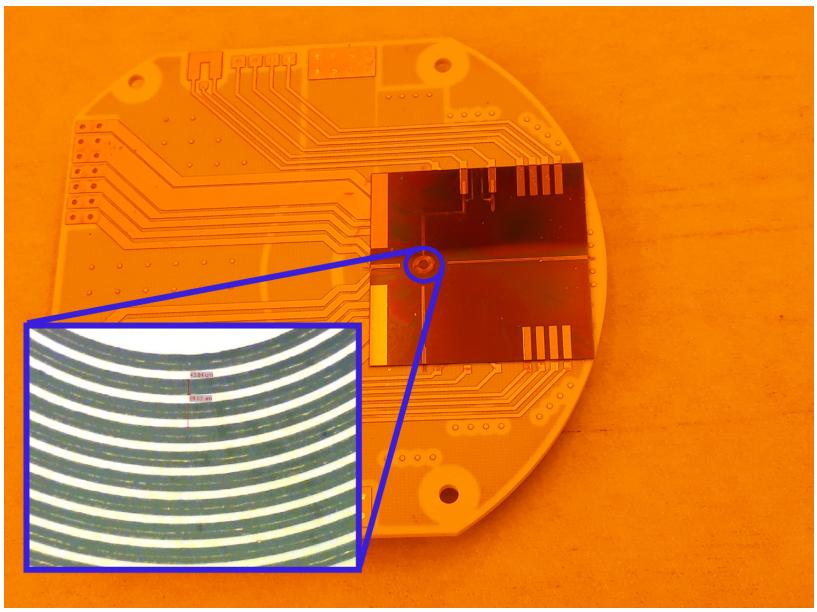

Figure 4.5: Photograph of the RF Chip mounted atop the PCB, with an enhanced close up of the RF coil tracks.

4.2.4 In-Chamber Antennae

Attached to the atom chip stack are free-standing, UHV compatible, Kapton-clad copper antennae. Standing perpendicular to the chip are two RF coils, named RFx and RFy, whose purpose is to produce high-magnitude, planar RF fields along their respective axis. However, RFx is not along the x-axis, but instead at 45 degrees between the x- and y-axes, as otherwise the coil would obstruct absorption imaging of atoms close to the chip. Photographs of these antennae individually, and their positions with respect to the atom chip are shown in Figure 4.6. These two coils contain 5 turns each and are pressed as close to the chip as they can to maximise field values. Also attached to the vacuum flange that the PCB sits upon is an antenna designed to produce microwave-frequency magnetic fields for the purposes of driving atoms between the $F = 1$ and $F = 2$ manifolds. This antennae is designed such that it is resonant at 6.835 GHz - the hyperfine splitting energy for the hyperfine transition.

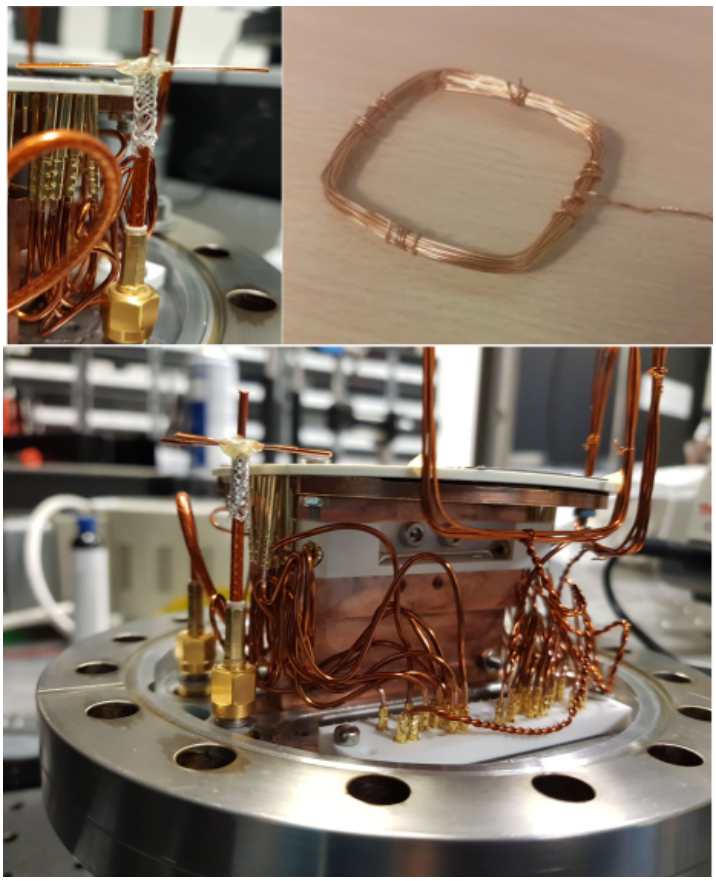

Figure 4.6: Photographs of the In-Chamber AC antennae. Top left: The MW Antennae. Top Right : A dummy version of an RF coil. Bottom: The MW antennae, and two RF coils mounted on the vacuum ceiling flange, next to the Atom chip PCB

4.3 Optical Setup

The experiment has five different requirements from optical fields, and makes use of lasers for all of these, the five required optical fields and their uses are listen below:

Cooling Provides the velocity dependent force required for the Doppler cooling of atoms and forming the optical molasses.

Repumping Repopulates the MOT by driving atoms that fall into the $F = 1$ state back into states addressable by the cooler laser.

Optical Pumping Drives atoms into the trappable $|2,2\rangle$ state after the MOT

Imaging Tuned such that atoms in the trappable $|2,2\rangle$ state are opaque to it, providing absorption imaging.

Optical Plugging High power beam providing a repulsive force at the centre of a quadrupole trap, effectively 'plugging' the field zero.

These five requirements necessitate the use of multiple lasers, each with a stable frequency located around an atomic transition. This requires the use of many optical techniques to tightly control the frequency, power, stability and polarisations of lasers involved. This section will provide a detailed summary of the lasers used, and the techniques applied to achieve the requirements.

4.3.1 The Table Lasers

The first four requirements are all performed by a set of lasers, called the table lasers, for their collective location on an optical bench in the laboratory. These lasers share the need for fine control of their frequency, whilst having a relatively low power requirement. As a result, these beams are all produced by cavity-diode lasers. The cooling and repumper beams are produced by a Toptica TA-Pro, the optical pumping is produced by a Toptica DL-Pro, and the imaging beam is produced by a Diode cavity laser custom produced at the University of Birmingham. These lasers are used for their high stabilities, in both power and frequency domains, all whilst being able to maintain clean, single-mode beams. A schematic of the beam paths, with the components used to manipulate the laser light, is shown in Figure 4.8.

Frequency Locking

The laser sources are frequency locked to transitions on the D2 line (The transition between the $5^2\mathcal{S}_{\frac{1}{2}}$ and $5^2\mathcal{P}_{\frac{3}{2}}$ levels) via a Pound-Drever-Hall locking scheme. selection is shown in Figure 4.7.

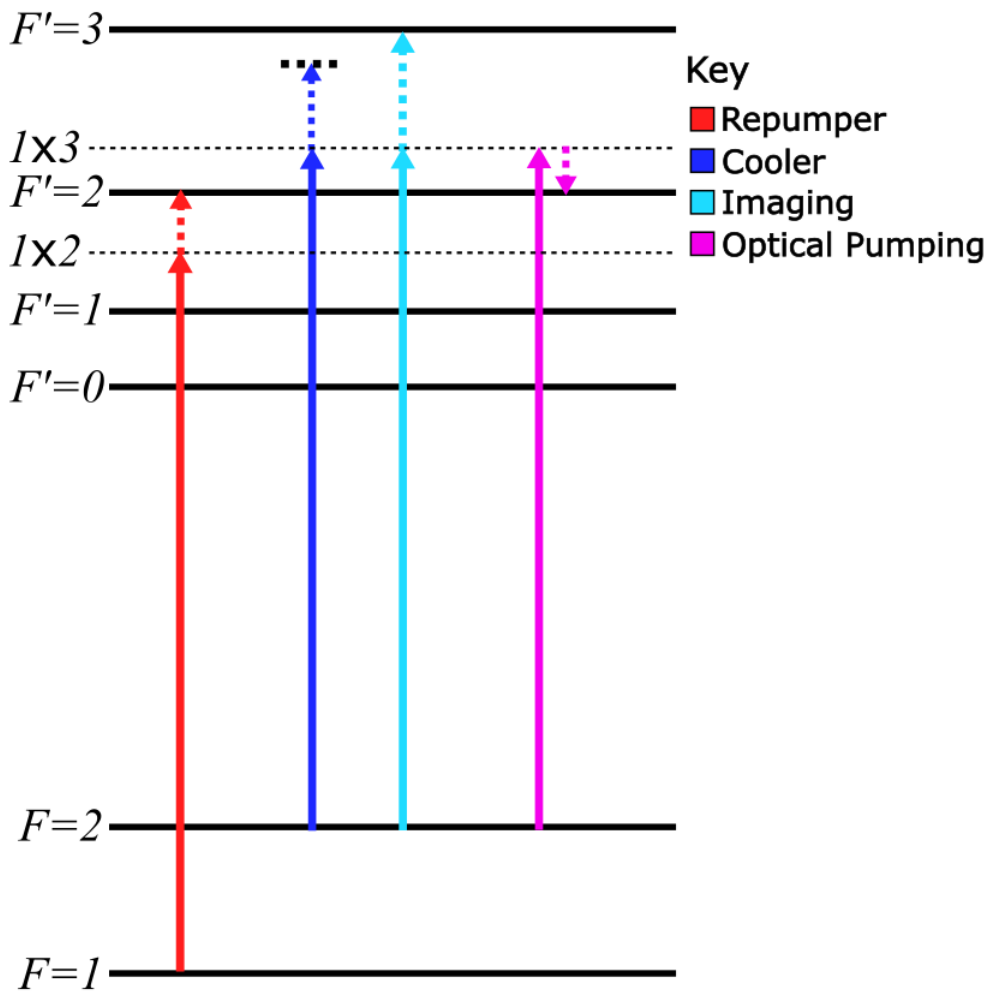

Figure 4.7: Diagram showing the transitions that lasers are locked to, solid lines indicate frequencies locked to specific spectral features, whereas dotted lines represent shifts induced via AOM.

The locking scheme uses Doppler-free saturated absorption spectroscopy [71] referenced through ^{87}Rb vapor cell. The beam is passed through the cell twice (with the first pass through being labelled the pump beam, and the second the probe beam) to eliminate linewidth broadening that occurs due to the thermal motion of atoms (hence, Doppler free). In order to see the absorption spectra incident on a photodetector, we must modulate the beam such that the frequency is scanned over time, we do this by applying some fast time-dependent modulation, usually by applying a high frequency sine modulation to the current supplying the diode laser, and then applying a slow time-dependent modulation, usually either modulating the voltage

of the piezoelectric crystal that controls the grating angle inside the diode laser, or by using a solenoid wrapped around the Rubidium cell to induce Zeeman shifts, causing a detuning from the transition). We then use electronics to create the time-derivative of this signal, which allows us to lock the frequency to transition peaks via PID-locking electronics.

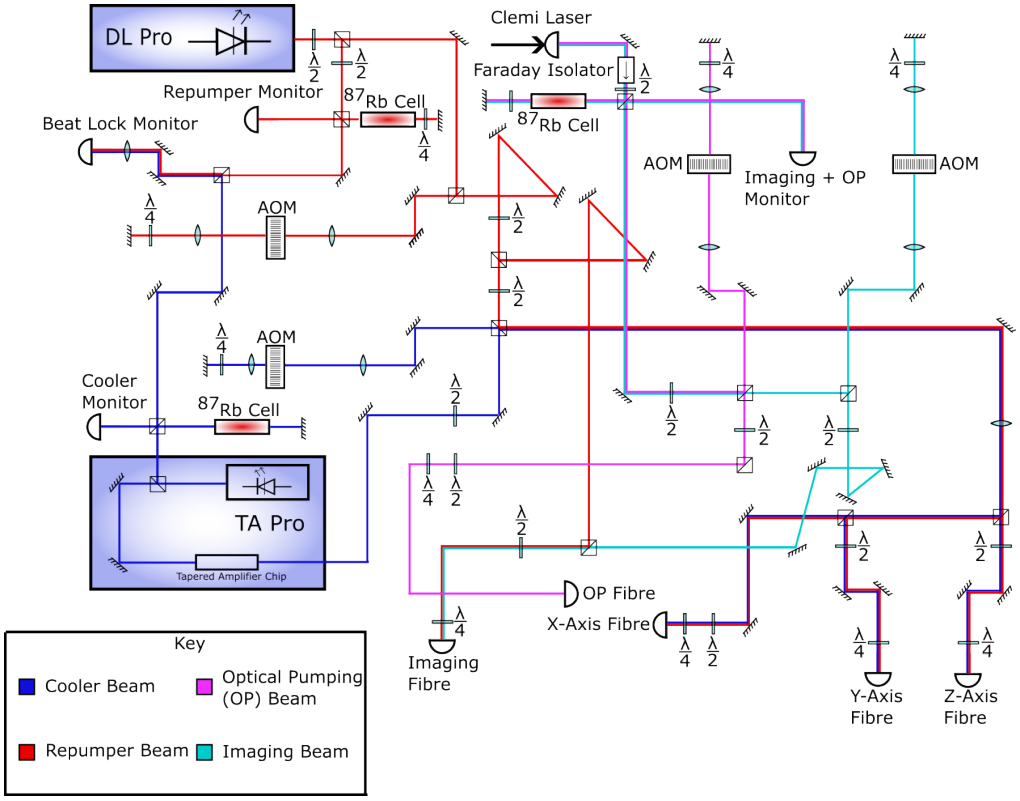

Figure 4.8: Schematic Diagram of the Table Laser Setup

Acousto-Optical Modulators

The frequency of the beams can be fine tuned via the use of Acousto-Optical modulators [68]. These active optical components use an electronic RF signal to drive Phonons of the same frequency through a crystal inside the AOM. The propagation of the phonons through the crystal creates an artificial period structure, through which light can diffract via Bragg diffraction. Laser light entering the crystal at a slight incidence angle will absorb a phonon, and be deflected by an angle θ, having its frequency shifted by an amount equal to the RF electronic signals frequency. The resultant beam is split into multiple beams, each having been deflected by

an angle equal to an integer amount of θ. These deflected modes have their frequencies shifted by an amount equal to the integer deflection number, times the RF frequency. This process is shown in Figure 4.9. The angle of incidence can be tuned to maximise the laser power in the mode with the desired frequency shift. The AOMs used in this experiment have a maximum single pass efficiency of 80%, meaning that we expect to see a maximum efficiency of 64% for the double pass. The AOMs are especially powerful tool as they convert and electronic RF signal, which is dynamically tunable in frequency (via a VCA input signal) into a dynamic and tunable shift in laser frequency. Care does have to be taken however, as a shift in RF frequency also slightly changes the Bragg angle, θ, slightly changing the beam path, and thus the coupling of optical components in the rest of the optical table. This path deflection is not purely a negative, however, as it can be used as a fast-acting shutter, by suddenly changing the RF frequency by a large amount, the beam path can be misplaced, meaning that it wont couple into the fibre and reach the atoms. A switch done this way acts on the timescale of microseconds, rather than the milliseconds a traditional, mechanical shutter takes to close and open.

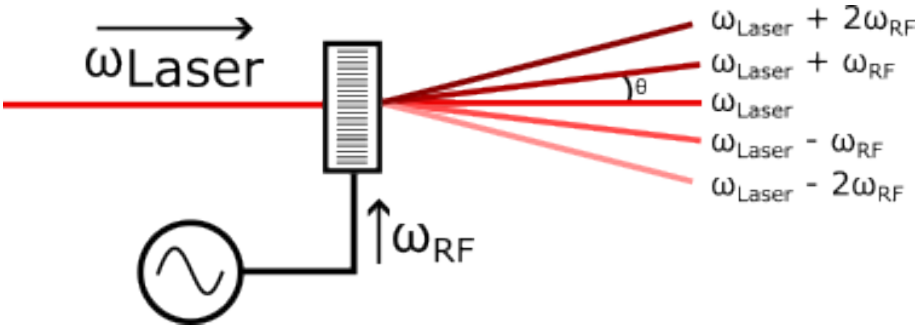

Figure 4.9: Schematic Diagram, showing the operation of an AOM device. Incident laser light with frequency ω_{Laser} is incident to the AOM device, which is modulated by an electronic signal of frequency ω_{RF}. The laser light is deflected into modes, at angles n θ with a frequency shift of n ω_{RF}

Polarisation control and Fibres

Both the MOT stage, and Optical Pumping require circularly polarised light fields, meaning special apparatus has to be used to generate the correct polarisation of beam. This is achieved through the use of both optical

table and chamber mounted waveplates. A $\frac{\lambda}{2}$ and $\frac{\lambda}{4}$ waveplates in the correct relative orientation can be used to create a linear polarisation, which is coupled into a polarisation maintaining fibre. The beam then passes through two more waveplates in the same configuration at a different angle, to create a circularly polarised beam. The power provided through the MOT beams drifts over long timespans, but is optimised to around 70 mW in the X and Y beams, and 90 in the Z beam. The imaging and optical pumping beams are significantly lower in power output, and each transmits only a few milliwatts of power into the vacuum chamber.

4.3.2 The Optical Plug Laser

The optical field used to produce the optical plug is subject to vastly different requirements than the other optical fields. The optical plug trap is far less dependent on precise frequency control than the other optical processes. Instead, we desire the maximum power possible. To achieve this we use a multiple device setup that utilises a Lighthouse Photonics pump laser, that outputs 10 W of 532 nm laser power. This laser has its frequency halved via a Solstis Titanium Sapphire laser, which produces $\approx 3W$ of 760 nm of laser power. This is then coupled via fibre into the vacuum chamber, where we see $\approx$ 1.7 W of laser power reach the atomic cloud.

4.4 AC Signal Generation

Crucial to the experiment in both obtaining state-dependent transport and state manipulation via microwaves, is the ability to produce highly controllable AC electronic signals. Signals generated must be controllable to high precision in both frequency and power. The sensitivity of atoms to these AC fields also presents a challenge, as sources of noise from the environment, or from current sources themselves. There are two frequency ranges on which this experiment operates, the RF frequency, which ranges from 0-100 MHz, and the microwave range, which operates at 6.83468 GHz $\pm$ 10 MHz

4.4.1 Generation of RF signals

RF signals are initially generated via a Direct Digital Synthesis (DDS) board, connected to the laboratory control FPGA. The board has eight RF output channels that can output low-noise, low linewidth RF current at a power of 7 dBm (5 mW), and has an unclipped frequency range of. The frequency is referenced to an internal crystal oscillating clock on the DDS board, which itself is synced to an external satellite-based GPS clock. The connection from the DDS to the FPGA, and thus the PXI system allows for dynamic control of RF signals during experimental runs, including frequency ramping, and dynamic phase control.

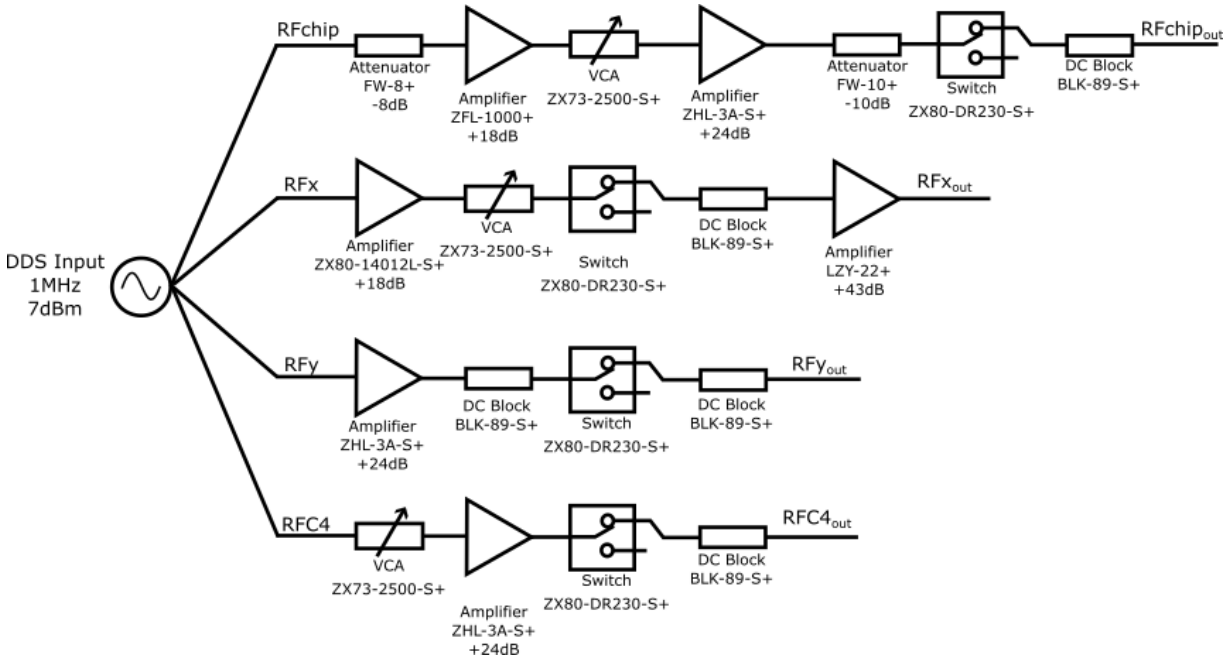

Figure 4.10: Schematic Diagram of the RF pre-amplification network.

The SMA output connectors are protected with passive DC blocking components to protect against power surging due to the internal DC resistance of the RF outputs being zero.

Power Amplification

The RF generation of the DDS board may have high stability and low noise, but the power output is inefficient for use in RF probing, dressing

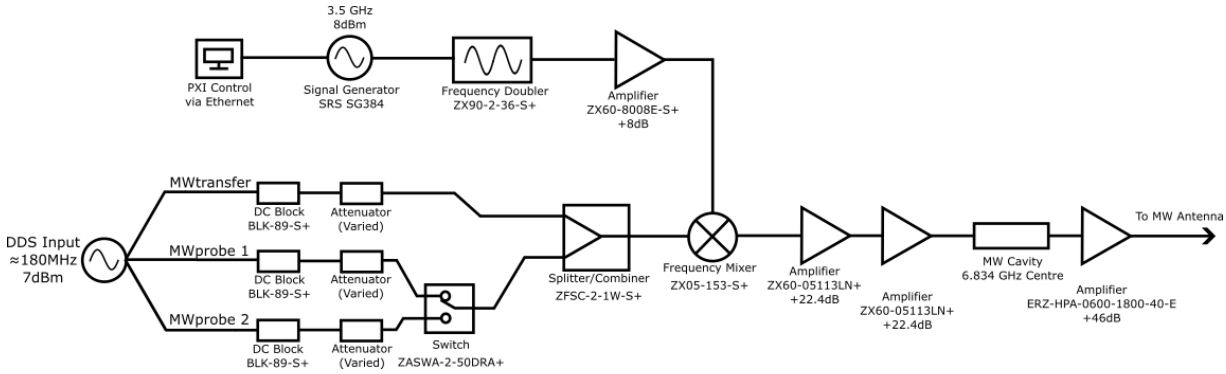

Figure 4.11: Schematic Diagram of the Microwave frequency generation, and amplification network

or evaporative cooling, and as such must be amplified through the use of active circuits.

Figure 4.10 shows the exact setup of the RF amplification circuits. Due to the addition of Voltage controlled attenuators, which allow for a reduction of power that scales with a VCA input (directly and dynamically controlled through the Labview interface) the RF amplification lives by the mantra : 'More power, more better'. In this, we mean that as long as the signal integrity remains high and the carried noise remains low, there is no upper limit to the power amplification that we desire.

4.4.2 Generation of Microwave signals

Microwave-frequency signals are more difficult to cleanly generate electronically and therefore are not able to be produced on the DDS board. Instead, we make use of an SRS signal generator. The signal generator is set to output a signal of 7 GHz at its maximum output power of 8 dBm, this signal is then mixed with one of three different RF channels, chosen by a switch. The mixing of microwave and RF signals produces two sideband frequencies, 7 GHz$-\omega_{RF}$ and 7 GHz$+\omega_{RF}$, referred to as the red and blue sidebands, respectively. The resulting signal, carrier frequency and red and blue sidebands, are further amplified electronically before the signal is passed through a cavity resonant at 6.831 GHz. This cavity only allows signals close to the $F = 1 \rightarrow F = 2$ transition to pass through. To not be filtered out, we require the mixing RF frequency, ω_{RF}, to be

169 ± 10 MHz, which centres the red sideband on the hyperfine transition. This sideband filtering method allows the microwaves signal to be frequency and phase controlled via use of the RF DDS board, allowing for dynamic control of the Microwave frequency during the experiment, and phase resetting of the microwave signal, both useful tools to have. Once filtered the microwave signal is sent via SMA cable to the chamber mounted microwave antennae. Much like the RF signals, the Microwave signals are passed through a VCA, meaning that obtaining a high a power as possible (whilst maintaining signal integrity, and avoiding damaging fragile-high frequency components) remained the main objective. Figure 4.4.1 shows the setup created to achieve this.

Chapter 5

Microwave Transitions

With atomic transport around the ringtrap achieved, the next requirement for the experiment was the ability to create a coherent superposition of trappable atom states with which to perform interferometry. The caveat is that the two states of atoms within the superposition must couple to opposite-handed RF polarisations, the $F = 1$ and $F = 2$ states fulfill this requirement, by coupling to σ_- and σ_+ respectively. The two states have an energy separation of 6.834682 GHz, which is in the microwave range, and accessible through electronic generation. This Chapter will focus first on RF-Dressed microwave transitions, preparation of pure states. The second section will focus on the path to maximising the efficiency of the transfer from one state to another. The final section will the explore the creation of a quantum superposition of atomic states, and the coherence time of such states, and the implications of such coherence on an interferometer.

5.1 RF-Dressed Microwave Transitions

Single photon transfers between atomic states are governed by selection rules that greatly restrict the transitions available. In the case of driving between the $F = 1$ and $F = 2$ manifold, we are governed by the fact that the photon driving the transition must have a component in the σ_+/σ_- directions, meaning that the magnetic sub-level must increment by 1, or -1, depending on the polarisation of light used. This restriction, $\Delta m_f = \pm 1$ would normally be a problem for the trapping and transport scheme, as

it means that a direct transfer between the two closest trappable states in each hyperfine manifold, $|2,1\rangle$ and $|1,-1\rangle$ would not be possible. However, the presence of the RF-dressing field, coupling the magnetic sub-levels, together, allows for pseudo one-photon transitions through the absorption and stimulated emission of RF photons. These pseudo one-photon transitions are subject to their own set of polarisation based transition rules, shown in Figure 5.1

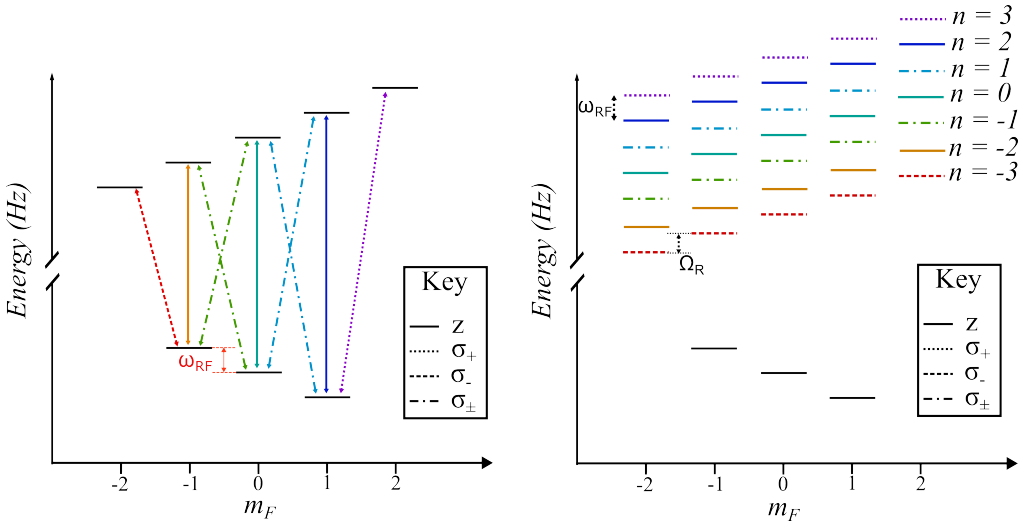

Figure 5.1: Left : Allowed Single photon transitions from the $F = 1$ manifold, colour coded based on energy separation, and with a linestyle that denotes the polarisation of MW pulse required to drive the transition. Right : The presence of RF dressing fields separates each allowed transition into its own group of transitions, labelled $n = 3, 2.... - 3$, colour coding and polarisation linestyles match between the two figures.

The coupling between m_f levels means that a single microwave photon can effectively drive an atom into any other $|F, m_f\rangle$ state. Transitions can be expected at frequencies [78]:

$$\omega_{|F,m_f\rangle \to |F+1,m'_f\rangle} = \omega_{HFS} + N\omega_{RF} + (\omega_{m_f} - \omega_{m'_f}) \tag{5.1}$$

Where ω_{HFS} is the hyperfine splitting frequency, $N\omega_{RF}$ indicates the number of RF photons absorbed or emitted (positive N means net absorption, negative N means net emission), and $(\omega_{m_f} - \omega_{m'_f})$ is the energy offset of both the initial and target state from the ground states, respectively. For the RF-dressed case, the energy offset is given by the Rabi splitting

$\omega_{m_f} = \bar{m}\Omega_{RF}$. From figure 5.1 we can see that the amount of RF absorption or emission transitions is limited to a maximum of ± 3. This, along with the Rabi splitting term leads to the spectrum as seen in figure 5.2, in which the RF-photon absorption-emission leads to 7 (The bare group ± 3) groups of transition peaks, all containing a complete set of transition peaks to the opposite hyperfine manifold (i.e. atoms in the $F = 2$ manifold see 3 transition peaks, as that is the amount of $F = 1$ states to be transferred to).

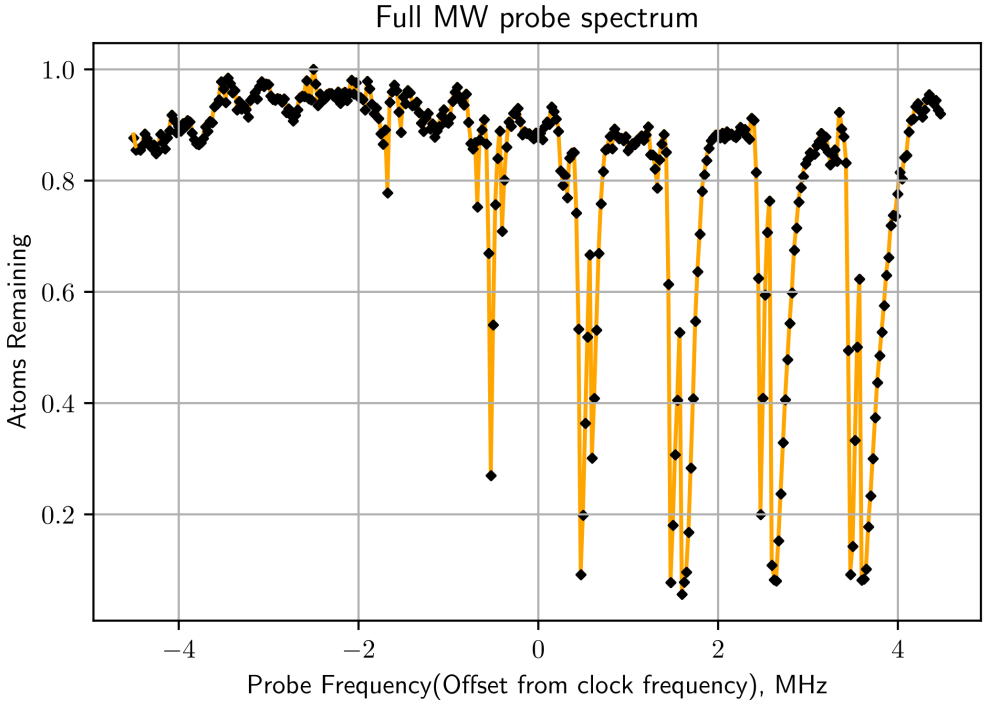

Figure 5.2: Microwave Spectrum encompassing the frequency range to see all 7 groups of transitions ($\omega_{RF} = 1$MHz), $\Omega_R \approx 150$kHz. We see diminishing coupling for negative groups, and are unable to see group $n = -3$ at all.

The existence of the multiple RF-transition groups, which have splitting ν_{RF}, are limited by the microwave polarisations that can drive atoms along them. We consider the microwave polarisation in the π,$\sigma_\pm$ basis, photons of microwaves in these polarisations provide an angular momentum change of 0,± 1 respectively, meaning they drive different transition groups depending on the sum of angular momenta changes for a given transition group.

5.1.1 Coupling Strengths

The spectrum in Figure 5.1 was taken using short microwave pulses, such that the transfer of atoms does not exhibit any oscillatory behaviour due to Rabi cycling. As a result, the peak heights, or atoms transferred, are proportional to the coupling strength of the microwave field and its polarisation. When considering the direct coupling between hyperfine manifolds, it is no longer sufficient to only consider the product $\hat{F} \cdot B$. Instead we consider how the entire fine J-manifold couples to the magnetic field, we create the Hamiltonian:

$$\hat{H} = \hat{J}' \cdot B, \tag{5.2}$$

where $\hat{J}'$ is the RF-dressed fine state matrix obtained from the tensor product of its two constituent RF-dressed $\hat{F}$ manifolds. Each of the three potential polarisations (σ_+, σ_-, and z) of MW field can couple to 3 transition groups each ($n = -1, 1, 3$ for σ_+,$n = -3, -1, 1$ for σ_-, and $n = -2, 0, 2$ for z), with 15 transitions for each group, means that there are a total of 45 different possible couplings for each polarisation, or 135 total couplings to consider. The coupling coefficients can be calculated by considering the dressing angles of the two manifolds :

$$\theta_F = \frac{\pi}{2} - \arctan\left(\frac{B_{DC} - B_{res,F}}{\sqrt{2}B_{RF}^{\pm}}\right) \tag{5.3}$$

The coupling coefficients for the σ_+ polarisation are listed below:

Transition	$n=-1$ coupling	$n=1$ coupling	$n=3$ coupling
$\|1,-1\rangle \leftrightarrow \|2,-2\rangle$	$-\frac{1}{\sqrt{2}}(1+\cos(\theta_1))\sin^2(\theta_2)$	$\sqrt{2}\sin(\theta_1)(1-\cos(\theta_2))\sin(\theta_2)$	$-\frac{1}{\sqrt{2}}(1-\cos(\theta_1))(1-\cos(\theta_2))^2$
$\|1,-1\rangle \leftrightarrow \|2,-1\rangle$	$\frac{1}{\sqrt{2}}(1+\cos(\theta_1))\sin(2\theta_2)$	$-\sqrt{2}\sin(\theta_1)(1+\cos(\theta_2)-2\cos^2(\theta_2))$	$\sqrt{2}(1-\cos(\theta_1))(1-\cos(\theta_2))\sin(\theta_2)$
$\|1,-1\rangle \leftrightarrow \|2,0\rangle$	$\frac{1}{\sqrt{3}}(1+\cos(\theta_1))(1-3\cos^2(\theta_2))$	$\sqrt{3}\sin(\theta_1)\sin(2\theta_2)$	$-\sqrt{3}(1-\cos(\theta_1))\sin^2(\theta_2)$
$\|1,-1\rangle \leftrightarrow \|2,1\rangle$	$-\frac{1}{\sqrt{2}}(1+\cos(\theta_1))\sin(2\theta_2)$	$\sqrt{2}\sin(\theta_1)(1-\cos(\theta_2)-2\cos^2(\theta_2))$	$\sqrt{2}(1-\cos(\theta_1))(1+\cos(\theta_2))\sin(\theta_2)$
$\|1,-1\rangle \leftrightarrow \|2,2\rangle$	$-\frac{1}{\sqrt{2}}(1+\cos(\theta_1))\sin^2(\theta_2)$	$-\sqrt{2}\sin(\theta_1)(1+\cos(\theta_2))\sin(\theta_2)$	$-\frac{1}{\sqrt{(2)}}(1-\cos(\theta_1))(1+\cos(\theta_2)^2$
$\|1,0\rangle \leftrightarrow \|2,-2\rangle$	$\sin(\theta_1)\sin^2(\theta_2)$	$2\cos(\theta_1)(1-\cos(\theta_2))\sin(\theta_2)$	$-\sin(\theta_1)(1-\cos(\theta_2))^2$
$\|1,0\rangle \leftrightarrow \|2,-1\rangle$	$-\sin(\theta_1)\sin^2(\theta_2)$	$-2\cos(\theta_1)(1+\cos(\theta_2)-2\cos^2(\theta_2))$	$2\sin(\theta_1)(1-\cos(\theta_2))\sin(\theta_2)$
$\|1,0\rangle \leftrightarrow \|2,0\rangle$	$-\sqrt{\frac{2}{3}}\sin(\theta_1)(1-3\cos^2(\theta_2))$	$\sqrt{6}\cos(\theta_1)\sin(2\theta_2)$	$-\sqrt{6}\sin(\theta_1)\sin^2(\theta_2)$
$\|1,0\rangle \leftrightarrow \|2,1\rangle$	$\sin(\theta_1)\sin(2\theta_2)$	$2\cos(\theta_1)(1-\cos(\theta_2)-2\cos^2\theta_2))$	$2\sin(\theta_1)(1+\cos(\theta_2))\sin(\theta_2)$
$\|1,0\rangle \leftrightarrow \|2,2\rangle$	$\sin(\theta_1)\sin^2(\theta_2)$	$-2\cos(\theta_1)(1+\cos(\theta_2))\sin(\theta_2)$	$-\sin(\theta_1)(1+\cos(\theta_2))^2$
$\|1,1\rangle \leftrightarrow \|2,-2\rangle$	$-\frac{1}{\sqrt{2}}(1-\cos(\theta_1))\sin^2(\theta_2)$	$-\sqrt{2}\sin(\theta_1)(1-\cos(\theta_2))\sin(\theta_2)$	$-\frac{1}{\sqrt{2}}(1+\cos(\theta_1))(1-\cos(\theta_2))^2$
$\|1,1\rangle \leftrightarrow \|2,-1\rangle$	$\frac{1}{\sqrt{2}}(1-\cos(\theta_1))\sin(2\theta_2)$	$\sqrt{2}\sin(\theta_1)(1+\cos(\theta_2)-2\cos^2(\theta_2))$	$\sqrt{2}(1+\cos(\theta_1))(1-\cos(\theta_2))\sin(\theta_2)$
$\|1,1\rangle \leftrightarrow \|2,0\rangle$	$\frac{1}{\sqrt{3}}(1-\cos(\theta_1))(1-3\cos^2(\theta_2))$	$-\sqrt{3}\sin(\theta_1)\sin(2\theta_2)$	$-\sqrt{3}(1+\cos(\theta_1))\sin^2(\theta_2)$
$\|1,1\rangle \leftrightarrow \|2,1\rangle$	$-\frac{1}{\sqrt{2}}(1-\cos(\theta_1))\sin(2\theta_2)$	$-\sqrt{2}\sin(\theta_1)(1-\cos(\theta_2)-2\cos^2(\theta_2))$	$\sqrt{2}(1+\cos(\theta_1))(1+\cos(\theta_2))\sin(\theta_2)$
$\|1,1\rangle \leftrightarrow \|2,2\rangle$	$-\frac{1}{\sqrt{2}}(1-\cos(\theta_1))\sin^2(\theta_2)$	$\sqrt{2}\sin(\theta_1)(1+\cos(\theta_2))\sin(\theta_2)$	$-\frac{1}{\sqrt{2}}(1+\cos(\theta_1))(1+\cos(\theta_2)^2$

Table 5.1: Coupling coefficient equations in terms of θ_1, and θ_2. Couplings are shown only for σ_+ transitions (Other polarisations can be found at [35]

5.1.2 Peak Widths

The other main variance between transition peaks, besides their differing coupling strengths, is the width of the peaks. When transitioning between Zeeman substates with a different magnetic sensitivity ($m_F \cdot g_F$), there is a gradient difference between the two trapping potentials. Atoms at higher field values, due to being higher energy in the thermal distribution, will see a greater potential change when transferred into the new state, compared to atoms at the bottom of the trap. This causes the transition peak to be broadened by Δm_F thermal distributions, as shown in Figure 5.3.

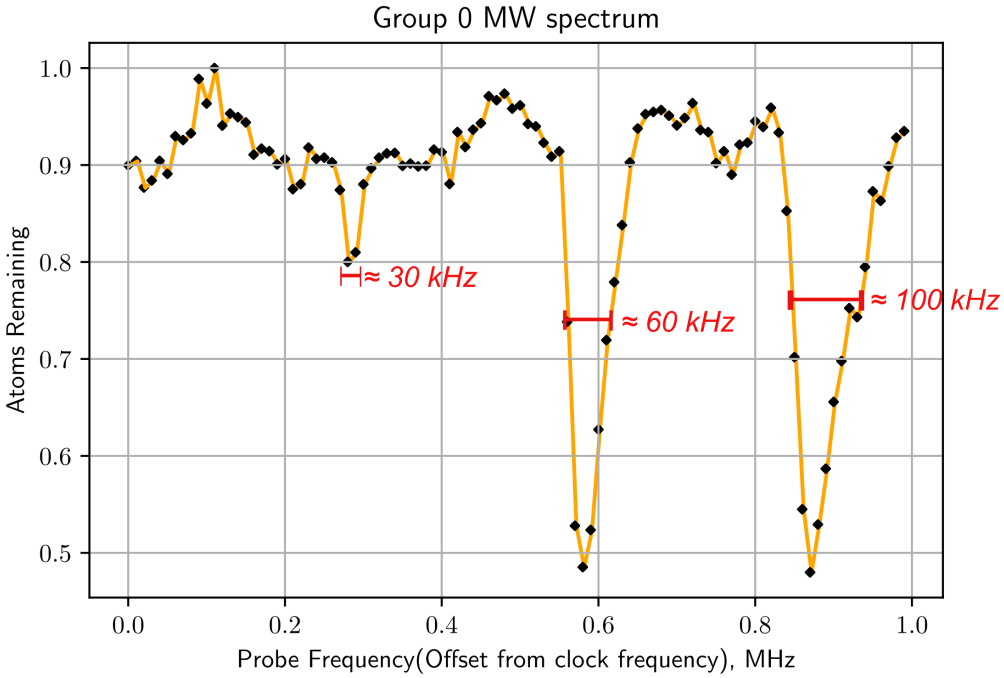

Figure 5.3: Linewidths for the $|2,2\rangle$ transitions on group 0. The leftmost peak, the $|2,2\rangle \rightarrow |1,-1\rangle$ transition has a width of 1 thermal distribution, while further transitions are broadened by Δm_F thermal distributions.

This causes another limitation on experimental parameters if we want to resolve individual transition peaks, in that we are often at risk of peaks overlapping (as can be seen somewhat in Figure 5.2). There are two considerations to make, firstly the RF Rabi frequency must be small enough that all the transitions within a group actually fit inside the group itself, i.e. for the $F = 1$ state, we see 5 possible transitions, so the RF Rabi frequency must be less than 0.2 times the RF dressing frequency. Secondly, we need to cool the atoms down such that the maximum transition extent is not greater than the RF Rabi frequency, for the $|1,-1\rangle$ state, this means that 3 times the thermal distribution width must not be greater than 200 kHz, setting a lower limit on our cloud temperature. These conditions are able to be controlled by modulating the RF Rabi frequency such that it is around 180 kHz, slightly smaller than 0.2 times that RF dressing frequency of 1 MHz, and cooling the atoms to the sub micro-Kelvin range, narrowing the transition widths to tens of kHz.

5.2 Atomic State Transfer

Since the optical pumping phase at the beginning of the experiment, the atoms have remained in the $|2,2\rangle$ state. Atoms in this state are unable to be used in the interferometric process as there is no Zeeman sub-state with the matching magnetic sensitivity to be found in the $F = 1$ manifold. Instead, we transfer atoms to the $|1,-1\rangle$ state, with the intention of using this state into a superposition with the $|2,1\rangle$ state. Due to how few atoms are left in the trap at this stage, owing primarily to the multiple evaporative cooling stage implemented, it is of great importance that the transfer between the $|2,2\rangle$ and $|1,-1\rangle$ states is as efficient as possible; otherwise, the contrast in absorption imaging becomes low enough that future measurements become very difficult. There are two methods that can be used to drive atoms between two states - Rabi Pulses, and Raman Transitions. Rabi pulses, where the coupling field is applied resonantly, drives atoms between the two states in a cyclical manner. Provided perfect coherence, the probability, $|c_+(t)|^2$, to find an atom in an excited state $|+\rangle$ is given as [84]:

$$|c_+(t)|^2 \propto \frac{\Omega_R^2}{\Omega_R^2 + \Delta^2} \sin^2\left(\frac{(\Omega_R^2 + \Delta^2)t}{2}\right) \tag{5.4}$$

Where both the Rabi frequency at resonance Ω_R, and detuning Δ play a role in how the superposition generated by the Rabi pulse cycles. Figure 5.4 shows the comparison between theoretical Rabi cycles, and the Rabi flopping that occurs to coherence decay.

To maximise transfer efficiency to the $|1,-1\rangle$ state, all we must do is apply an on resonance MW pulse for exactly half a Rabi cycle (a π-pulse, for short).

The other method we can utilise to perform the transfer is by making use of Stimulated Raman Adiabatic Passages (STIRAPs) [89, 27]. Due to the RF-Dressed energy levels, we can skip the requirement of having an intermediate state, and have the STIRAP directly transfer atoms from the $|2,2\rangle$ state to the $|1,-1\rangle$ state. To do this, we first create a microwave field that is far red-detuned from the transition (such that it does not transfer any atoms via Rabi pulse). By ramping the field frequency through the transition peak, we are able to stimulate an adiabatic transfer between the

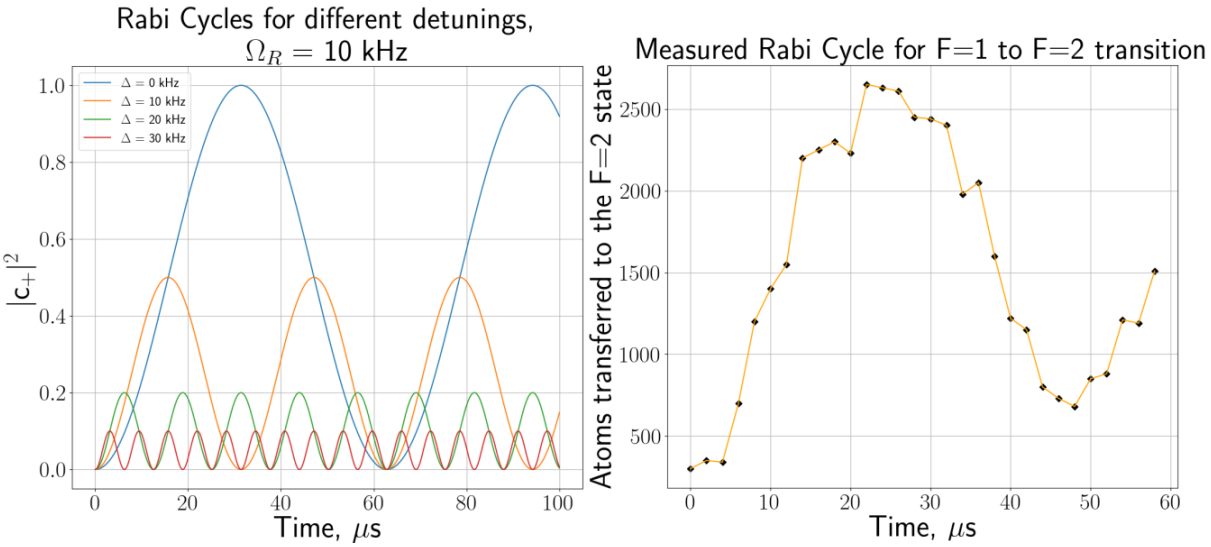

Figure 5.4: Left : Simulated Rabi cycles for a probe that induces a Rabi frequency of 10kHz, for different detunings. Right : Experimental measurements of the Rabi frequency of the MW probe at max power. We probe the $|1,-1\rangle \rightarrow |2,1\rangle$ transition, and observe a Rabi frequency of $\approx$ 10kHz

two states, theoretically transferring every atom from the $|2,2\rangle$ state to the $|1,-1\rangle$ state. This requires a slow ramp through the atomic cloud, where the adiabatic condition is given by:

$$\dot{\omega} \ll \omega_L, \tag{5.5}$$

such that the atomic spin can adiabatically follow the raman frequency ramp.

Comparing the density of the clouds after each process side by side shows that Rabi pulses are a superior method of atom transfer. This is likely a result of digital effects that derive from the bit rate of the DDS system that generates the RF currents. It can be shown [63] that for a frequency ramp of N steps, the fraction of atoms transferred to the excited state is given as:

$$\frac{N(|e\rangle)}{N(|g\rangle)} \approx 1 - \frac{F}{2N}\left(\frac{4\pi\Delta\omega}{g_J B_{MW}}\right)^2, \tag{5.6}$$

where F is the total atomic spin, and $\Delta\omega$ is the frequency range of the ramp. If we want to achieve a 90% transfer rate, we expect the minimum

number of frequency steps required to be:

$$N_{MIN} = 5F \left(\frac{4\pi\Delta\omega}{g_J B_{MW}} \right)^2 \tag{5.7}$$

Using this, we expect the transfer pulse between the $F = 1$ and $F = 2$ manifolds to require on the order of 100,000 frequency steps, or $2^{16.6}$, meaning a 16-bit encoded ramp would not appear adiabatic.

It is preferable, when using the Rabi-pulse transfer method, to maximise the coupling of the MW field to the atoms, so as to maximise the Rabi frequency of the transfer. The means that atoms transfer into the desired state faster, and are less susceptible to lossy effect, such as noise during the transfer, or coherence decay effects, that reduce the contrast of the superposition generated by the Rabi pulse. In an effort to improve this coupling, we trialled two different sources of MW field: The MW antennae, mounted inside the vacuum chamber, and a MW horn, mounted externally. The MW horn is significantly further from the atomic cloud than the MW antennaae, but has a known, controllable polarisation that we can align to the atoms quantisation axis, and emits field directionally, so can be aimed directly at the atom cloud, where the MW antennae produces field in all directions.

Initial testing performed through attempting to drive the $|2, 2\rangle \rightarrow |1, -1\rangle$ transition revealed that the MW antenna was superior, able to achieve kHz Rabi frequencies, where the MW horn was barely able to drive the transition at all (to the point at which one could not measure the Rabi frequency, as the transition time is significantly longer than the decoherence time of the resulting superposition). As such, the MW antenna is used for all results going forward.

5.3 Superposition and Coherence

The state-dependent transport that forms the backbone of the rotational interferometer necessitates having two atomic states with opposite Landé g-factor signs, and the Ramsey Bordé sequence requires they be in a coherent superposition. We can achieve this experimentally by creating a quantum superposition of the $|1, -1\rangle$ and $|2, 1\rangle$ hyperfine states. This superposition

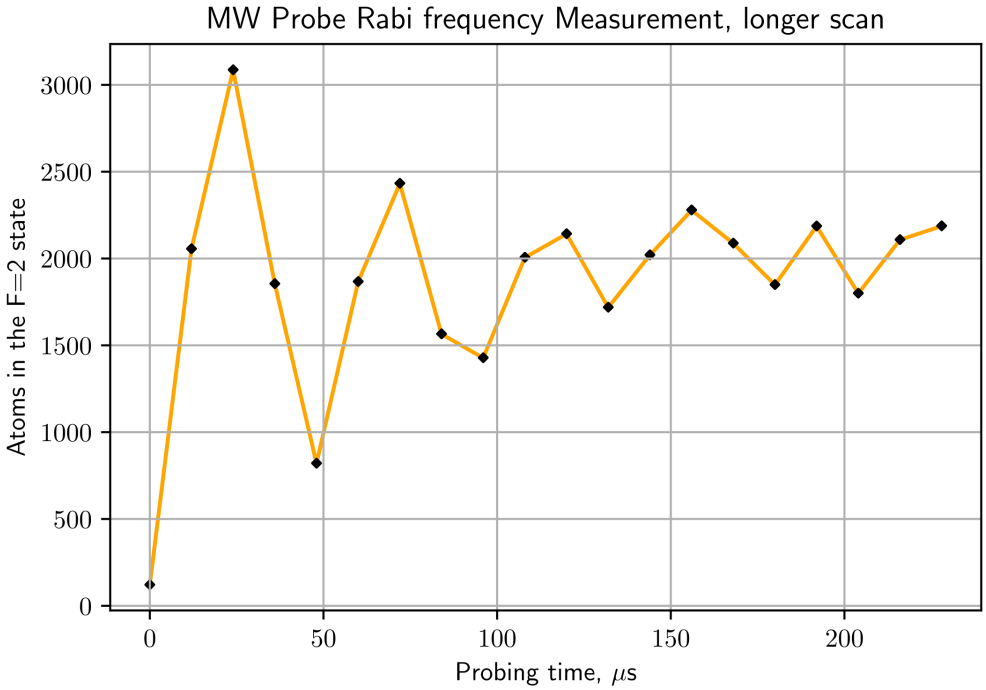

Figure 5.5: Coherence decay of Rabi oscillations, as a function of probing time. The $|1,-1\rangle \rightarrow |2,1\rangle$ was probed, with probe strength $\Omega_R \approx 10$kHz

is able to be creates via Rabi pulse, and we can observe the superposition by looking at the Rabi oscillations between the two states, shown in Figure 5.5.

As the Rabi oscillations continue, we notice a decay in the contrast between the two states, instead flattening out somewhere in the middle. This is the principle of decoherence, a process by which quantum superpositions decay out of their superposition state into mixture states. To perform interferometry successfully, we wish for the superposition to remain coherent throughout the entire interferometric sequence, which, as mentioned earlier, is 200 ms. Taking a cursory glance at the Rabi oscillations, however, suggests that decoherence occurs on the order of hundreds of microseconds, out by a factor of one thousand.

We can obtain a more accurate measurement of the coherence time by performing spin-echo sequences, a form of mock Ramsey-Bordé interferometry, wherein we artificially generate Ramsey fringes via experimental control. To perform this experimentally, we prepare a pure $|1,-1\rangle$ state,

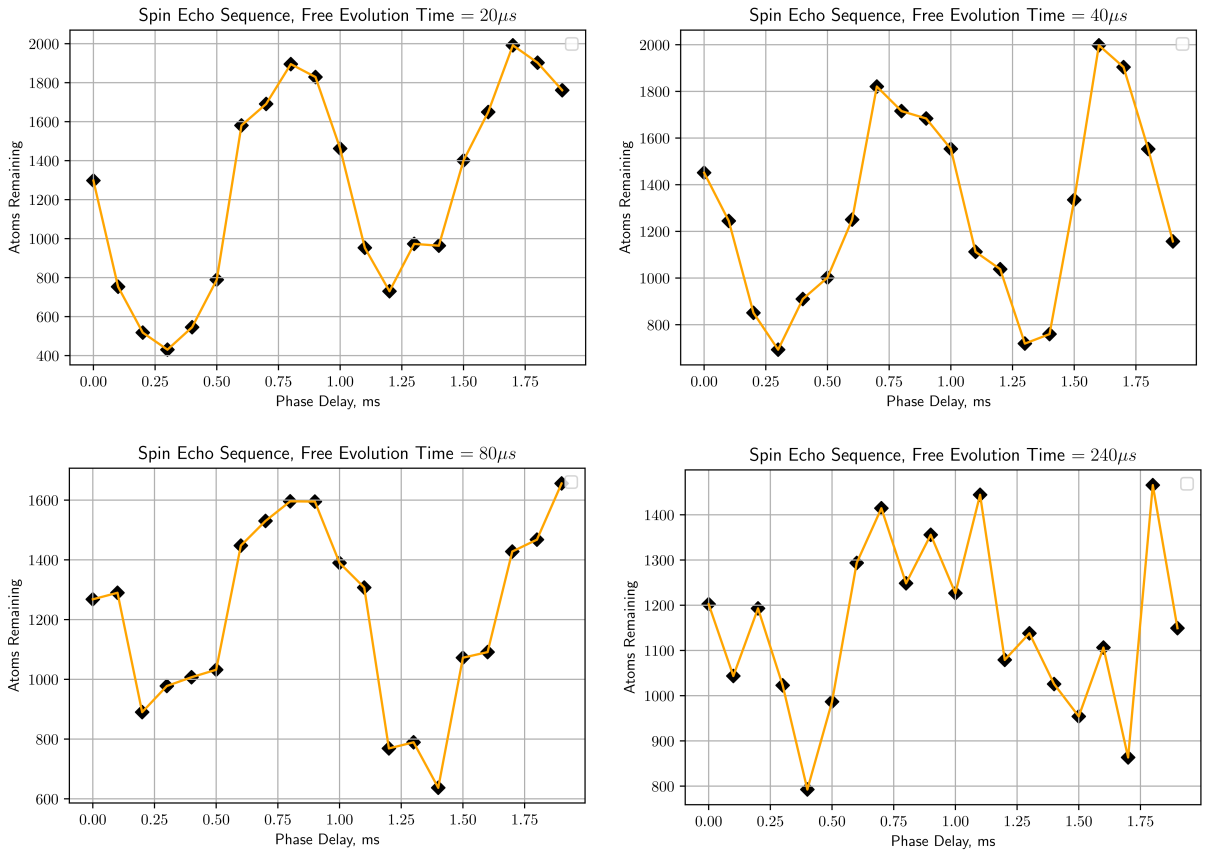

Figure 5.6: Ramsey fringes induced via spin echo sequences of varying free evolution time. Atom numbers are generally low after the sequence, producing poor imaging results, still the contrast can be obtained.

which is then driven into a fifty-fifty superposition via a $\frac{\pi}{2}$ Rabi pulse. We then perform a ramsey sequence as detailed in Chapter 2, but do not displace the atomic clouds during the free evolution time. To generate the Ramsey fringes, we shift the phase of the final Rabi pulse (the recombination $\frac{\pi}{2}$-pulse) by an amount ϕ, as ϕ varies from 0 to 2π we expect to see two Ramsey fringes. We can define the contrast, $\mathcal{C}$ of the fringes as:

$$\mathcal{C} = \frac{\max(N) - \min(N)}{\max(N) + \min(N)}, \tag{5.8}$$

where N is the amount of atoms in the $|2,1\rangle$ state. We preform this experiment multiple times for different durations of free evolution time, and measure how the fringe contrast decreases with the duration. The expected

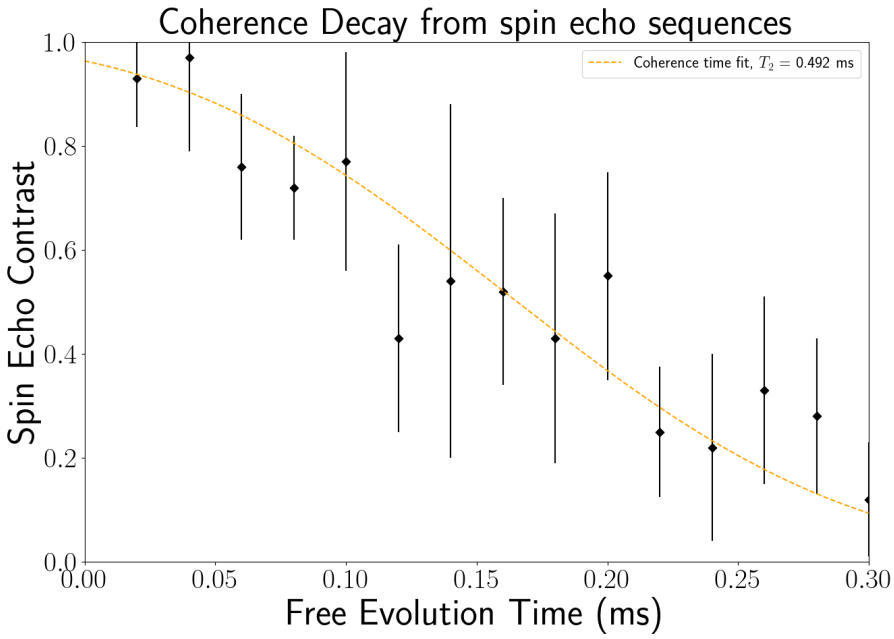

Figure 5.7: Contrast Decay as a function of free evolution time, we define a free evolution time step as the time between two Ramsey pulses, meaning the actual time atoms evolve for its twice that.

contrast as a function of time for spin echo sequences is [25]:

$$\mathcal{C}(t) = \exp\left((\frac{2nt}{T_2})^3\right), \tag{5.9}$$

where n is the number of consecutive echo sequences performed (one, in our case), and T_2 is the $\frac{1}{e}$ decay time. Figure 5.6 shows a selection of the spin echo data taken, showing thedecay in contrast for longer free evolution times. From Figure 5.7 we can observe a decay time on the order of 0.5 ms, much better than our initial assumptions from the Rabi cycles, but a long way off the desired 200 ms. We will discuss the cause of this low coherence time, and its potential solutions, in the next chapter.

Chapter 6

Coherence Control

In the previous chapter we highlighted a problem on the path to a functioning interferometer: The rapid decoherence of superpositions of states in the interferometer. This chapter will both explain how such decoherence is baked into the design of the interferometer, and a technique for solving the problem. This chapter will be split into three parts, the first will describe and quantify the problem that generates the decoherence issue, namely trap mismatch. The second section will describe the experimental technique used to combat the problem, Microwave-dressed potentials, showing the theoretical construction and experimental implementation.

6.1 Source of Decoherence : Trap Mismatch

In previous calculations of atom trapping, it was assumed that, for the $F = 1$ and $F = 2$ states, the gyromagnetic ratios were $g_{F1} = -0.5$ and $g_{F2} = 0.5$. As discussed in chapter 2, however, the alignment or anti alignment of the nuclear angular orbital momentum causes a discrepancy between the two gyromagnetic ratios, where $g_{F1} = -0.5018267$ and $g_{F2} = 0.4998364$, a magnitude difference of 0.5%

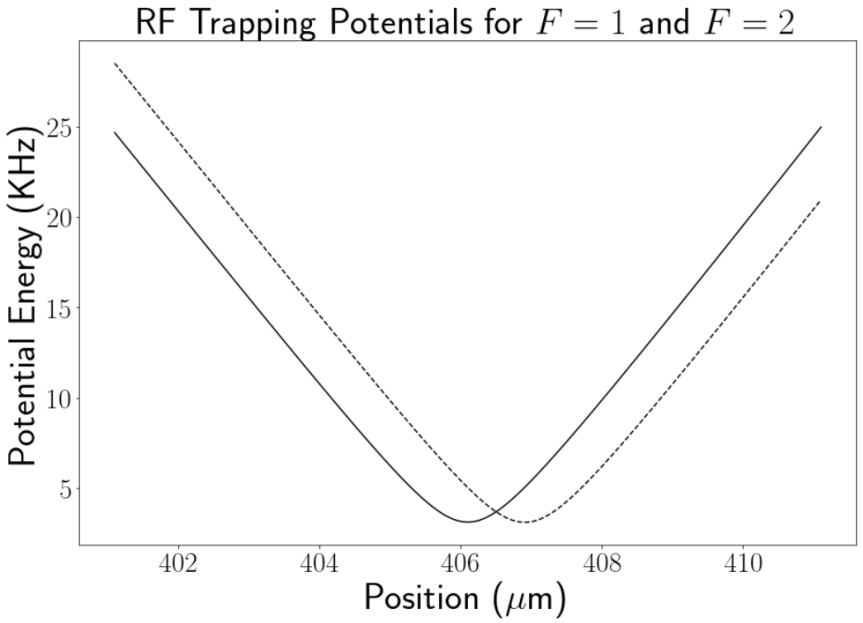

Figure 6.1: Difference in trapping potentials (in the RF-dressed ringtrap) that arise due to the difference in gyromagnetic ratios between the $F = 1$ and $F = 2$ states.

Figure 6.1 shows how this difference in gyromagnetic ratios manifests for atoms loaded in the RF-dressed ringtrap. The trap minimas are offset from one another by around $1\mu m$ and the trap curvatures differ by 0.5%. What is not really visible is that the $F = 2$ trap also has a higher trap gradient, meaning that the confining force for atoms in the $F = 2$ trap is also 0.5% higher.

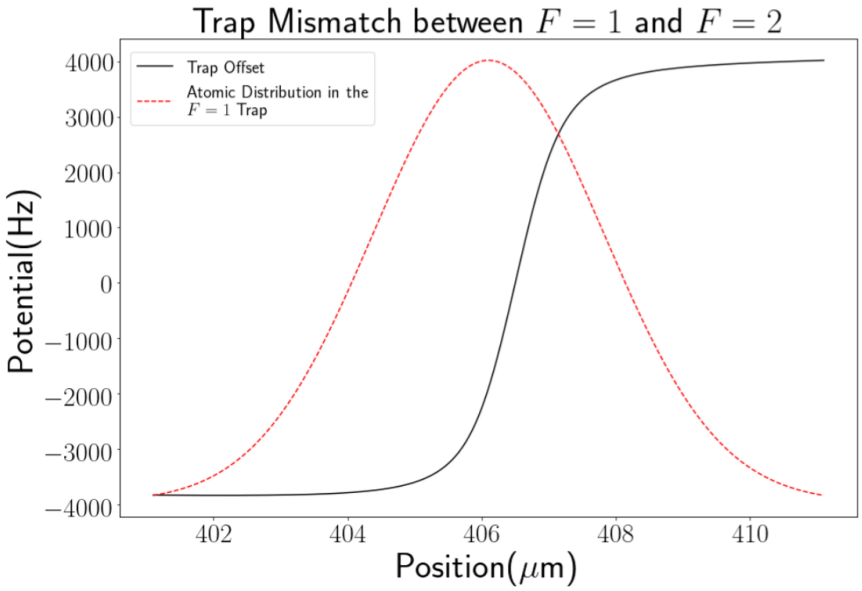

Figure 6.2: Plot that combines the difference in potential between the $F = 1$ and $F = 2$ traps. The thermal (T= 1μk) distributions of atoms in the $F = 1$ (red) and $F = 2$ (blue) traps are also shown.

Figure 6.2 exemplifies this problem, as it can be seen that, over the atomic distributions, the difference in potentials between the two traps is 8kHz, and atoms at temperatures as low as 1μK are able to spread across the full width of this mismatch. The spectral linewidth of the transition between the two traps can be computed, this is shown in Figure 6.3. We calculate these linewidths under the assumption that the effect of atomic motion is negligible to the probe, this assumption is valid. We then see that for an atomic cloud at 1μK, we expect to have a transition linewidth of $\approx$ 8kHz. Taking a naive approach to coherence time, and transition linewidths, based on field correlations, we assume the coherence time to be directly proportional to the linewidth of the transition. If we are seeing 500μs coherence time for 8 kHz, then achieving a 200 ms coherence time would require a linewidth of $\approx \frac{8000}{400} = 20$Hz.

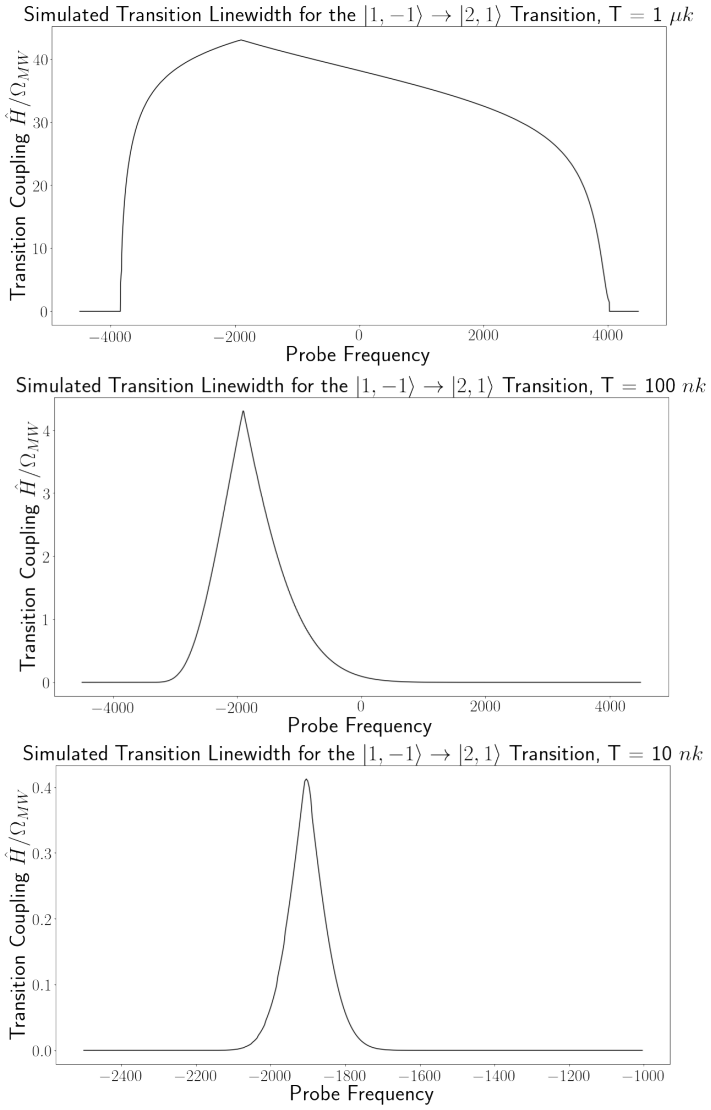

Figure 6.3: Simulated Linewidths for the $|1,-1\rangle \rightarrow |2,1\rangle$ transition, for cloud temperatures of $T = 1000, 100$, and 10 nk. The final peak has had the probe frequency scan range reduced, to better see the peaks.

6.1.1 Coherence simulation

To convince ourselves that the reduced coherence observed was primarily the effect of a broadened linewidth, and not simply due to thermal atomic motion about the detuning profile seen in Figure 6.2. To do this we made use of a numerical simulation of a spin echo sequence applied to a two level atom. For such a spin echo sequence we are interested in obtaining the

expectation value of the $|+\rangle$ state, given by:

$$E(|+\rangle) = \left\langle \hat{U} \right| \hat{\sigma}_z \left| \hat{U}_{\pm} \right\rangle \tag{6.1}$$

In which we introduce the rotation operator for the entire sequence, $\hat{U}$, which is an state of the Pauli spin matrix $\hat{\sigma}_z$ (and acts as a rotation about the x-axis). We can obtain the rotation operator by diagonalising the exponential of the Hamiltonian:

$$\hat{U} = P \exp\left(-i\frac{\hat{H}}{\hbar}t\right) P^T \tag{6.2}$$

Where P is the diagonalising matrix that takes the form of the tensor product of the eigenvectors of $\hat{H}$. An atom being resonantly driven by a single pulse of coupling Ω and that has detuning from the pulse frequency of $\Delta - \omega_0 - \omega$, is expressed by the following Hamiltonian:

$$\hat{H} = \Omega(\cos(\alpha)\sigma_x + i\sin(\alpha)\sigma_y) + \Delta\sigma_z \tag{6.3}$$

The diagonalization matrix of this Hamiltonian is thus:

$$P = \begin{bmatrix} -\Delta - \frac{\sqrt{\Delta^2+\Omega^2}}{\Omega\exp(-i\alpha)} & 1 \\ 1 & -\Delta + \frac{\sqrt{\Delta^2+\Omega^2}}{\Omega\exp(-i\alpha)} \end{bmatrix} \tag{6.4}$$

We can then simulate the effect of this on atoms by simulating a spin echo sequence on atoms, setting $\alpha = 0$ and introducing α' which denotes the changed phase of a pulse; thus the total rotation operator for the whole sequence $\hat{U}_T$ can be written as:

$$\hat{U}_T = \hat{U}_{\frac{\pi}{2}}(\alpha)\hat{U}_{ev}\hat{U}_{\pi}(\alpha')\hat{U}_{ev}\hat{U}_{\frac{\pi}{2}}(\alpha) \tag{6.5}$$

Where the type of pulse is denoted by the subscript, with ev being a free evolution stage, which allows us to simulate the motion of atoms in the trapped potential. The expectation value of the $|+\rangle$ state ranges between -1 and 1, we can use this to find the contrast of the Ramsey fringes as:

$$\mathcal{C} = \frac{\max(E(|+\rangle + 1) - \min(E(|+\rangle + 1)}{\max((E(|+\rangle + 1) - \min(E(|+\rangle + 1)} \tag{6.6}$$

Figure 6.4 allows us to see how the contrast decays as a function of free evolution time. This simulation allows us to measure the coherence decay that arises due to the thermal motion of atoms about the two mismatched traps, and how the change in detuning of the Rabi pulses during the sequence gives rise to reduced fringe contrast.

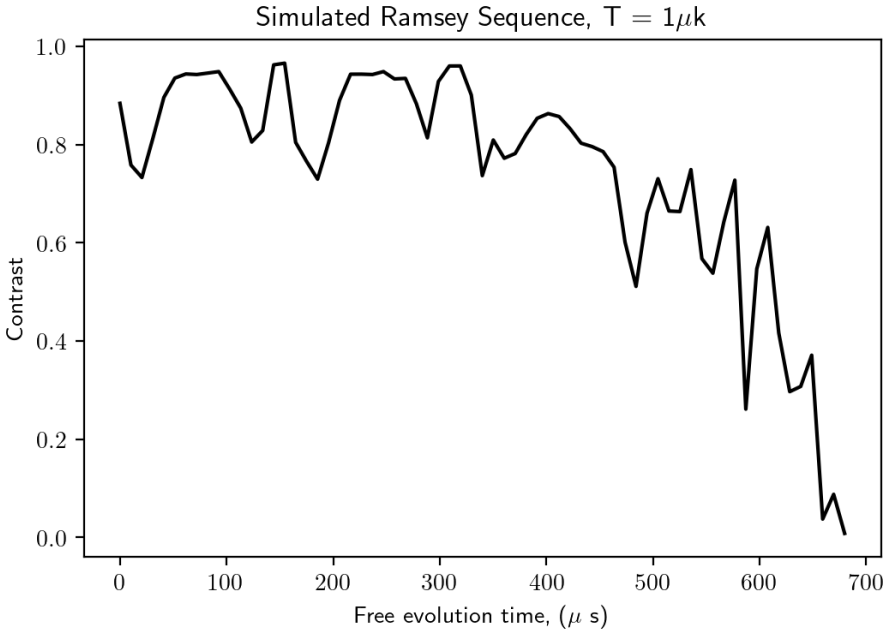

Figure 6.4: Computational Ramsey sequence performed on atoms at 1μK. This simulation does not take into account the effect of linewidth broadening, and instead considers atoms moving about a detuning potential,in between Ramsey pulses.

We can see from this simulation that without linewidth broadening effects, we expect a longer coherence time, by around a factor of two (while it is not necesarily appropriate to use the same theoretical model as with our experimental spin echo sequences, we can see that the contrast remains high for around 500-600 ms, as opposed to the 300 experimentally).

6.1.2 The effect of Temperature

It can be seen in Figure 6.3 that the linewidth is drastically reduced if we are able to cool the atomic cloud down to 100 nk. We can see from Figure 6.5 that cooling the cloud down by a factor of 1000 reduces the

span of the thermal distribution across the offset region by a factor of ≈ 200. However, performing this experimentally is unfeasible due to practical considerations. Firstly, the additional evaporative cooling required to reach even 100 nk would reduce the contrast even further, and since we are below the limit to which we can efficiently cool atoms, it is likely that lowering the temperature any further would reduce the contrast of the absorptive imaging below a useful level.

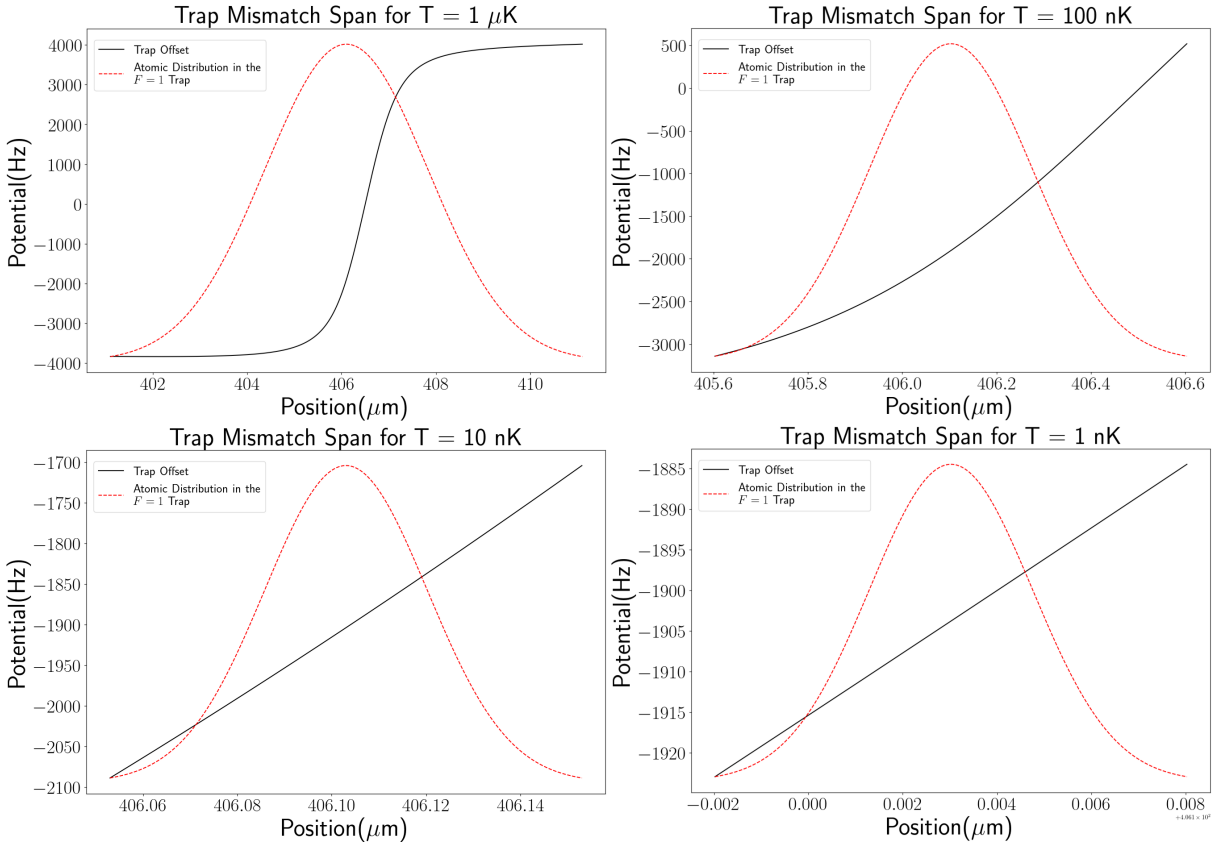

Figure 6.5: Spans of the thermal distribution over the trap offset for different temperatures. By reducing the temperature from 1μK to $1n$K we see a reduction in potential offset span from $8kHz$ down to $35Hz$. This assumes that the cloud remains thermal gas, and does not collapse into a BEC state, where we would see the energy distribution narrow significantly.

Secondly, due to the process of parametric heating, atoms driven between the two potentials, more often than not end up with a higher potential energy in the new state than the state from which they were driven. The atom will then roll down the potential, gaining kinetic energy, and

increasing the temperature of the atom cloud (shown in Figure 6.6. This process effectively limits the temperature to which atoms may be cooled.

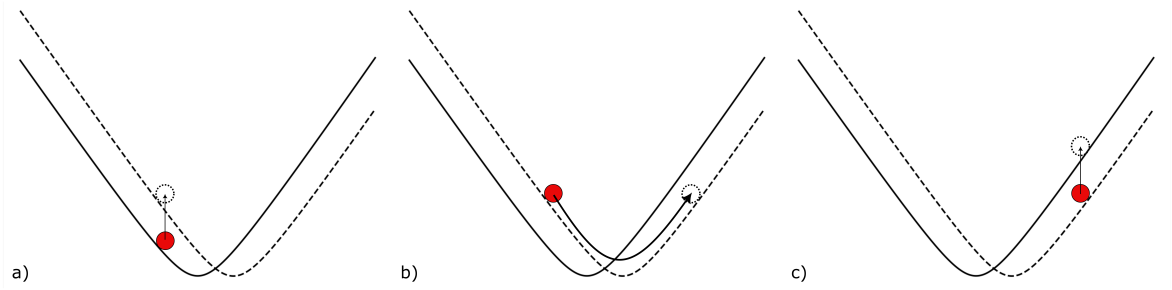

Figure 6.6: Diagram showing the process of parametric heating. a) an atom is driven between the two potentials, ending in a higher potential state.b) The atom rolls down its new potential, until it reaches the other side of the trap. c) The atom is transferred back into its original trap, now with a significantly higher energy than it had before this process began.

6.2 Microwave-Dressed Potentials

The negative effects of the trap mismatch, and thus the broadened linewidth, can be negated by simply shifting the two potentials on top of each other, removing the mismatch, the linewidth broadening, and increasing the coherence time of a superposition between the two states. The method we seek to exploit to achieve this is the AC-Stark shift, in a similar vein to how detuned laser light can be used to form dipole traps, or optical plugs, The rough idea behind this is shown in Figure 6.7. This section will discuss the theoretical formulation of this method, and the process and results of implementing it with the RF-dressed ringtrap. Any two RF-dressed magnetic sub-levels can be directly coupled through the use of a single microwave photon. This coupling, when sufficiently weak, can be considered as a small perturbation applied to a spin-half system. Such an assumption requires that any microwave coupling field be smaller than the RF field that couples the sub-levels in each hyperfine manifold. The bare hamiltonian of such a system, with an energy separation between the two levels of ω_0 is :

$$\hat{H}_0 = \frac{\hbar}{2}\begin{bmatrix} \omega_0 & 0 \\ 0 & -\omega_0 \end{bmatrix} \tag{6.7}$$

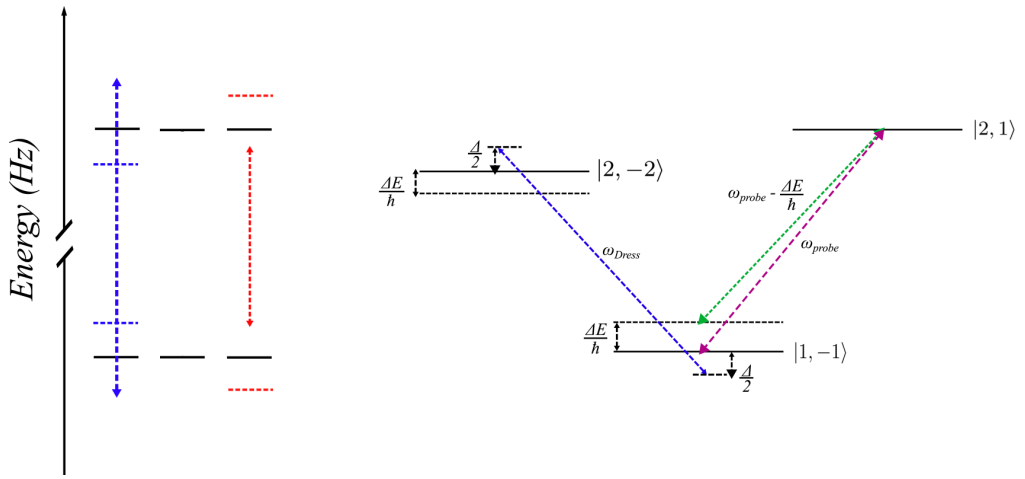

Figure 6.7: Illustration showing the theory behind MW dressing. Left : Two arbitrary energy levels are coupled with blue detuned, and red detuned light, inducing shifts in its energy splitting (coloured dashed lines) Right : A blue detuned field is applied to the $|1,-1\rangle \rightarrow |2,-2\rangle$ transition, shifting their energy levels, and changing the resonance frequency of the $|1,-1\rangle \rightarrow |2,1\rangle$ transition.

We can introduce a circularly-polarised coupling field with coupling strength Ω_D and frequency ω

$$\hat{H}_{AC} = \Omega(\cos(\omega t)\sigma_x - i\sin(\omega t)\sigma_y) \tag{6.8}$$

Solving for the eigenenergies of this Hamiltonian gives us an energy shift of:

$$\Delta E_{\pm} = -\Delta \pm \sqrt{\Omega^2 + \Delta^2} \tag{6.9}$$

The reliance of the energy shift on both the detuning from a given transition, Δ, and the coupling between the two states, Ω_{MW}, grants us two facets of control over how a microwave dressing field can influence the potentials. The $\pm$ refers to the sign of the detuning, where $+$ indicates a red detuning, and $-$ a blue detuning. Looking back to Section 5.1.1, we recall that the coupling strengths for different transition peaks have vastly different dependencies on static and RF field strengths, as such we can freely choose from any transition peak as the basis for our dressing field, choosing in such a way that it cancels out the potential mismatch

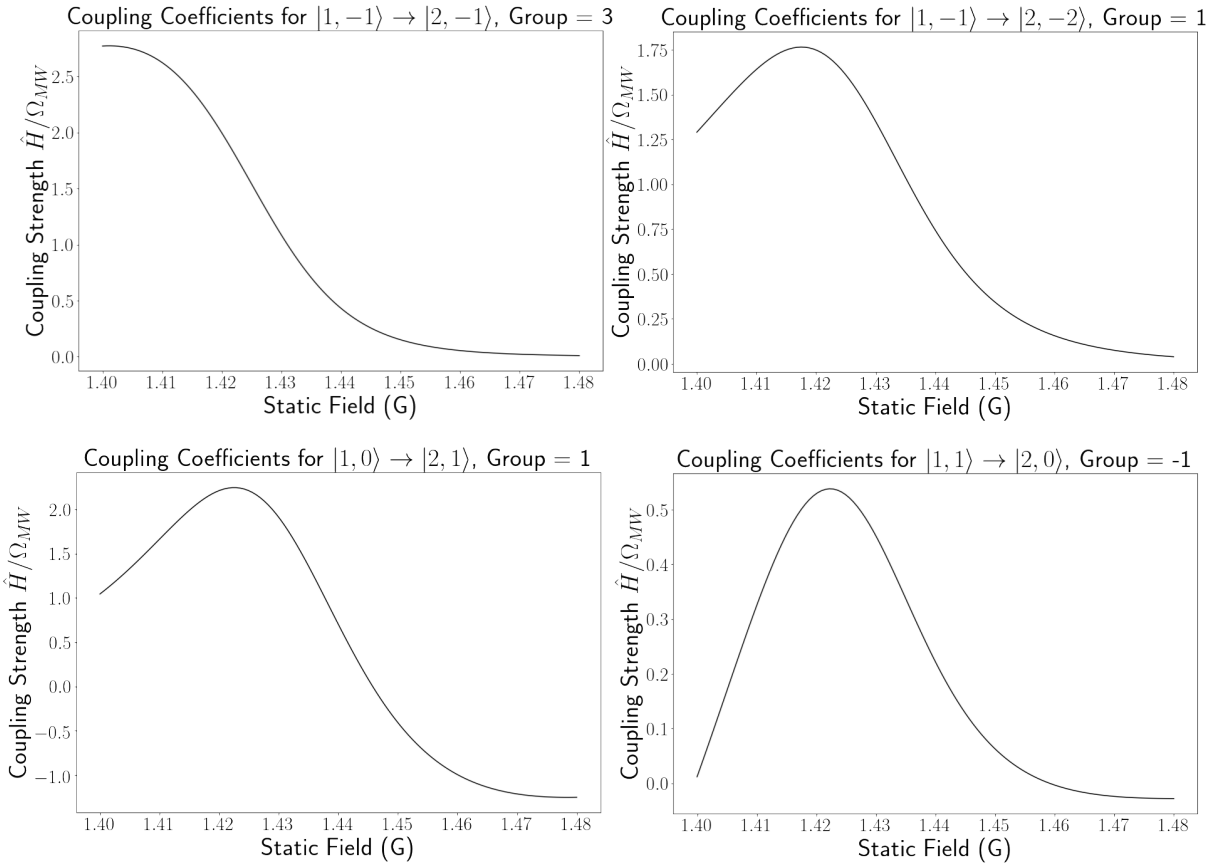

Figure 6.8: Coupling coefficient curves for 4 of the RF dressed MW transitions. All four of these curves have a roughly opposite geometry to the trap mismatch, making them ideal candidates for MW dressing schemes

(so long as the transition chosen couples either the initial $|1,-1\rangle$, or final $|2,1\rangle$ state). A few example coupling curves, that appear to have roughly opposite geometries to the trap mismatch, are shown in Figure 6.8.

6.2.1 High Temperature Linewidth Reduction

We begin our application of MW dressing fields with the aim of reducing the linewidth of the transition at the higher temperature of 1μK, as we know that the temperature is achievable experimentally. This means that there is a large area of the trap that must be shifted, in order to minimize linewidth. We can see the effects of applying a dressing field, blue detuned from the $|1,1\rangle \rightarrow |2,1\rangle$ transition, and applying it with different values of B_{MW}, inducing different coupling strengths. For the purposes of

these simulations, we assume that the dressing field is polarised correctly to drive the transition it is detuned from, without this assumption, the field values used would be shifted by some static multiplier, depending on the antennae's polarisation.

We can see from Figure 6.9 that as a dressing field is applied, the shift in trap offset causes a noticeable reduction in peak width. We also start to see some interesting geometries for the transition, where the peak splits in two. This happens as a result of the trap offset geometries, where there are large amounts of atoms at the turning points of the trap offset, meaning many atoms sit at a single frequency, compared to the high gradients in between. This effect would not be measurable experimentally due to atomic motion averaging these features out. We see maximal peak width reduction between 3.33 mG, and 10 mG

By scanning over the peak width for different dressing powers, as seen in Figure 6.10, we can observe that maximum narrowing of the peak comes at ≈ 7.8 mG of dressing field, where we see the peak width narrowed down to ≈ 2.8 kHz. This is a narrowing of the peak by a factor of three, and thus should increase coherence time by a factor of three, also. Nevertheless this is not enough, we must look to other improvements to meet the 200 ms coherence time requirement.

6.2.2 Low Temperature Linewidth Reduction

When we look at the shifted potentials in Figure 6.9, we notice that at the centre of the distribution, the trap offset turns on itself with increasing microwave field. That turning creates a small region of the trap offset that, if atoms were able to be cooled enough such that the entire distribution sat within that turning region, we would see a significant reduction in peak width.

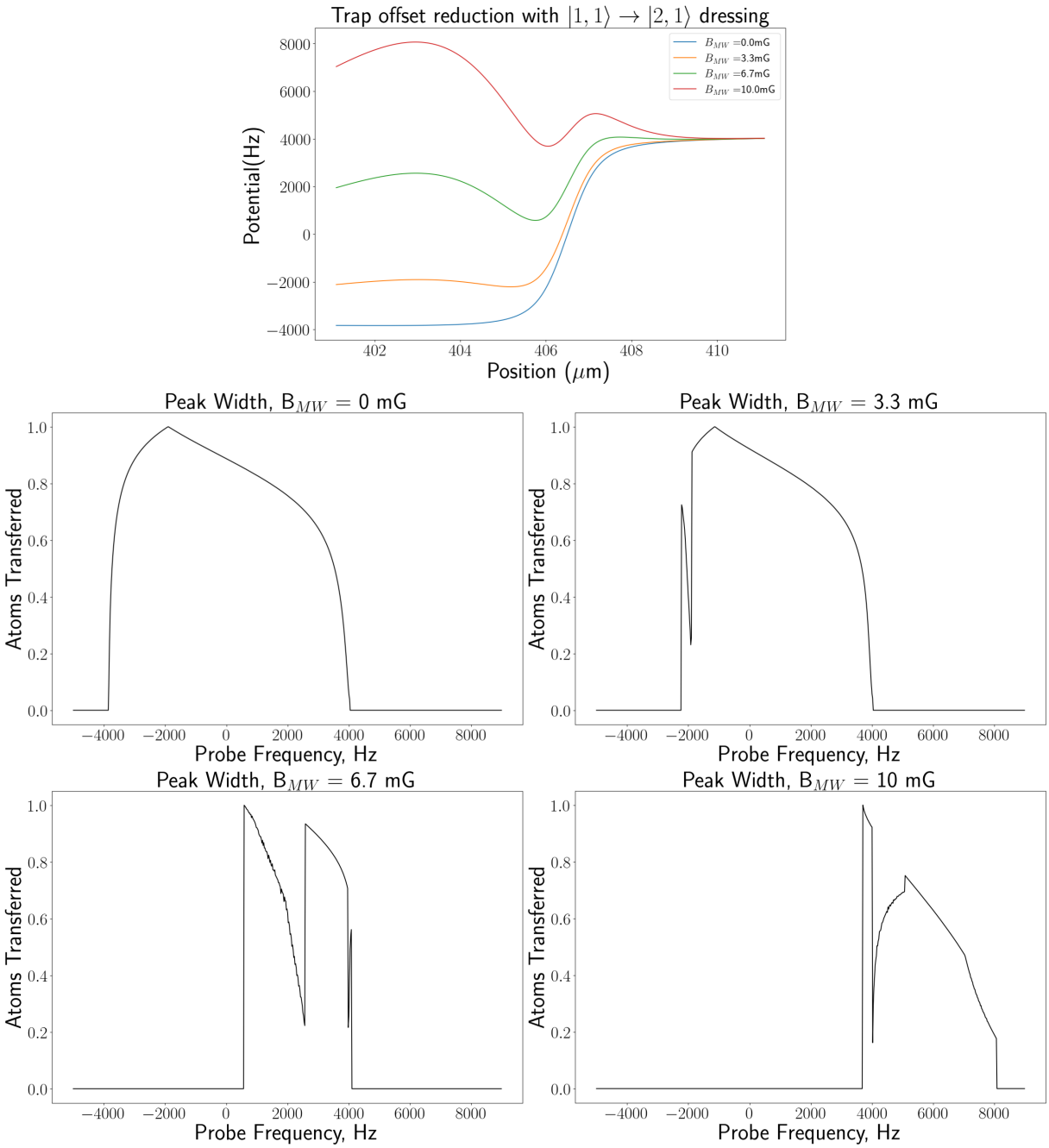

Figure 6.9: Simulated trap offsets (Right), and peak widths (left) for the $|1,-1\rangle \rightarrow |2,1\rangle$ transitions, dressed with the $|1,1\rangle \rightarrow |2,1\rangle$ transition of varying field strengths, with $\Delta = 2$kHz. We begin seeing very strange looking double peaks, with unnaturally sharp features, and jagged edges.

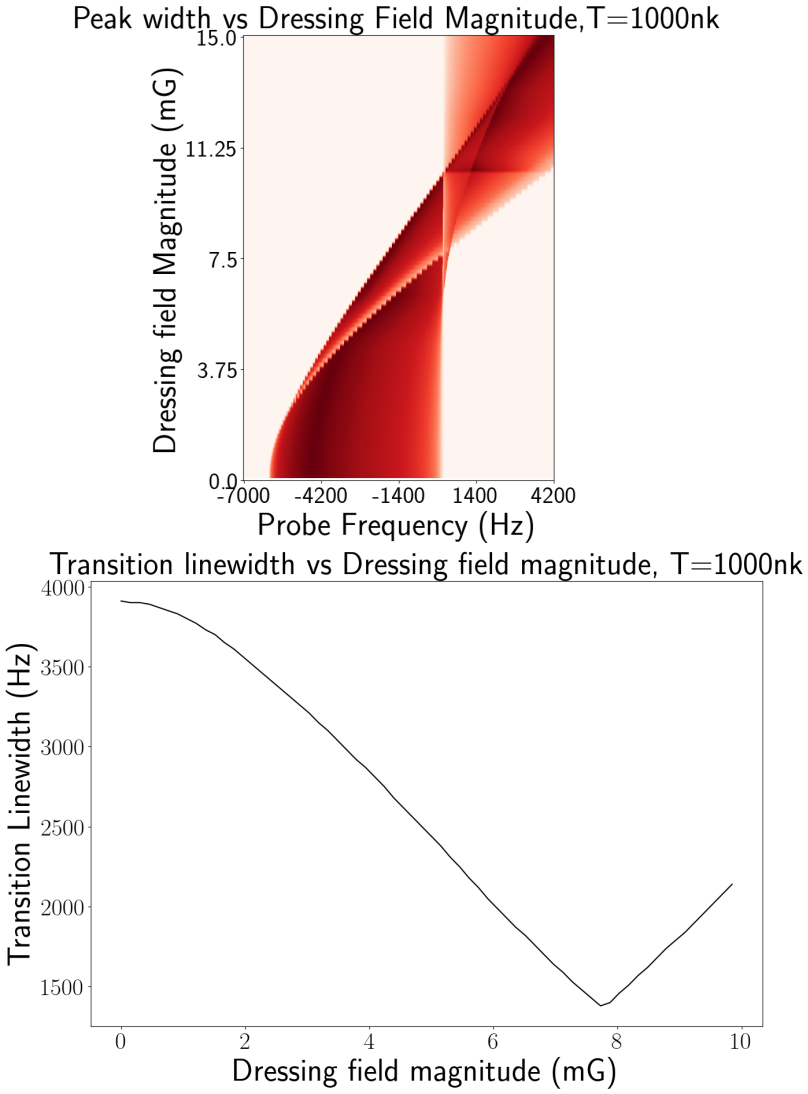

Figure 6.10: Complete scan of MW dressing strengths vs peak width narrowing, dressed on the $|1,1\rangle \rightarrow |2,1\rangle$ transition, $\Delta = 2$kHz. Left : State transfer probability as a function of Probe frequency (x-axis) and Microwave dressing field strength (y-axis), a single y-value slice corresponds to a spectral scan. The red colouring shows the probability of an atom being transferred at that probe frequency, which corresponds to peak height in a spectrum. Right : Calculated peak widths (here we consider any peak height above 1/10 of the maximum height to be part of the transition) as a function of Microwave dressing strength.

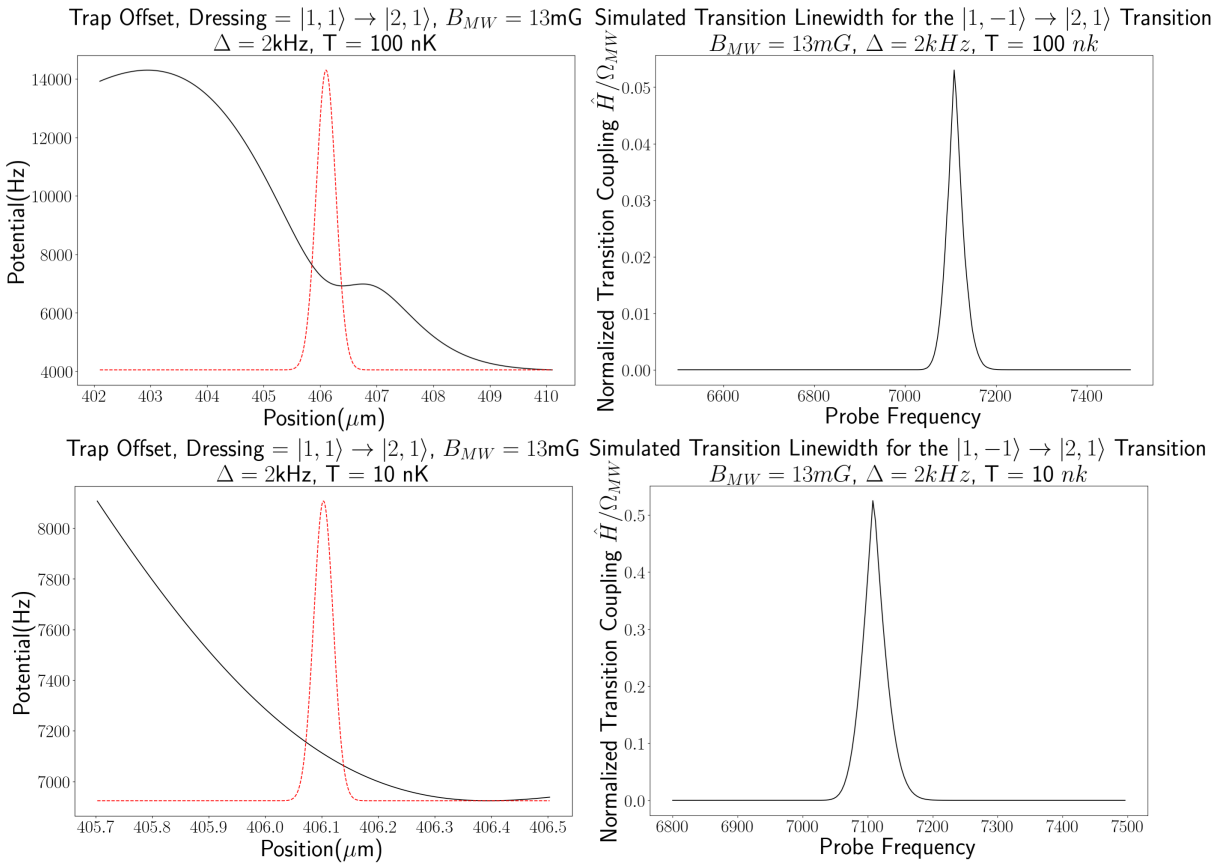

Figure 6.11: Simulated linewidth narrowing of the $|1,-1\rangle \rightarrow |2,1\rangle$ transition, dressed by a MW field blue detuned from the $|1,-1\rangle \rightarrow |2,-1\rangle$ group 3 transition. We see that there is significant linewdith narrowing, which improves as the cloud temperature decreases, down to 100 Hz at 10 nk.

Figure 6.11 shows how applying the same $|1,1\rangle \rightarrow |2,1\rangle$ dressing, with the same detuning, at $B_{MW} = 11$ mG can produce a flattening of the region in the centre of the distribution. For atomic clouds at 100 nk and below, the thermal distribution becomes small enough to sit entirely within the flattened region.

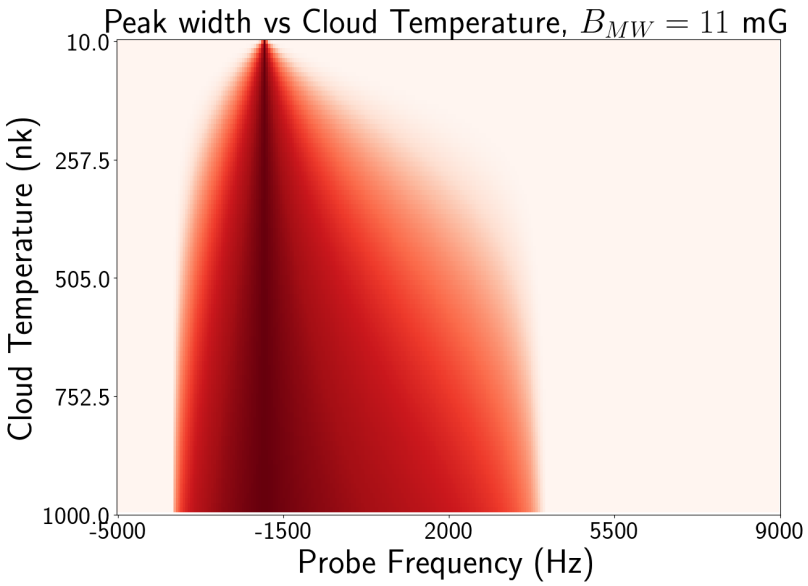

Figure 6.12: Scan of temperature vs. peak width for the trap offset in Figure 6.11. ($B_{MW} = 11$ mG, $\Delta = 2$ kHz.

We expect that the narrowing comes into play at around 500 nk, which gives a rough experimental goal for cooling atom clouds down to, though still out of range for the current experimental setup. Armed with this knowledge we can scan through dressing field strengths, and their respective peak widths to find the optimal narrowing achievable, which we do for $T = 100, 10$ nk.

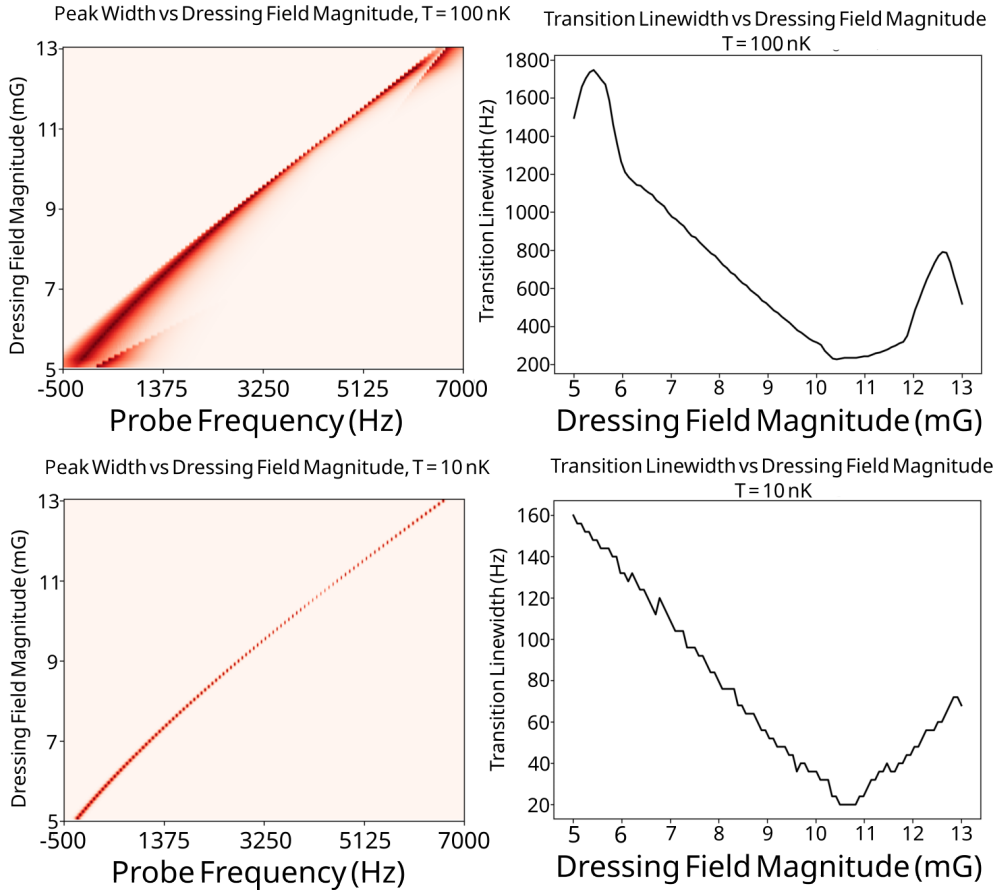

Figure 6.13: Scan of MW dressing field amplitude versus peak widths. Dressed with the $|1,1\rangle \rightarrow |2,1\rangle$ transition, $\Delta = 2$ kHz.

From Figure 6.13 we observe a minimum linewidth at a dressing field amplitude of ≈ 10.5 mG which results in a peak width of ≈ 200Hz for an atomic cloud at 100 nk,and a peak width of $\approx$ 20Hz for the cloud at 10 nk. This shows promise for the process of MW dressing, as 20 Hz brings us well within the coherence range that we would need to start seeing Ramsey fringes in an interferometric sequence.

Multi-Frequency Dressings

Whilst the narrowing of the transition peak down to 20 Hz is a promising start, its requirement of cooling the atomic cloud down to a temperature of 1 nk leaves it as an experimentally unviable option. Instead, we can consider the effects of multiple MW dressing fields applied to the same

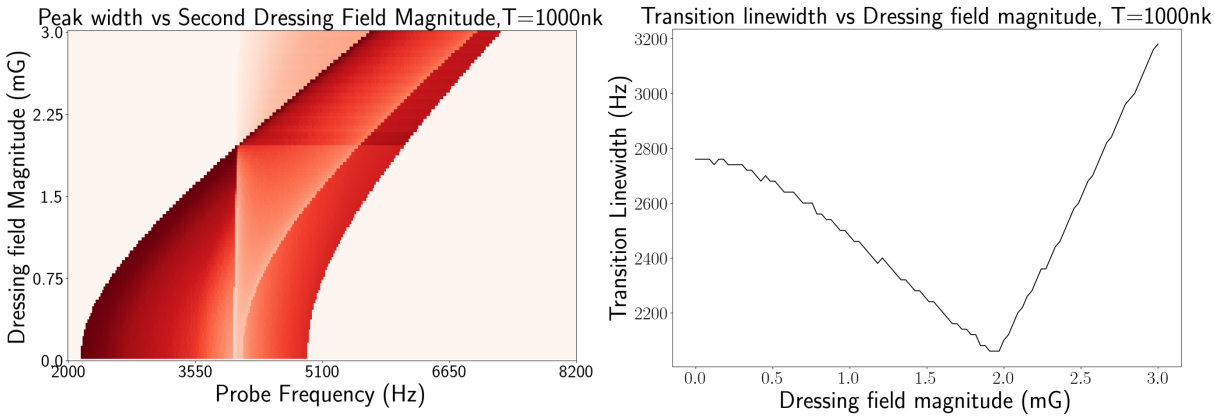

Figure 6.14: Scan of MW dressing field amplitude versus peak widths. Dressed with the $|1,1\rangle \rightarrow |2,1\rangle$ transition, $\Delta = 2$ kHz and the $|1,-1\rangle \rightarrow |2,2\rangle$ transition, $\Delta = 5$ kHz.

atomic cloud. To perform this properly there are a couple of stipulations, firstly in respecting the rotating frame we are limited by the transitions we can choose, as we cannot set up a dressing scheme that couples a loop of energy states, as the shift induced cannot simultaneously shift many coupled energy levels into degeneracy if there is co-dependence between the shifts. Secondly, applying a dressing field to an energy state that is already shifted via another dressing field means that the detuning becomes dependent on the new shifted energy level, this causes a compound effect where the shift of the first field effects the coupling f the second field, which effects the coupling of the first field, and so on. As a result of this, we model a single secondary dressing field that only couples to the undressed state (being the $|1,-1\rangle$ state in our current example.

The second dressing field is able to reduce the linewidth further to the sub 3 kHz regime, and possibly further, with enough searching of the large parameter space. The onloy real concern here is that the field strength of the second dressing field is close to the field strength of the first dressing field, which violates the rotating wave approximation used to generate the modelling of these shifts.

6.2.3 Experimental Results

We perform our experimental testing of microwave dressed potentials in the RF-dressed Ioffe trap, as the well known static field gives us a constant quantisation axis across the entire atomic cloud, meaning that all of the atoms see (roughly) the same polarisation of MW dressing field, which is necessary as even small changes in coupling strength can have drastic effect on the potential shift, and thus the linewidth narrowing. We cool the atoms to around 1 μK, as this is as cold as we can get the cloud before losing contrast on the absorptive imaging. Our initial estimates suggested that the 10 mG of field that we would require to apply dressing strong enough to narrow the linewidth by a substantial amount, was far more than could be produced by our MW antennae. As such, we drive as much current through the MW antennae as possible, attempting to reach maximal coupling. We tested a number of different coupling profiles by detuning from different transition peaks, but found the most success by dressing with the $|1,-1\rangle \rightarrow |2,1\rangle$, $n = -3$ peak. By applying a MW dressing field red-detuned 50 kHz from this transition peak we were able to achieve a narrowing of the clock transition from 4 kHz, down to around 1 kHz, shown in Figure 6.15.

To make absolutely sure that the peak widths that we were measuring were a result of the trap mismatch, and not power broadening, we need to make sure our probe is as weak as possible, whilst still being able to drive the clock transition. We see from Figure 6.16 that at a probe attenuation of +30 dB the peak narrows down to ≈ 4 kHz across. This is substantially less than was predicted from the trap mismatch, and likely owes its origin to the fact that such a weak probe is unable to properly drive atoms across the distribution, and as such we only see the distributions centre.

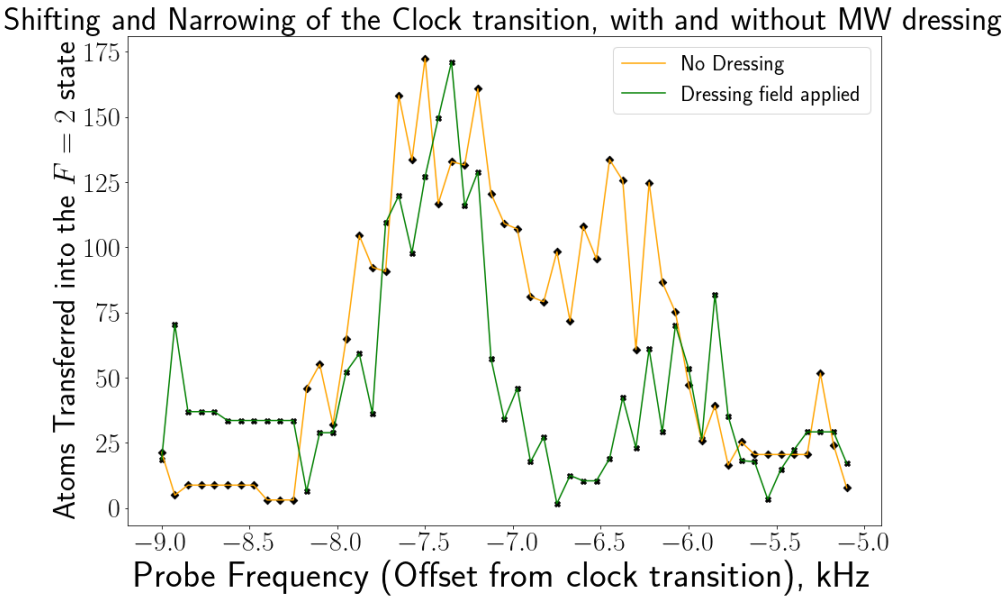

Figure 6.15: Graph illustrating MW dressing experimentally, the clock transition was scanned, once with dressing fields turned off, and once with a dressing field, red detuned from the $n = -3$, $|1, -1\rangle \rightarrow |2, 1\rangle$ transition by $\approx 50kHz$. We see a linewidth reduction down to around 1 kHz

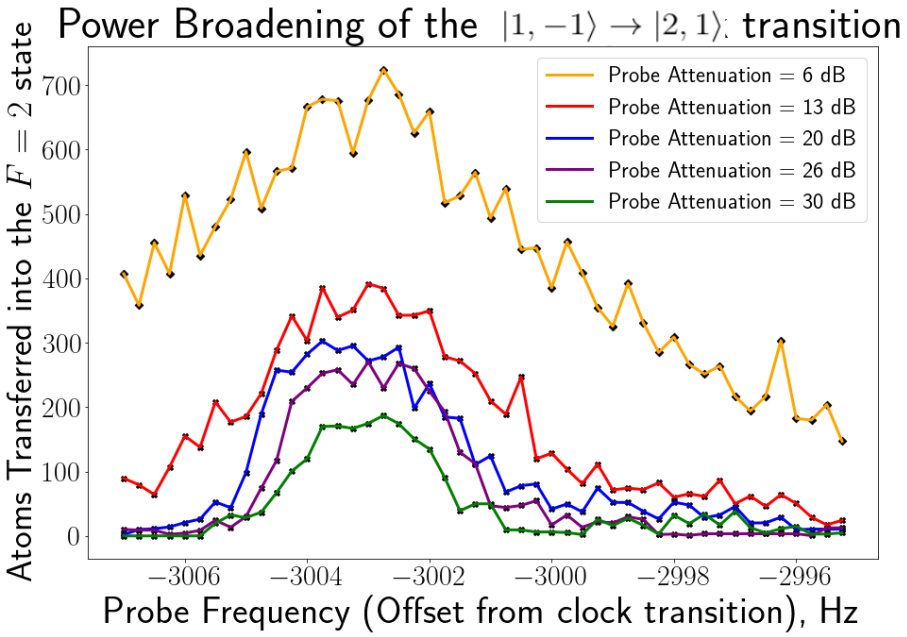

Figure 6.16: Linewidth of the $|1, -1\rangle \rightarrow |2, 1\rangle$ transition, as a function of probe power. Performed by adding physical attenuators in front of the MW antennae

With knowledge of how broad our bare peak is, and a good peak to perform dressing on, we consider the effects of detuning from the peak. We scan the peak widths for different detuning from the $|1,-1\rangle \rightarrow |2,1\rangle$ $n=-3$ transition, where inevitable some of the dressing fields are closer to other peaks than our desired transition, which seems to have little effect, likely due to how poor the coupling of the MW field is to those peaks (see Figure 5.2). When performing this we keep in consideration the adiabaticity of applying the dressing fields, and ramp up the detuning from an extra 50 kHz out. For large detunings, we see the same narrowing down to 2 kHz, but little change when the detuning is lowered, until we reach around 450 kHz detuning from the transition, where the peak begins to shift by 100-200 Hz. These results are shown in Figure 6.17. Noticeably, at very low detunings the peaks is less contrasted from the background, likely due to the dressing field actually driving the transition, and driving atoms in to a non-visible state, rather than dressing the peak. We are able to partially remedy this by ramping from a high detuning to the lower detunings, but the space between transitions (as shown in Figure 5.3

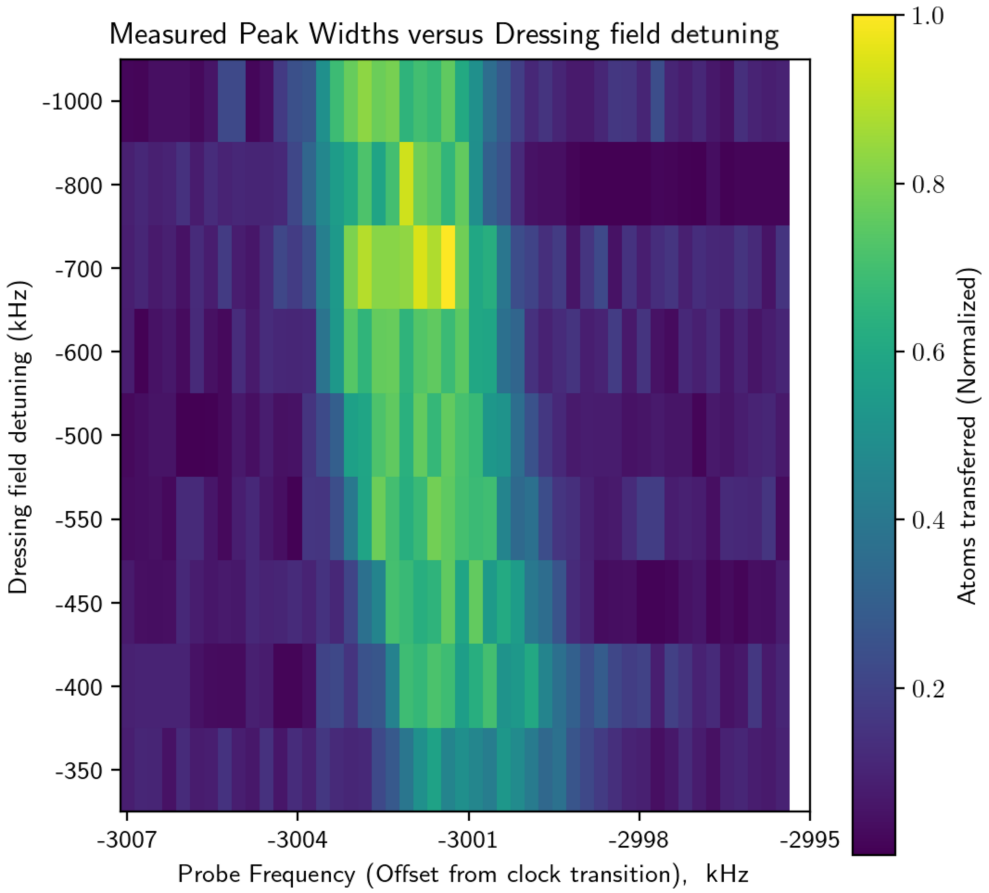

Figure 6.17: Scan of Peak width measured against detuning from the $|1,-1\rangle \rightarrow |2,1\rangle$ $n=-3$ transition. The Y-axis is not linearly scaled.

With confirmation that we see a dressing effect at detunings smaller then $\Delta = 450$ kHz, we then ramp down the detuning to ≈ 50 kHz from the $|1,-1\rangle \rightarrow |2,1\rangle$ $n=-3$ transition peak, for differing attenuation on the dressing field. We expect, from theory to see a peak width reduction from 8 kHz, down to $\approx$ 4 kHz, or a factor of 2 reduction. From the weakest dressing fields we can possible apply, we already see the peak width being reduced by a factor of 2, though low atom number means direct measurement of peak widths is difficult. We observe further shifting of the peaks for increasing dressing field, but a gradual increase in linewidth, and at -12.33 dBm, we see a possible second peak arise, also aligning with the theoretical understanding. From this we can estimate that our MW dressing field has a field that corresponds to 10.5 mG of field (before

consideration of polarisation couplings, meaning the actual field value is at least $\sqrt{2}$ times higher) between -18.5 dBm, and -15.67 dBm.

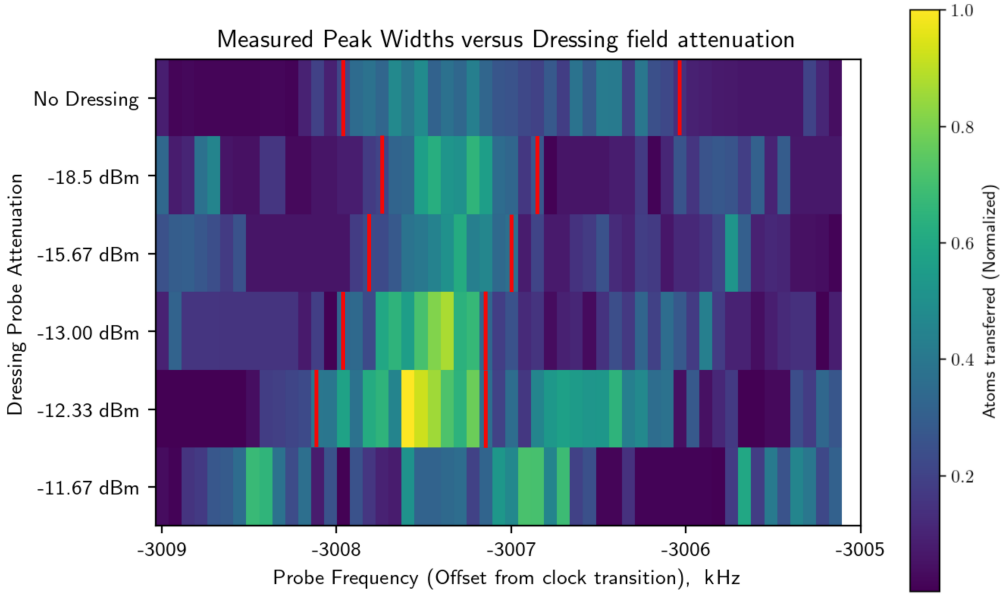

Figure 6.18: Experimental data applying a dressing field red detuned by $\approx$ 50kHz from the $|1,-1\rangle \rightarrow |2,1\rangle$ $n=-3$ transition. Due to low atom numbers, peaks are hard to pick out, and so red lines outline the best guess of peak width

With a significant reduction in peak width achieved through the use of a single dressing field, able to reduce the width of the peak down into the sub kHz range, better than what we expect from theory. This is unexpected, and measuring the temperature of the atomic cloud in the $|1,-1\rangle$ state to be $\approx 1.5\mu$k. We attribute all of these narrower peaks to the weakened probe, that has a measured rabi frequency of $\approx$ 200Hz, meaning a $\frac{\pi}{2}$ pulse is multiple milliseconds. This means that each pulse drives very few atoms into the F=2 manifold. We compare these results with the theoretical description of the shift induced by this.

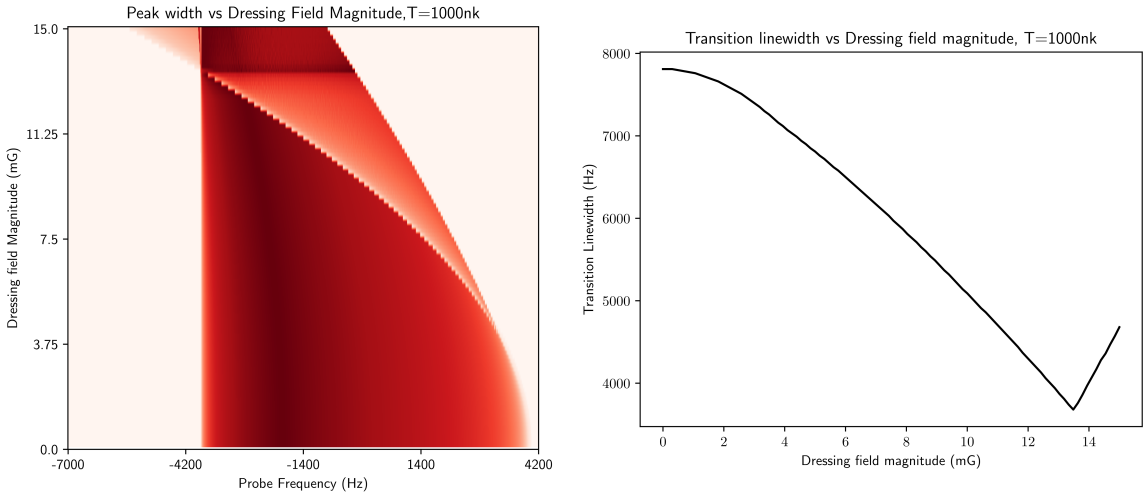

Figure 6.19: Theoretical model of linewidth for the experimental data taken in Figure 6.18. The transition is the $|1,-1\rangle \rightarrow |2,1\rangle$ $n=-3$, red detuned by 50 kHz

The results coincide well between theory and experiment, with a narrowed peak width that is half as wide as the undressed case. We expect to see peak narrowing at ≈ 13.5 mG of σ_- polarised field, meaning we are dressing with at least 19 mG of linear field.

The remaining path the narrow the linewidth lays open somewhat, but is gated by powers, the Rabi frequencies of MW dressing field we reach are already comparable to the estimated Rabi frequencies from the RF dressing field that we employ, in this case the rotating approximation breaks down, and we are essentially performing the parameter search blind. In addition to this, the highest powers of MW dressing fields have the effect of driving the transition. This can be remedied by an adiabatic ramping of the dressing field, but we do not have enough room to do a full ramp, as ramping through other possible transitions (see 5.1) will transfer the atoms on that transition instead. In this we are still limited by the RF dressing field magnitude, as symptom of the geometric design of the atom chip stack (see 3.15).

Chapter 7

Conclusion and Outlook

This thesis has thus presented the progress made on the path to the fully trapped and guided Sagnac interferometer, the updated progress chart in Table 7.1 shows how many of the original goals and objectives have been achieved.

Progress Milestone	Completion
Loading atoms into a MOT	Complete
Transport to the Ringtrap	Complete
Demonstrate RF-Dressed Potentials	Complete
Load the RF-Dressed Ringtrap	Complete
RF-Dressed Transport Scheme	Complete
Multiple second trap Lifetimes	Complete
Demonstrate MW-Dressed potentials	Complete
200ms Coherence time/1Hz Linewidth	Partial
Full Ramsey Sequence	Incomplete
Rotational Interferometry	Incomplete
Signal maximisation and noise reduction	Incomplete

Table 7.1: Updated table of objectives, as of February 2024

We can see that significant progress has been made in advancing along the path towards an operational interferometer, though the interferometric sequence remains unachieved. With this in mind, this chapter will summate these achievements, and then explore the future outlook of the project.

State Dependent Transport

The big breakthrough on this project was the realisation of state dependent transport, the path to a stable RF dressed ringtrap was fraught with difficulties. It turned out that our main issue was with phase noise on the internal clock, but connecting a satellite based clock stabilised the RF signals. We are now able to transport atoms in both the $F = 2$, and $F = 1$ trappable states, at a maximum rotational rate of 5 Hz. The demonstration of this means that the mechanical basis for the fully trapped Sagnac interferometer is complete.

There are a few facets with which to improve the dressed transport system, with most of them owing to increased atom numbers, and reduced cloud temperatures, both of which are mostly solvable through more efficient cooling ramps, and better trapping methods - pre ringtrap. Combined with this, improvements can be made in the depth of the interference fields by increasing the radial RF dressing fields. We see such weak radial dressing fields as our radial dressing coil only produces fields at 17 degrees to the vertical, limiting our horizontal component to $B_{RFchip} \sin(17^\circ)$.

Coherence control

Our second objective, that of extending the coherence time of a superposition to 200 ms, has seen some initial success, with us being able to demonstrate narrowing of the transition linewidth by a factor of 2. This corresponds with raising our expected coherence time up to just under a millisecond. We do run into some problems, however, namely too improve on the linewidth narrowing we expect to make use of either multi-frequency dressing fields, or low temperature narrowing. At the moment both of these options remained out of experimental reach. Double dressing fields remain a experimental difficulty as the frequency mixer used to create the microwave fields (see Figure 4.11 acts in a non-linear manner when creating multiple sidebands, this means that two dressing field, and a probe, will all vary in power when applied, and when ramped through frequencies. Low temperature dressing schemes also require atoms to be cooled to significantly lower temperatures than currently achievable. Both of these issues are solvable with experimental improvements, and as such the future for

MW dressed potentials bringing the peak width down even further is great.

7.1 Outlook

With the progress made on this project, the path to a fully trapped Sagnac interferometer remains promising, yet not without difficulties. This section now looks to the future, detailing the potential improvements to the setup, methodology and theoretical approach, as well as taking a look into the planned future operation of the interferometer.

7.1.1 Design Improvements

Whilst this project, over the past 4 years, has made great strides in the manipulation of ultracold atomic clouds, there is still vast room for improvement, and the desire to do so. Notable is the desire to be able to cool an atomic cloud below $1\mu k$, while retaining a high enough atom number to maintain contrast for absorptive imaging. Another avenue of improvement that we would like to pursue is improving the total microwave coupling capabilities of the setup, be it through better electronic control of the microwave currents, or new antennae models, either way a higher effective rabi frequency will allow us to enter the regime of strong linewidth narrowing that we require for the interferometric sequence.

Atom Chip Redesign

One method of solving for these issues is via updates to the atom chip setup, in which new additions made with the knowledge gained over the past 4 years of progress could lead to great improvements in our ability to manipulate atoms. Chief amongst these is the redesign of the EM-chip to include a large scale Z trap that routes around the ringtrap. This new Ioffe trap would be many times larger than the Ioffe trap formed of the ringtrap lead wires, and as such could load many more atoms. Doing so would allow us to reach even lower temperatures, whilst maintaining a higher atom number for the purposes of absorptive image contrast. Unfortunately, manufacturing issues have delayed the production of this new chip severly, and as such it may be inactive for some time. Another possible alteration

to the chip, that was not implemented on the new chip ordered, but is in string consideration, is the implementation of a planar antennae on the EM chip that makes use of its large, unused gold layer surrounding the conductor structures. This type of antennae would simply require the gold conductive layer be connected to one of the unused conductor pads on the chip, which could then be connected to a microwave precision connector on the outside of the chamber. Whilst not being designed to produce high fields at the desired MW frequency, it has the benefit of being much closer to the atoms than the current MW antennae

Additional Theory

We must also consider the fact that the current experimental results for MW dressings diverge from the theoretical expectations at high MW field values. This is due to our theory relying on a rotating wave approximation that makes the assumption $\Omega_{MW} \ll \Omega_{RF}$, which becomes patently untrue for our experimental data, and seems to be the regime that we must enter to reach further linewidth narrowing. To avoid entering into the realm of endless trial and error, a new theoretical description of the potential shifts in MW dressing schemes must be used. Such a scheme would involve expanding upon the floquet modes that we touched on in Chapter 2, and creating Floquet hamiltonians that consist of Supermatrices containing the fully dressed $\hat{J}$ Hamiltonian, and additional floquet modes, such a Hamiltonian takes the form:

$$\hat{H}_F = \begin{bmatrix} \hat{J} + \omega_{RF} & \Omega_D & 0 \\ \Omega_D & \hat{J} & \Omega_D \\ 0 & \Omega_D & \hat{J} - \omega_{RF} \end{bmatrix} \tag{7.1}$$

Where Ω_D is the coupling chosen between two states, and ω_{RF} is the RF dressing frequency. This hamiltonian can be expanded to multiple floquet modes $\pm 2, 3, 4, \text{etc}\ \omega_{RF}$with expected diminishing effects from additional modes. Such a theory allows us to simulate the effects of a MW coupling field on RF dressed states, without relying on the rotating wave approximation.

7.1.2 Future Operation

Provided we are able to achieve a 200ms coherence time for the superposition, and able to complete a full transport sequence around the ring, without additional heating effects or noise damaging the coherence further, we can look forwards to the ability to perform Sagnac interferometry with the setup. Doing so brings forth a host of new experimental considerations, and challenges, mostly revolving around obtaining the best possible signal from the interferometric sequence, and measuring the rotation with as little uncertainty as possible.

Uncertainty of Measurements

All measurements made experimentally will have an inherent level of uncertainty governed by the individual uncertainties that comprise the total measurement. For atomic Sagnac interferometry we can look to Equation 2.12, and consider the uncertainties associated with m, A, Ω, and $\hbar$ to find our overall uncertainty $\delta\Phi$. As m, and $\hbar$ are obtained from the literature, both assume that the inherent uncertainties are very low, and that there is little we can do to affect those uncertainties anyway, so they are better left ignored. We then consider the uncertainty in the Sagnac phase $\delta\Phi$ as a function of uncertainty in the interferometer area δA, and the uncertainty in the rotation rate $\delta\Omega$, by taking the total differential of $\delta\Phi$:

$$\delta\Phi^2 = \left(\frac{\partial\Phi}{\partial A}\delta A\right)^2 + \left(\frac{\partial\Phi}{\partial\Omega}\delta\Omega\right)^2 \tag{7.2}$$

which can be simplified to:

$$\delta\Phi^2 = \left(\frac{m\Omega}{\hbar}\delta A\right)^2 + \left(\frac{mA}{\hbar}\delta\Omega\right)^2 \tag{7.3}$$

We can see from here that our uncertainty in rotation rate is amplified by the area of the interferometer, which is fixed (based on the size of the ringtrap, and thus the EM chip). The uncertainty is only controllable by our ability to minimise δA, which can be done by decreasing the rotation rate of the interferometer. At first this seems like a counter-intuitive process, as the rotation rate is what we are trying to obtain by measuring the

Sagnac phase. However, we can reverse engineer the problem, by running the interferometry sequence a number of times, and during each one applying a rotation to the device, we can find a rotation that cancels out Ω. This would mean that we measure the external rotation, while keeping the rotation rate of the device to a minimum, reducing measurement uncertainty in the process.

Signal Maximisation : Quantum Squeezing

In quantum mechanics there is an uncertainty tied to measurements of two related quantities that is defined by the commutation of the two operators : $[\hat{A}, \hat{B}] = AB - BA$. This uncertainty is most well known in the Heisenberg uncertainty between position and momentum : $[\hat{x}, \hat{p}_x] = \frac{\hbar}{2}$, or the uncertainty between two spin operators $[\hat{S}_x, \hat{S}_y] = i\hbar\hat{S}_z$. For our interferometer, it is the projection of such spin states onto the bloch sphere that defines our inteferometry sequence, and as such there is an inherent uncertainty in the projection of $\hat{S}_z$ that depends on the uncertainty in the measurement of the superpositional phase (which count as the projections of $\hat{S}_x$ and $\hat{S}_y$). For a cloud of atoms in a superposition, we can write the coherent spin state (CSS) of a spin-half system as [56]:

$$|\theta, \phi\rangle = \bigotimes_{l=1}^{N} \left[\cos\left(\frac{\theta}{2}\right)|-\rangle + \exp(i\phi)\sin\left(\frac{\theta}{2}\right)\right] \tag{7.4}$$

where we take the tensor product of the l-th atom, for N total atoms. We can also define a 'squeezing parameter' ξ from the commutation relation for spin states [52]:

$$\xi^2 = \frac{2(\Delta S_\alpha)^2}{|\langle S_\gamma\rangle|} \tag{7.5}$$

where α and γ are orthogonal directions that the spin can be broadcast to. This squeezing parameter can be shown to be:

$$\xi^2 = \left|\frac{\sin(\theta)}{\cos(\phi)}\right| \tag{7.6}$$

The purpose of the squeezing parameter is to measure how much more accurately the squeezing allows one to measure a given state. For a spin

half particle, the expected measurement uncertainty for the coherent spin state, and the squeezed state can be expressed as:

$$\begin{aligned} \Delta\Phi_{CSS} &= \frac{\Delta J_y}{|\langle Jz\rangle|} = \frac{1}{\sqrt{N}}, \\ \Delta\Phi_{SSS} &= \frac{\xi}{\sqrt{N}} \end{aligned} \tag{7.7}$$

We expect a cloud in a coherent spin state to have a binomial distribution of states, whereas the squeezed state becomes sub binomial. one way of spin squeezing a system is applying a method called one axis-twisting. By introducing a rotation operator about the z axis, defined as $\hat{U} = \exp(-itF(S_z))$ the quasiprobability function can be spread about the bloch sphere, reducing is component in one axis. If done in the correct way, this canreduce the uncertainty in a measurement of S_z, allowing for better interferometry. This process has been shown to work in a variety of experimental settings, making it an ideal candidate for improving the operation of the interferometer.

Appendix A

Principal Component Analysis

This project relies very heavily on the Principal of absorptive imaging to make measurements on atomic clouds. For the most part this is a fine process, as the ability to remove atoms via AC magnetic field pulses allows for spectroscopy that can be directly read out through this imaging process. However, as we near the end of each experimental cycle, atom numbers drop down into the low thousands, which drastically lowers the Optical density of the cloud. As a direct result, the contrast for imaging and spectroscopic purposes reduces, and the features on such measurements become hard to discern amongst measurement noise. This is especially true for atoms in the ioffe and ringtrap, as vibrational noise means that the EM chip structure is especially noticeable.

To combat this, we make use of Principal component analysis to analyse the light and dark images to generate the 'perfect' background image corresponding to each atoms image. To do this we must be able to construct a set of images that correspond to common noise in the images. We first calculate the covariance matrix $\mathcal{C}$ for all images:

$$\mathcal{C} = \mathbf{cov}(\mathbf{light\text{-}dark}) \tag{A.1}$$

This creates an $N \times N$ array, with each off diagonal element corresponding to the covariance between two images(i.e.the $(1, 2)$ element corresponds to the variance between the 1st and 2nd images). We are then interested in generating the eigenvector of such a matrix, as this vector denotes image components that minimise the covariance matrix. The components

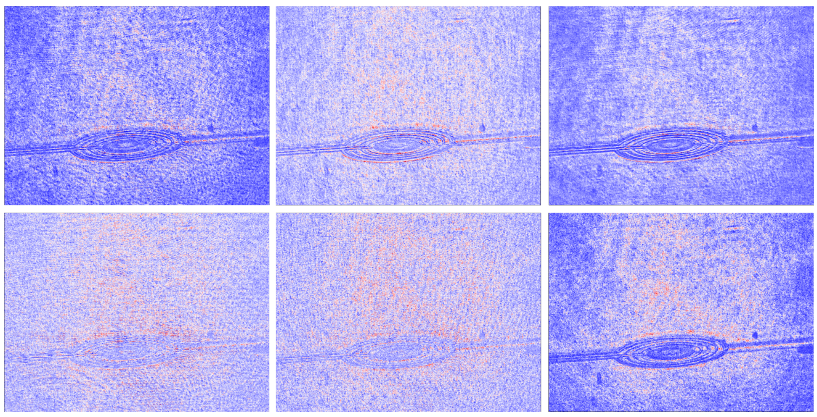

Figure A.1: First 6 Principal components, we clearly see the EM coil structure in each one., along with differing noise in fringes and camera spots

of this eigenvector, or eigenimage, denote components of the respective original images that make up an image that minimises covariance in the background images. The corresponding eigenvalues tell us how 'much' a given eigenimage makes up in the background. Written empirically, a given eigenimage $\mathcal{I}$ is defined as:

$$\mathcal{C}\,|\mathcal{I}\rangle = \epsilon\,|\mathcal{I}\rangle \tag{A.2}$$

We can then project the atoms image, $\mathcal{A}$, along the eigenimage axis, to calculate a background that matches the noise in the atoms image. We must fine tune exactly how many eigenimages to consider in our background image generation. Too few and we don't correctly account for all the background noise, but too many and we begin to wash out specific noise features (as the sum of all eigenimages is just the mean image). Subtracting this from the atoms image then grants us our total image, $\mathcal{T}$:

$$\mathcal{T}_n = \mathcal{A}_n - \sum_{i=1}^{k} (\mathcal{A}_n \cdot \mathcal{I}_i) \times \mathcal{I}_i, \tag{A.3}$$

where k is the amount of eigenimages we wish to use to reconstruct our background. We can calibrate this by looking at the associated eigenvalues, and only picking eigenimages with large associated.

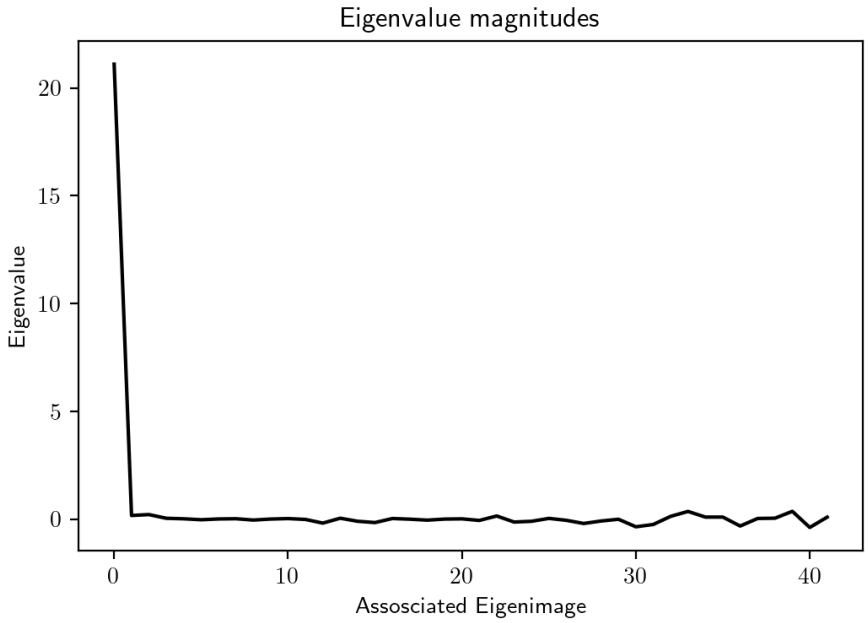

Figure A.2: Graph of eigenimage values, in descending order, for this image, we only really need the first eigenimage, as it has a magnitude much greater than any others.

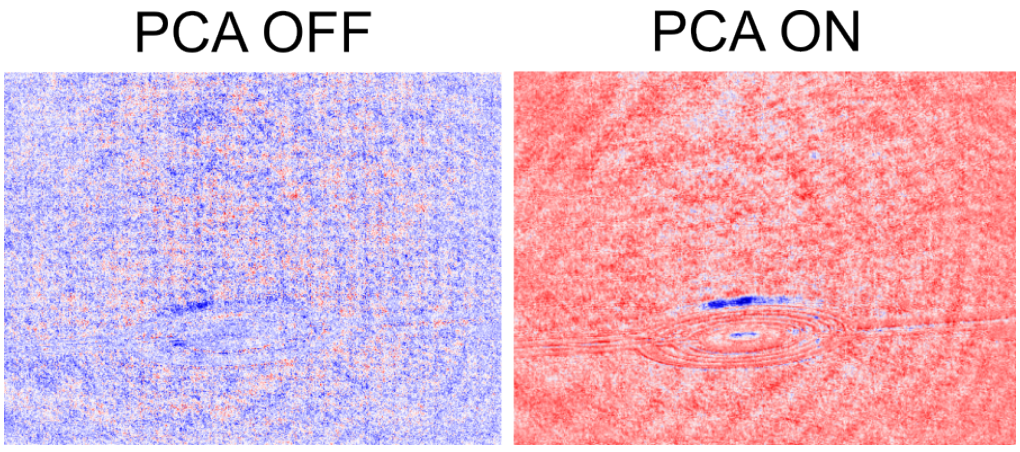

Figure A.3: Absorption imaging of atoms, from figure 3.18, compared with PCA to de-noise the image, and without.

Bibliography

[1] B. P. Abbott et al. "GW151226: Observation of Gravitational Waves from a 22-Solar-Mass Binary Black Hole Coalescence". In: *Physical Review Letters* 116.24 (June 15, 2016), p. 241103. ISSN: 0031-9007, 1079-7114. DOI: 10.1103/PhysRevLett.116.241103. URL: https://link.aps.org/doi/10.1103/PhysRevLett.116.241103 (visited on 08/27/2025).

[2] S. Abend et al. "Atom-Chip Fountain Gravimeter". In: *Physical Review Letters* 117.20 (Nov. 11, 2016), p. 203003. ISSN: 0031-9007, 1079-7114. DOI: 10.1103/PhysRevLett.117.203003. URL: https://link.aps.org/doi/10.1103/PhysRevLett.117.203003 (visited on 11/22/2024).

[3] C.S. Adams, O. Carnal, and J. Mlynek. "Atom Interferometry". In: *Advances In Atomic, Molecular, and Optical Physics*. Vol. 34. Elsevier, 1994, pp. 1–33. ISBN: 978-0-12-003834-3. DOI: 10.1016/S1049-250X(08)60073-7. URL: https://linkinghub.elsevier.com/retrieve/pii/S1049250X08600737 (visited on 11/22/2024).

[4] Luigi Amico et al. "Colloquium: Atomtronic circuits: From many-body physics to quantum technologies". In: *Rev. Mod. Phys.* 94.4 (Nov. 2022). Publisher: American Physical Society, p. 041001. DOI: 10.1103/RevModPhys.94.041001. URL: https://link.aps.org/doi/10.1103/RevModPhys.94.041001.

[5] M. H. Anderson et al. "Observation of Bose-Einstein Condensation in a Dilute Atomic Vapor". In: *Science* 269.5221 (1995). Publisher: American Association for the Advancement of Science, pp. 198–201. ISSN: 00368075, 10959203. URL: http://www.jstor.org/stable/2888436 (visited on 11/21/2024).

[6] Vilius Atkocius. "State-dependent RF-Dressed Ring traps for Sagnac Interferometry". PhD thesis. 2024.

[7] I. Barb et al. "Creating Ioffe-Pritchard micro-traps from permanent magnetic film with in-plane magnetization". In: *The European Physical Journal D* 35.1 (Aug. 2005), pp. 75–79. ISSN: 1434-6060, 1434-6079. DOI: 10.1140/epjd/e2005-00055-3. URL: http://link.springer.com/10.1140/epjd/e2005-00055-3 (visited on 11/30/2024).

[8] Brynle Barrett et al. "The Sagnac effect: 20 years of development in matter-wave interferometry". In: *Comptes Rendus. Physique* 15.10 (Nov. 12, 2014), pp. 875–883. ISSN: 1878-1535. DOI: 10.1016/j.crhy.2014.10.009. URL: https://comptes-rendus.academie-sciences.fr/physique/articles/10.1016/j.crhy.2014.10.009/ (visited on 11/30/2024).

[9] Dobroslawa Bartoszek-Bober, Roman Panas, and Tomasz Kawalec. "Magnetic trapping on an atom chip". In: *Photonics Letters of Poland* 5.3 (Oct. 1, 2013), pp. 109–111. ISSN: 2080-2242. DOI: 10.4302/plp.2013.3.10. URL: http://photonics.pl/PLP/index.php/letters/article/view/442 (visited on 11/30/2024).

[10] Roberto Bassani. "Earnshaw (1805–1888) and Passive Magnetic Levitation". In: *Meccanica* 41.4 (Aug. 2006), pp. 375–389. ISSN: 0025-6455, 1572-9648. DOI: 10.1007/s11012-005-4503-x. URL: http://link.springer.com/10.1007/s11012-005-4503-x (visited on 11/30/2024).

[11] T. Berrada et al. "Integrated Mach–Zehnder interferometer for Bose–Einstein condensates". In: *Nature Communications* 4.1 (June 27, 2013), p. 2077. ISSN: 2041-1723. DOI: 10.1038/ncomms3077. URL: https://www.nature.com/articles/ncomms3077 (visited on 11/30/2024).

[12] Thomas Bishop. "A guided matter-wave Sagnac interferometer, Thesis". PhD thesis. 2019.

[13] Kai Bongs and Klaus Sengstock. "Physics with coherent matter waves". In: *Reports on Progress in Physics* 67.6 (June 1, 2004), pp. 907–963. ISSN: 0034-4885, 1361-6633. DOI: 10.1088/0034-4885/67/6/R03.

URL: https://iopscience.iop.org/article/10.1088/0034-4885/67/6/R03 (visited on 11/30/2024).

[14] G. Breit and I. I. Rabi. "Measurement of Nuclear Spin". In: *Phys. Rev.* 38.11 (Dec. 1931). Publisher: American Physical Society, pp. 2082–2083. DOI: 10.1103/PhysRev.38.2082.2. URL: https://link.aps.org/doi/10.1103/PhysRev.38.2082.2.

[15] D. M. Brink and C. V. Sukumar. "Majorana spin-flip transitions in a magnetic trap". In: *Physical Review A* 74.3 (Sept. 11, 2006), p. 035401. ISSN: 1050-2947, 1094-1622. DOI: 10.1103/PhysRevA.74.035401. URL: https://link.aps.org/doi/10.1103/PhysRevA.74.035401 (visited on 08/27/2025).

[16] Louis De Broglie. "XXXV. *A tentative theory of light quanta*". In: *The London, Edinburgh, and Dublin Philosophical Magazine and Journal of Science* 47.278 (Feb. 1924), pp. 446–458. ISSN: 1941-5982, 1941-5990. DOI: 10.1080/14786442408634378. URL: https://www.tandfonline.com/doi/full/10.1080/14786442408634378 (visited on 11/22/2024).

[17] F. Bylicki et al. "Studies of the Hydrodynamic Properties of Bose-Einstein Condensate of^{87} Rb Atoms in a Magnetic Trap". In: *Acta Physica Polonica A* 113.2 (Feb. 2008), pp. 691–705. ISSN: 0587-4246, 1898-794X. DOI: 10.12693/APhysPolA.113.691. URL: http://przyrbwn.icm.edu.pl/APP/PDF/113/a113z208.pdf (visited on 11/30/2024).

[18] B. Canuel et al. "Exploring gravity with the MIGA large scale atom interferometer". In: *Scientific Reports* 8.1 (Sept. 14, 2018), p. 14064. ISSN: 2045-2322. DOI: 10.1038/s41598-018-32165-z. URL: https://www.nature.com/articles/s41598-018-32165-z (visited on 11/30/2024).

[19] Sheng-wey Chiow et al. "102 hbark Large Area Atom Interferometers". In: *Phys. Rev. Lett.* 107.13 (Sept. 2011). Publisher: American Physical Society, p. 130403. DOI: 10.1103/PhysRevLett.107.130403. URL: https://link.aps.org/doi/10.1103/PhysRevLett.107.130403.

[20] Pierre Cladé et al. "Determination of the Fine Structure Constant Based on Bloch Oscillations of Ultracold Atoms in a Vertical Optical Lattice". In: *Physical Review Letters* 96.3 (Jan. 23, 2006), p. 033001. ISSN: 0031-9007, 1079-7114. DOI: 10.1103/PhysRevLett.96.033001. URL: https://link.aps.org/doi/10.1103/PhysRevLett.96.033001 (visited on 11/30/2024).

[21] R. Colella, A. W. Overhauser, and S. A. Werner. "Observation of Gravitationally Induced Quantum Interference". In: *Physical Review Letters* 34.23 (June 9, 1975), pp. 1472–1474. ISSN: 0031-9007. DOI: 10.1103/PhysRevLett.34.1472. URL: https://link.aps.org/doi/10.1103/PhysRevLett.34.1472 (visited on 11/22/2024).

[22] Michael W. Davidson. *Robert Hooke (1635-1703)*. Nov. 13, 2015.

[23] K. B. Davis, M. -O. Mewes, and W. Ketterle. "An analytical model for evaporative cooling of atoms". In: *Applied Physics B Laser and Optics* 60.2 (1995), pp. 155–159. ISSN: 0946-2171, 1432-0649. DOI: 10.1007/BF01135857. URL: http://link.springer.com/10.1007/BF01135857 (visited on 11/30/2024).

[24] C. Davisson and L. H. Germer. "Diffraction of Electrons by a Crystal of Nickel". In: *Physical Review* 30.6 (Dec. 1, 1927), pp. 705–740. ISSN: 0031-899X. DOI: 10.1103/PhysRev.30.705. URL: https://link.aps.org/doi/10.1103/PhysRev.30.705 (visited on 11/22/2024).

[25] Rogerio De Sousa. "Electron Spin as a Spectrometer of Nuclear-Spin Noise and Other Fluctuations". In: *Electron Spin Resonance and Related Phenomena in Low-Dimensional Structures*. Ed. by Marco Fanciulli. Red. by Claus E. Ascheron and Adelheid H. Duhm. Vol. 115. Series Title: Topics in Applied Physics. Berlin, Heidelberg: Springer Berlin Heidelberg, 2009, pp. 183–220. ISBN: 978-3-540-79364-9 978-3-540-79365-6. DOI: 10.1007/978-3-540-79365-6_10. URL: http://link.springer.com/10.1007/978-3-540-79365-6_10 (visited on 11/30/2024).

[26] Savas Dimopoulos et al. "Gravitational wave detection with atom interferometry". In: *Physics Letters B* 678.1 (July 2009), pp. 37–40. ISSN: 03702693. DOI: 10.1016/j.physletb.2009.06.011. URL:

https://linkinghub.elsevier.com/retrieve/pii/S0370269309006844 (visited on 08/27/2025).

[27] Yan-Xiong Du et al. "Experimental realization of stimulated Raman shortcut-to-adiabatic passage with cold atoms". In: *Nature Communications* 7.1 (Aug. 11, 2016), p. 12479. ISSN: 2041-1723. DOI: 10.1038/ncomms12479. URL: https://www.nature.com/articles/ncomms12479 (visited on 11/22/2024).

[28] R Kollengode Easwaran et al. "RF spectroscopy in a resonant RF-dressed trap". In: *Journal of Physics B: Atomic, Molecular and Optical Physics* 43.6 (Mar. 28, 2010), p. 065302. ISSN: 0953-4075, 1361-6455. DOI: 10.1088/0953-4075/43/6/065302. URL: https://iopscience.iop.org/article/10.1088/0953-4075/43/6/065302 (visited on 08/27/2025).

[29] A. Einstein. "Über einen die Erzeugung und Verwandlung des Lichtes betreffenden heuristischen Gesichtspunkt". In: *Annalen der Physik* 322.6 (Jan. 1905), pp. 132–148. ISSN: 0003-3804, 1521-3889. DOI: 10.1002/andp.19053220607. URL: https://onlinelibrary.wiley.com/doi/10.1002/andp.19053220607 (visited on 11/22/2024).

[30] I. Estermann and O. Stern. "Beugung von Molekularstrahlen". In: *Zeitschrift fr Physik* 61.1 (Jan. 1930), pp. 95–125. ISSN: 1434-6001, 1434-601X. DOI: 10.1007/BF01340293. URL: http://link.springer.com/10.1007/BF01340293 (visited on 11/22/2024).

[31] JianCheng Fang and Jie Qin. "Advances in Atomic Gyroscopes: A View from Inertial Navigation Applications". In: *Sensors* 12.5 (May 11, 2012), pp. 6331–6346. ISSN: 1424-8220. DOI: 10.3390/s120506331. URL: https://www.mdpi.com/1424-8220/12/5/6331 (visited on 11/22/2024).

[32] R.P. Feynman, R.B. Leighton, and M.L. Sands. *The Feynman Lectures on Physics*. Addison-Wesley, 1989. ISBN: 978-0-201-02115-8. URL: https://books.google.co.uk/books?id=P6SSRAAACAAJ.

[33] Fausto Fiorillo. *Measurement and characterization of magnetic materials*. Elsevier series in electromagnetism. Amsterdam: Elsevier Academic Press, 2004. 1 p. ISBN: 978-0-12-257251-7 978-0-08-052892-2.

[34] Christopher J. Foot. *Atomic physics*. Repr. (twice with corr.) Oxford master series in physics Atomic, optical, and laser physics 7. Oxford: Oxford Univ. Press, 2011. 331 pp. ISBN: 978-0-19-850695-9 978-0-19-850696-6.

[35] Bethany Foxon. *Foxon, Bethany (2021) Quantum coherence control for radio-frequency dressed cold atom systems. PhD thesis, University of Nottingham.*

[36] G. Gauthier et al. "Direct imaging of a digital-micromirror device for configurable microscopic optical potentials". In: *Optica* 3.10 (Oct. 20, 2016), p. 1136. ISSN: 2334-2536. DOI: 10.1364/OPTICA.3.001136. URL: https://opg.optica.org/abstract.cfm?URI=optica-3-10-1136 (visited on 11/30/2024).

[37] Fabio Gentile. "Towards an atomic Sagnac interferometer with full dynamical control of atoms in ring waveguides". PhD thesis. Aug. 2019.

[38] Fabio Gentile et al. "Ring-shaped atom-trap lattices using multipole dressing fields". In: *AVS Quantum Science* 7.1 (Mar. 1, 2025), p. 013201. ISSN: 2639-0213. DOI: 10.1116/5.0241505. URL: https://pubs.aip.org/aqs/article/7/1/013201/3340099/Ring-shaped-atom-trap-lattices-using-multipole (visited on 08/27/2025).

[39] S. Gov, S. Shtrikman, and H. Thomas. "Magnetic trapping of neutral particles: Classical and quantum-mechanical study of a Ioffe–Pritchard type trap". In: *Journal of Applied Physics* 87.8 (Apr. 15, 2000), pp. 3989–3998. ISSN: 0021-8979, 1089-7550. DOI: 10.1063/1.372444. URL: https://pubs.aip.org/jap/article/87/8/3989/490916/Magnetic-trapping-of-neutral-particles-Classical (visited on 08/27/2025).

[40] Peter W. Graham et al. "New Method for Gravitational Wave Detection with Atomic Sensors". In: *Physical Review Letters* 110.17 (Apr. 25, 2013), p. 171102. ISSN: 0031-9007, 1079-7114. DOI: 10.1103/PhysRevLett.110.171102. URL: https://link.aps.org/doi/10.1103/PhysRevLett.110.171102 (visited on 11/30/2024).

[41] Rudolf Grimm, Matthias Weidemüller, and Yurii B. Ovchinnikov. "Optical Dipole Traps for Neutral Atoms". In: *Advances In Atomic, Molecular, and Optical Physics*. Vol. 42. Elsevier, 2000, pp. 95–170. ISBN: 978-0-12-003842-8. DOI: 10.1016/S1049-250X(08)60186-X. URL: https://linkinghub.elsevier.com/retrieve/pii/S1049250X0860186X (visited on 08/27/2025).

[42] T L Gustavson, A Landragin, and M A Kasevich. "Rotation sensing with a dual atom-interferometer Sagnac gyroscope". In: *Classical and Quantum Gravity* 17.12 (June 21, 2000), pp. 2385–2398. ISSN: 0264-9381, 1361-6382. DOI: 10.1088/0264-9381/17/12/311. URL: https://iopscience.iop.org/article/10.1088/0264-9381/17/12/311 (visited on 11/22/2024).

[43] T. L. Gustavson, P. Bouyer, and M. A. Kasevich. "Precision Rotation Measurements with an Atom Interferometer Gyroscope". In: *Physical Review Letters* 78.11 (Mar. 17, 1997), pp. 2046–2049. ISSN: 0031-9007, 1079-7114. DOI: 10.1103/PhysRevLett.78.2046. URL: https://link.aps.org/doi/10.1103/PhysRevLett.78.2046 (visited on 11/22/2024).

[44] J. C. Hafele and Richard E. Keating. "Around-the-World Atomic Clocks: Predicted Relativistic Time Gains". In: *Science* 177.4044 (1972). Publisher: American Association for the Advancement of Science, pp. 166–168. ISSN: 00368075, 10959203. URL: http://www.jstor.org/stable/1734833 (visited on 11/21/2024).

[45] S. Hofferberth et al. "Radiofrequency-dressed-state potentials for neutral atoms". In: *Nature Physics* 2.10 (Oct. 2006), pp. 710–716. ISSN: 1745-2473, 1745-2481. DOI: 10.1038/nphys420. URL: https://www.nature.com/articles/nphys420 (visited on 11/22/2024).

[46] Jason M. Hogan et al. "An atomic gravitational wave interferometric sensor in low earth orbit (AGIS-LEO)". In: *General Relativity and Gravitation* 43.7 (July 2011), pp. 1953–2009. ISSN: 0001-7701, 1572-9532. DOI: 10.1007/s10714-011-1182-x. URL: http://link.springer.com/10.1007/s10714-011-1182-x (visited on 11/30/2024).

[47] Christiaan Huygens. *Traité de la Lumière: Où sont expliquées les causes de ce qui luy arrive dans la reflexion & dans la refraction.* 1690.

[48] "I. The Bakerian Lecture. Experiments and calculations relative to physical optics". In: *Philosophical Transactions of the Royal Society of London* 94 (Dec. 31, 1804), pp. 1–16. ISSN: 0261-0523, 2053-9223. DOI: 10.1098/rstl.1804.0001. URL: https://royalsocietypublishing.org/doi/10.1098/rstl.1804.0001 (visited on 11/22/2024).

[49] Sindhu Jammi et al. "Dispersive detection of radio-frequency-dressed states". In: *Phys. Rev. A* 97.4 (Apr. 2018). Publisher: American Physical Society, p. 043416. DOI: 10.1103/PhysRevA.97.043416. URL: https://link.aps.org/doi/10.1103/PhysRevA.97.043416.

[50] Jamie Johnson. "Atom-Chip Designs for a Trapped and Guided Sagnac Interferometer". PhD thesis. 2021.

[51] Mark Keil et al. "Stern-Gerlach Interferometry with the Atom Chip". In: *Molecular Beams in Physics and Chemistry*. Ed. by Bretislav Friedrich and Horst Schmidt-Böcking. Cham: Springer International Publishing, 2021, pp. 263–301. ISBN: 978-3-030-63962-4 978-3-030-63963-1. DOI: 10.1007/978-3-030-63963-1_14. URL: https://link.springer.com/10.1007/978-3-030-63963-1_14 (visited on 08/27/2025).

[52] Masahiro Kitagawa and Masahito Ueda. "Squeezed spin states". In: *Physical Review A* 47.6 (June 1, 1993), pp. 5138–5143. ISSN: 1050-2947, 1094-1622. DOI: 10.1103/PhysRevA.47.5138. URL: https://link.aps.org/doi/10.1103/PhysRevA.47.5138 (visited on 11/22/2024).

[53] Maike D. Lachmann et al. "Ultracold atom interferometry in space". In: *Nature Communications* 12.1 (Feb. 26, 2021), p. 1317. ISSN: 2041-1723. DOI: 10.1038/s41467-021-21628-z. URL: https://www.nature.com/articles/s41467-021-21628-z (visited on 11/22/2024).

[54] V. S. Letokhov, V. G. Minogin, and B. D. Pavlik. "Cooling and capture of atoms and molecules by a resonant light field". In: *Soviet Journal of Experimental and Theoretical Physics* 45 (Apr. 1977), p. 698.

[55] Müller H. "Quantum mechanics, matter waves, and moving clocks". In: *Proceedings of the International School of Physics “Enrico Fermi”* 188 (Atom Interferometry 2014), pp. 339–418. ISSN: 0074-784X. DOI: 10.3254/978-1-61499-448-0-339. URL: https://doi.org/10.3254/978-1-61499-448-0-339 (visited on 08/27/2025).

[56] Jian Ma et al. "Quantum spin squeezing". In: *Physics Reports* 509.2 (Dec. 2011), pp. 89–165. ISSN: 03701573. DOI: 10.1016/j.physrep.2011.08.003. URL: https://linkinghub.elsevier.com/retrieve/pii/S0370157311002201 (visited on 08/27/2025).

[57] J.C. Maxwell. "On physical lines of force". In: *Philosophical Magazine* 90 (sup1 Feb. 2010), pp. 11–23. ISSN: 1478-6435, 1478-6443. DOI: 10.1080/14786431003659180. URL: http://www.tandfonline.com/doi/abs/10.1080/14786431003659180 (visited on 11/22/2024).

[58] G. D. McDonald et al. "Optically guided linear Mach-Zehnder atom interferometer". In: *Phys. Rev. A* 87.1 (Jan. 2013). Publisher: American Physical Society, p. 013632. DOI: 10.1103/PhysRevA.87.013632. URL: https://link.aps.org/doi/10.1103/PhysRevA.87.013632.

[59] Zhi-Xin Meng et al. "Closed-loop dual-atom-interferometer inertial sensor with continuous cold atomic beams". In: *Physical Review Applied* 21.3 (Mar. 22, 2024), p. 034050. ISSN: 2331-7019. DOI: 10.1103/PhysRevApplied.21.034050. URL: https://link.aps.org/doi/10.1103/PhysRevApplied.21.034050 (visited on 08/27/2025).

[60] Albert Messiah. *Quantum mechanics: two volumes bound as one*. Garden City, New York: Dover Publications, Inc, 2020. 1136 pp. ISBN: 978-0-486-78455-7.

[61] Harold J. Metcalf and Peter Van Der Straten. *Laser Cooling and Trapping*. Red. by R. Stephen Berry et al. Graduate Texts in Contemporary Physics. New York, NY: Springer New York, 1999. ISBN: 978-0-387-98728-6 978-1-4612-1470-0. DOI: 10.1007/978-1-4612-1470-0. URL: http://link.springer.com/10.1007/978-1-4612-1470-0 (visited on 11/22/2024).

[62] A. A. Michelson and E. W. Morley. "On the relative motion of the Earth and the luminiferous ether". In: *American Journal of Science* s3-34.203 (Nov. 1, 1887), pp. 333–345. ISSN: 0002-9599. DOI: 10.2475/ajs.s3-34.203.333. URL: https://ajsonline.org/article/62505 (visited on 11/22/2024).

[63] O. Morizot et al. "Influence of the Radio-Frequency source properties on RF-based atom traps". In: *The European Physical Journal D* 47.2 (Apr. 2008), pp. 209–214. ISSN: 1434-6060, 1434-6079. DOI: 10.1140/epjd/e2008-00050-2. URL: http://link.springer.com/10.1140/epjd/e2008-00050-2 (visited on 11/28/2024).

[64] Holger Müller et al. "Atom Interferometry with up to 24-Photon-Momentum-Transfer Beam Splitters". In: *Phys. Rev. Lett.* 100.18 (May 2008). Publisher: American Physical Society, p. 180405. DOI: 10.1103/PhysRevLett.100.180405. URL: https://link.aps.org/doi/10.1103/PhysRevLett.100.180405.

[65] H. Müntinga et al. "Interferometry with Bose-Einstein Condensates in Microgravity". In: *Physical Review Letters* 110.9 (Feb. 25, 2013), p. 093602. ISSN: 0031-9007, 1079-7114. DOI: 10.1103/PhysRevLett.110.093602. URL: https://link.aps.org/doi/10.1103/PhysRevLett.110.093602 (visited on 08/27/2025).

[66] Isaac Newton. "A letter of Mr. Isaac Newton, to the publisher from Cambridge, Febr. 6. 1671/72; in order to be communicated to the R. Society". In: *Philosophical Transactions of the Royal Society of London* 6.80 (Feb. 19, 1672), pp. 3075–3087. ISSN: 0261-0523, 2053-9223. DOI: 10.1098/rstl.1671.0072. URL: https://royalsocietypublishing.org/doi/10.1098/rstl.1671.0072 (visited on 09/27/2023).

[67] Lorne A. Page. "Effect of Earth's Rotation in Neutron Interferometry". In: *Physical Review Letters* 35.8 (Aug. 25, 1975), pp. 543–543. ISSN: 0031-9007. DOI: 10.1103/PhysRevLett.35.543. URL: https://link.aps.org/doi/10.1103/PhysRevLett.35.543 (visited on 11/22/2024).

[68] R. Paschotta. "Acousto-optic Modulators - an encyclopedia article". In: *RP Photonics Encyclopedia*. RP Photonics AG, 2008. DOI: 10.

61835/az1. URL: https://www.rp-photonics.com/acousto_optic_modulators.html (visited on 11/30/2024).

[69] Wolfgang Petrich et al. "Behavior of atoms in a compressed magneto-optical trap". In: *J. Opt. Soc. Am. B* 11.8 (Aug. 1994). Publisher: Optica Publishing Group, pp. 1332–1335. DOI: 10.1364/JOSAB.11.001332. URL: https://opg.optica.org/josab/abstract.cfm?URI=josab-11-8-1332.

[70] S. Pollock et al. "Integrated magneto-optical traps on a chip using silicon pyramid structures". In: *Optics Express* 17.16 (Aug. 3, 2009), p. 14109. ISSN: 1094-4087. DOI: 10.1364/OE.17.014109. URL: https://opg.optica.org/oe/abstract.cfm?uri=oe-17-16-14109 (visited on 11/30/2024).

[71] Daryl W Preston. "Doppler-free saturated absorption: Laser spectroscopy". In: *American Journal of Physics* 64.11 (1996). Publisher: [Woodbury, NY, etc. Published for the American Association of Physics ..., pp. 1432–1436.

[72] Norman F. Ramsey. "A Molecular Beam Resonance Method with Separated Oscillating Fields". In: *Physical Review* 78.6 (June 15, 1950), pp. 695–699. ISSN: 0031-899X. DOI: 10.1103/PhysRev.78.695. URL: https://link.aps.org/doi/10.1103/PhysRev.78.695 (visited on 11/30/2024).

[73] Ernst M. Rasel et al. "Atom Wave Interferometry with Diffraction Gratings of Light". In: *Physical Review Letters* 75.14 (Oct. 2, 1995), pp. 2633–2637. ISSN: 0031-9007, 1079-7114. DOI: 10.1103/PhysRevLett.75.2633. URL: https://link.aps.org/doi/10.1103/PhysRevLett.75.2633 (visited on 11/22/2024).

[74] G. Rosi et al. "Precision measurement of the Newtonian gravitational constant using cold atoms". In: *Nature* 510.7506 (June 2014), pp. 518–521. ISSN: 0028-0836, 1476-4687. DOI: 10.1038/nature13433. URL: https://www.nature.com/articles/nature13433 (visited on 11/30/2024).

[75] C. A. Sackett and J. A. Stickney. "Time-orbiting-potential chip trap for cold atoms". In: *Phys. Rev. A* 107.6 (June 2023). Publisher: American Physical Society, p. 063305. DOI: 10.1103/PhysRevA.107.063305. URL: https://link.aps.org/doi/10.1103/PhysRevA.107.063305.

[76] M. Georges Sagnac. "The Existence of the Luminiferous Ether Demonstrated by Means of the Effect of a Relative Ether Wind in an Uniformly Rotating Interferometer". In: *Relativity in Rotating Frames*. Ed. by Guido Rizzi and Matteo Luca Ruggiero. Dordrecht: Springer Netherlands, 2004, pp. 5–7. ISBN: 978-90-481-6514-8 978-94-017-0528-8. DOI: 10.1007/978-94-017-0528-8_2. URL: http://link.springer.com/10.1007/978-94-017-0528-8_2 (visited on 11/22/2024).

[77] S. Sala et al. "First demonstration of antimatter wave interferometry". In: *Science Advances* 5.5 (May 3, 2019), eaav7610. ISSN: 2375-2548. DOI: 10.1126/sciadv.aav7610. URL: https://www.science.org/doi/10.1126/sciadv.aav7610 (visited on 11/22/2024).

[78] G. A. Sinuco-Leon et al. "Microwave spectroscopy of radio-frequency-dressed Rb 87". In: *Physical Review A* 100.5 (Nov. 22, 2019), p. 053416. ISSN: 2469-9926, 2469-9934. DOI: 10.1103/PhysRevA.100.053416. URL: https://link.aps.org/doi/10.1103/PhysRevA.100.053416 (visited on 11/22/2024).

[79] Edward Slowik. "Plenum". In: *The Cambridge Descartes Lexicon*. Ed. by Lawrence Nolan. 1st ed. Cambridge University Press, Dec. 31, 2015, pp. 601–602. ISBN: 978-0-521-19352-8 978-0-511-89469-5. DOI: 10.1017/CBO9780511894695.205. URL: https://www.cambridge.org/core/product/identifier/CBO9780511894695A214/type/book_part (visited on 09/27/2023).

[80] Hongwei Song et al. "Normalized detection by using the blow-away signal in cold atom interferometry". In: *Optics Express* 24.25 (Dec. 12, 2016), p. 28392. ISSN: 1094-4087. DOI: 10.1364/OE.24.028392. URL: https://opg.optica.org/abstract.cfm?URI=oe-24-25-28392 (visited on 11/30/2024).

[81] A. M. Steane, M. Chowdhury, and C. J. Foot. "Radiation force in the magneto-optical trap". In: *Journal of the Optical Society of America B* 9.12 (Dec. 1, 1992), p. 2142. ISSN: 0740-3224, 1520-8540. DOI: 10.1364/JOSAB.9.002142. URL: https://opg.optica.org/abstract.cfm?URI=josab-9-12-2142 (visited on 11/30/2024).

[82] Daniel A. Steck. *"Rubidium 87 D Line Data,"*

[83] Pippa Storey and Claude Cohen-Tannoudji. "The Feynman path integral approach to atomic interferometry. A tutorial". In: *Journal de Physique II* 4.11 (Nov. 1994), pp. 1999–2027. ISSN: 1155-4312, 1286-4870. DOI: 10.1051/jp2:1994103. URL: http://jp2.journaldephysique.org/10.1051/jp2:1994103 (visited on 11/22/2024).

[84] Peter van der Straten and Harold Metcalf. "The atom–light interaction". In: *Atoms and Molecules Interacting with Light: Atomic Physics for the Laser Era*. Cambridge University Press, 2016, pp. 40–63.

[85] Ben Stray et al. "Quantum sensing for gravity cartography". In: *Nature* 602.7898 (Feb. 24, 2022), pp. 590–594. ISSN: 0028-0836, 1476-4687. DOI: 10.1038/s41586-021-04315-3. URL: https://www.nature.com/articles/s41586-021-04315-3 (visited on 11/22/2024).

[86] E. Tardiff et al. "Two-symmetry Penning-Ioffe trap for antihydrogen cooling and spectroscopy". In: *Nuclear Instruments and Methods in Physics Research Section A: Accelerators, Spectrometers, Detectors and Associated Equipment* 977 (Oct. 2020), p. 164279. ISSN: 01689002. DOI: 10.1016/j.nima.2020.164279. URL: https://linkinghub.elsevier.com/retrieve/pii/S0168900220306756 (visited on 11/30/2024).

[87] M. E. Tobar et al. "High precision microwave interferometers and oscillators for applied and fundamental physics applications". In: *2010 International Conference on Electromagnetics in Advanced Applications*. 2010, pp. 803–806. DOI: 10.1109/ICEAA.2010.5650761.

[88] Konrad Viebahn. *Introduction to Floquet theory*. Nov. 13, 2020.

[89] Nikolay V. Vitanov et al. "Stimulated Raman adiabatic passage in physics, chemistry, and beyond". In: *Reviews of Modern Physics* 89.1 (Mar. 8, 2017), p. 015006. ISSN: 0034-6861, 1539-0756. DOI: 10.1103/RevModPhys.89.015006. URL: https://link.aps.org/doi/10.1103/RevModPhys.89.015006 (visited on 08/27/2025).

[90] Xuezhi Wang et al. "Improving measurement performance via fusion of classical and quantum accelerometers". In: *Journal of Navigation* 76.1 (Jan. 2023), pp. 91–102. ISSN: 0373-4633, 1469-7785. DOI: 10.1017/S0373463322000637. URL: https://www.cambridge.org/core/product/identifier/S0373463322000637/type/journal_article (visited on 08/27/2025).

[91] S. A. Werner, E. Gürmen, and A. Arrott. "Neutron-Diffraction Measurement of the Lattice Parameter of Potassium Metal at 5.2°K". In: *Physical Review* 186.3 (Oct. 15, 1969), pp. 705–711. ISSN: 0031-899X. DOI: 10.1103/PhysRev.186.705. URL: https://link.aps.org/doi/10.1103/PhysRev.186.705 (visited on 11/22/2024).

[92] S. A. Werner et al. "Observation of the Phase Shift of a Neutron Due to Precession in a Magnetic Field". In: *Physical Review Letters* 35.16 (Oct. 20, 1975), pp. 1053–1055. ISSN: 0031-9007. DOI: 10.1103/PhysRevLett.35.1053. URL: https://link.aps.org/doi/10.1103/PhysRevLett.35.1053 (visited on 11/22/2024).

[93] Jason R. Williams et al. "Pathfinder experiments with atom interferometry in the Cold Atom Lab onboard the International Space Station". In: *Nature Communications* 15.1 (Aug. 13, 2024), p. 6414. ISSN: 2041-1723. DOI: 10.1038/s41467-024-50585-6. URL: https://www.nature.com/articles/s41467-024-50585-6 (visited on 11/30/2024).

[94] Michael J. Wright et al. "Cold atom inertial sensors for navigation applications". In: *Frontiers in Physics* 10 (Oct. 3, 2022), p. 994459. ISSN: 2296-424X. DOI: 10.3389/fphy.2022.994459. URL: https://www.frontiersin.org/articles/10.3389/fphy.2022.994459/full (visited on 11/30/2024).

[95] P. Zeeman. "XXXII. *On the influence of magnetism on the nature of the light emitted by a substance*". In: *The London, Edinburgh, and Dublin Philosophical Magazine and Journal of Science* 43.262 (Mar. 1897), pp. 226–239. ISSN: 1941-5982, 1941-5990. DOI: 10.1080/14786449708620985. URL: https://www.tandfonline.com/doi/full/10.1080/14786449708620985 (visited on 11/30/2024).

[96] Lin Zhou et al. "Test of Equivalence Principle at 1 0 - 8 Level by a Dual-Species Double-Diffraction Raman Atom Interferometer". In: *Physical Review Letters* 115.1 (July 2, 2015), p. 013004. ISSN: 0031-9007, 1079-7114. DOI: 10.1103/PhysRevLett.115.013004. URL: https://link.aps.org/doi/10.1103/PhysRevLett.115.013004 (visited on 11/22/2024).